

**Monolithic Millimeter-Wave Two-Dimensional
Horn Imaging Arrays**

Thesis by

Gabriel M. Rebeiz

In Partial Fulfillment of the Requirements

for the Degree of

Doctor of Philosophy

California Institute of Technology

Pasadena, California

1988

(Submitted March 29, 1988)

TO MY FATHER

Acknowledgements

I would like to express my deepest gratitude to my advisor, Professor David Rutledge, for his guidance, encouragement and support. He was always receptive and enthusiastic to my research ideas, and always encouraged me to do my best. I am also deeply thankful for the hours Dale and Dave spent with me when I was in need, and for guiding me during my stay at Caltech. I leave this place having Dave as a role model in honesty and hard work.

I am grateful to the Submillimeter-Wave group at the Jet Propulsion Laboratory, NASA, for providing me with technical support and encouragement. I am also indebted to Professors N. C. Luhmann, Jr. and H. R. Fetterman at the University of California, Los Angeles, for the use of their facilities. I thank Rick Savage for assisting me in the far-infrared measurements at UCLA, and for all the great times we spent together in the last two years.

I would like to thank all the members of the Caltech Millimeter-Wave IC group, for providing a healthy atmosphere for cooperation and research. In particular, I would like to thank Dayalan Kasilingam and Rick Compton for their electromagnetic and computer support, Wade Regehr, Yong Guo, and Wayne Lam for their fabrication support, Wyman Williams for sharing his microwave expertise, Phil Stimson for helping with the measurements, and Kent Potter for teaching me useful lab practices. I also thank the new members, Moonil Kim, Scott Wedge, and Bobby Weikle, for injecting a new spirit in the group. Last but not least, I am eternally indebted to Zoya Popović, for trying her best to make me a better person.

Finally, I thank my father for his love and patience, and Michel, for being the best brother one can ask for.

Monolithic Millimeter-Wave Two-Dimensional Horn Imaging Arrays

Abstract

A new monolithic millimeter-wave two-dimensional horn imaging array is presented. In this configuration, a dipole is suspended in an etched pyramidal cavity on a $1\text{-}\mu\text{m}$ silicon-oxynitride membrane. This approach allows ample space for low-frequency interconnections, while still maintaining efficient diffraction-limited imaging. The fabrication procedure of the horn array and the deposition parameters of the membrane layer are presented in detail. The array is analysed rigorously, by approximating the horn antenna by a structure of multiple rectangular waveguide sections. Pattern measurements at 93 GHz and 242 GHz agree well with the theory. The results show that horn antennas with an opening between 1.0λ and 1.5λ have high aperture efficiencies and would match well appropriate imaging systems. Also, a new wideband log-periodic antennas is integrated on a thin membrane and tuned by a back plane reflector. The antenna patterns are measured at 167 GHz, 370 GHz and 700 GHz, and the effect of the back-plane reflector is investigated at 370 GHz.

TABLE OF CONTENTS

Acknowledgement	iii
Abstract	iv
1. Introduction	1
1.1 Antennas on Substrates	2
1.2 Two-Dimensional Imaging Arrays	5
1.3 Overview of the Thesis	6
2. Monolithic Two-Dimensional Imaging Antenna Arrays	
Theory, Fabrication and Design	11
2.1 Diffraction-Limited Imaging	13
2.2 Fabrication	17
2.3 Membrane-Layer Deposition	20
2.4 Theory	25
2.5 Design of the Horn Structure	32
2.6 Design of the Dipole Antenna	34
3. Monolithic Two-Dimensional Imaging Antenna Arrays	
Measurements	42
3.1 Comparison of Theory and Experiment	44
3.2 Phased-Array Applications	55
3.3 Microwave Scale-Model Measurements	58
3.4 System Calibration at 93.2 GHz	61
3.5 Horn-Aperture Efficiency Measurements	64
3.6 Coupling Efficiency Measurements	68
4. Log-Periodic Antennas on Thin Membranes	76
4.1 Introduction	76
4.2 Fabrication	77
4.3 Wideband Log-Periodic Antenna	79

4.4 Linear Imaging Array	89
5. Future Work	92
5.1 Low-Frequency Horn Arrays	92
5.2 High-Gain Horn Arrays	93
5.3 Doubly-Polarized Horn Arrays	95
5.4 Back-to-Back Horn Arrays	95
5.5 Polarization-Duplexed Heterodyne Arrays	99
5.6 Coaxial Doubly-Polarized Horn Arrays	99

Chapter 1

Introduction

The frequency range of millimeter waves is defined as the region from 30 GHz to 300 GHz, while that of submillimeter waves is from 300 GHz to 3000 GHz. This corresponds to wavelengths between 10 mm and 0.1 mm. This region lies between the microwave and infrared spectra. It has shorter wavelengths and larger bandwidths than microwaves, and the millimeter-wave spectrum is less affected by atmospheric conditions than infrared radiation [1]. A millimeter-wave system could be considered as a hybrid between a microwave and an infrared system. The designer borrows ideas from both technologies to do a better job under specific conditions.

The shorter wavelengths of millimeter-waves allow the use of much smaller systems than microwave counterparts. This is very important in military applications, where size and weight are of primary concern. It also provides narrower beamwidth and higher gain. This means greater resolution in tracking and imaging applications. The large bandwidth allows the use of multi-frequency techniques (spread spectrum) in radars, and provides higher data rates in communication applications. The high frequencies of millimeter waves give larger doppler shifts for the same target velocities. This is especially useful in radar and tracking applications [2,3]. The atmospheric attenuation of millimeter waves is relatively low in the transmission windows compared to the optical and infrared wavelengths. This is important for applications where rain, fog and smoke occur frequently.

The unavailability of high power sources and of sensitive and reliable room temperature detectors at submillimeter-wave frequencies, made this region unattractive to military applications. However, it is still very useful as a scientific and academic analysis tool. In radio astronomy, measurements of molecular absorp-

tion lines that occur in this frequency band have provided considerable information on our universe [4]. In plasma diagnostics, measurements of electron density profiles and fluctuations have increased the understanding on controlled fusion experiments [5]. Submillimeter-wave receivers are being built by the Jet Propulsion Laboratory to study the mechanism of depletion of the earth ozone layer. Millimeter and submillimeter-wave systems have also being used in biological and medical applications [6].

Components at millimeter wave frequencies are either small machined versions of microwave waveguide components such as horn antennas, directional couplers or waveguide detectors, or metalized antennas integrated on a thick dielectric substrate (Silicon, GaAs, Quartz) with their associated detectors and transmission lines. The waveguide components provide better power handling capabilities and better performance than the integrated-circuit components, but are very expensive to build, and their performance is not repeatable at submillimeter-wave frequencies. They are best suited for applications where a small number of elements is needed. On the other hand, integrated-circuit systems are lithographically defined and processed using conventional IC techniques, and therefore inexpensive to build. They are best suited for large arraying applications, where low cost and a high degree of uniformity and reliability is needed.

1.2 Antennas on Substrates

Planar antennas on thick dielectric substrates are difficult to analyse electromagnetically [7]. They are generally narrowband, and have bad radiation patterns. They are also inefficient, since most of the power is coupled to substrate modes. Rutledge and Muha proposed the use of a substrate lens to eliminate the substrate modes losses, and increase the bandwidth of planar antennas [8]. They fabricated linear imaging arrays of wideband bow-tie antennas. Typical coupling efficiencies around 25% have been measured at 94 GHz and 240 GHz. Substrate-

lens coupled log-periodic and spiral antennas have much better radiation patterns than bow-tie antennas, and are therefore expected to have a higher coupling efficiency [9]. However, the dielectric losses in the substrate lens become particularly severe at submillimeter wavelengths, especially in imaging arrays that require a large substrate lens [10]. Parish and Fetterman used a twin-dipole antenna on a thick substrate, and Rogers and Neikirk used a twin-slot configuration on stacked substrates to eliminate the substrate modes and get good patterns, but the antennas became narrowband and still suffered from dielectric losses at submillimeter wavelengths [11,12].

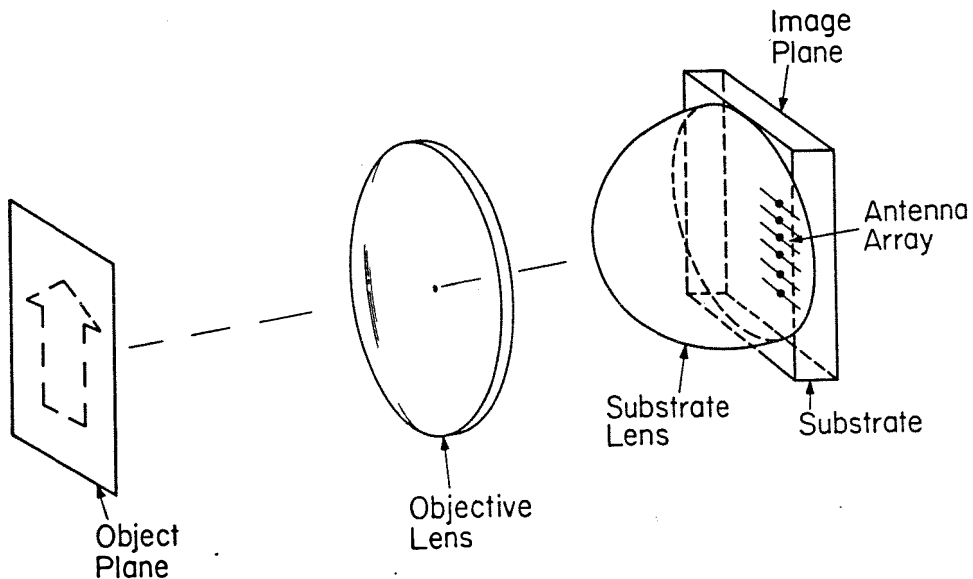


Figure 1. Millimeter-wave imaging system with substrate lens-coupled antenna array.

Fig. 2 shows the best measured receiver temperatures for SIS and Schottky diodes in different receiver designs. The lowest receiver temperatures in the range above 120 GHz are obtained with substrate coupled spiral and bow-tie antennas [13]. These figures are still much higher than the photon fluctuation limit of $\frac{h\nu}{k}$, h being

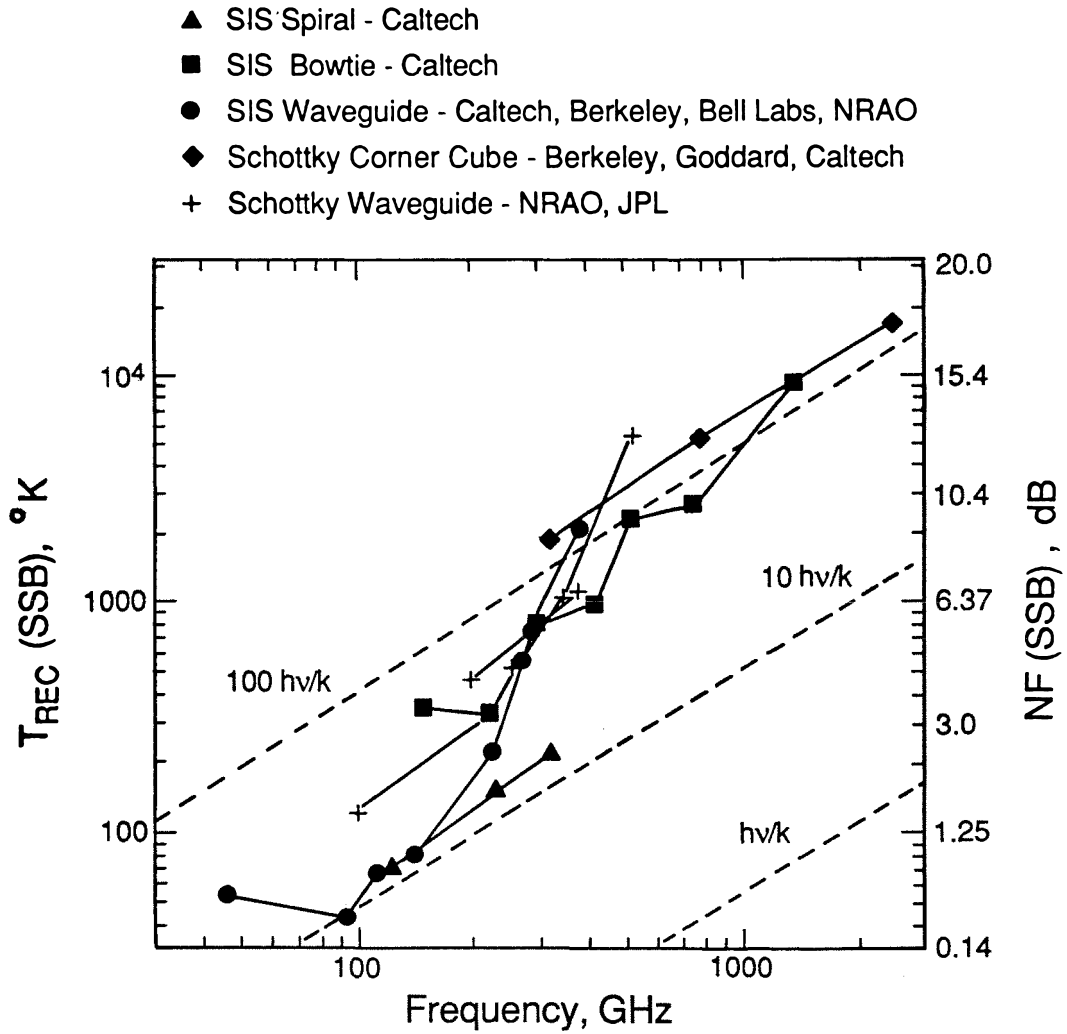


Figure 2. Best measured receiver temperatures for SIS and Schottky diodes in different receiver designs. (Courtesy of Prof. Thomas Phillips at the California Institute of Technology).

the Planck's constant, ν is the frequency and k is the Boltzmann's constant. Considerable improvement (about 3 dB) in the receiver performance is possible if the feed antenna to the imaging system exhibits high coupling efficiencies and low dielectric and resistive losses. Also, the accurate characterization of the mixer structure will result in a lower conversion loss, and therefore in lower receiver temperatures. However, this is not within the scope of this research. The main objective of this thesis is to develop high-efficiency focal-plane imaging antenna arrays for millimeter-wave applications.

In this thesis, we demonstrate antenna structures built on a 1- μm dielectric membrane. The membrane is so thin compared to a free space wavelength, that the antenna effectively radiates in free space. This approach eliminates the substrate lens and thus greatly reduces the dielectric losses. It also allows the use of free space antenna design techniques. This idea is used throughout this thesis to design wideband log-periodic antennas and two-dimensional imaging arrays for millimeter and submillimeter-wave applications.

1.2 Two-Dimensional Imaging Arrays

Two-dimensional imaging arrays offer much faster imaging of a scene than a scanned single element system [14]. A scanned system sees only one pixel at a time, and thus cannot image rapidly changing scenes of fast moving objects. Scanned systems could offer near real-time imaging, at the expense of a very short integration time per pixel, and thus poor noise performance. A two-dimensional focal plane imaging array, together with an optical system, can be considered a basic millimeter-wave camera.

An imaging array consist of a large number of antennas at the focal plane of an imaging system. The imaging system should be diffraction limited, that is, the resolution is limited by the optical system and not by the layout of the focal plane antennas [15]. The energy in each pixel, or resolution cell, is sampled by a single

antenna and converged to a detector. The outputs of all the detectors constitute an image. In order to couple the energy efficiently, the effective receiving area of a focal plane antenna should be the same as a resolution cell. In a diffraction limited imaging system, the resolution cells occupy *all* the space available on the focal plane. Therefore an efficient focal plane imaging array will have no room for low frequency lines and processing electronics.

The problem is then, how to build an *efficient* two-dimensional imaging array, while still leaving plenty of room for interconnections. One could think of making the antennas smaller. But this is not enough, because smaller antennas have smaller effective areas and therefore do not couple power efficiently. What is needed is a way to increase the effective area of the antenna without increasing its physical size. Kasilingam proposed a Fly's-eye array [16]. In this configuration, each antenna will be placed at the focal plane of a microlens (Fig. 3). The lens will increase the effective area of the antenna, thereby achieving efficient diffraction limited imaging with the use of small antennas.

In this thesis, I present a two-dimensional horn imaging array (Fig. 4). The idea is to etch crystalline silicon using an anisotropic etchant to create pyramidal cavities, or horn like structures. The antenna is suspended on a $1\text{-}\mu\text{m}$ membrane inside the horn. The focusing properties of the horn increases the effective area of the antenna, thus leaving plenty of room for interconnections. This configuration is entirely monolithic, with the antennas, detectors and processing electronics integrated on the back side of the wafer. It is simpler to fabricate than the fly's-eye array, and does not suffer from dielectric losses at submillimeter wavelengths.

1.3 Overview of the Thesis

As discussed earlier, the main objective of this thesis is to develop high-efficiency focal-plane imaging antenna arrays for millimeter-wave applications. The antennas should exhibit low cross-polarization, resistive and dielectric losses. The

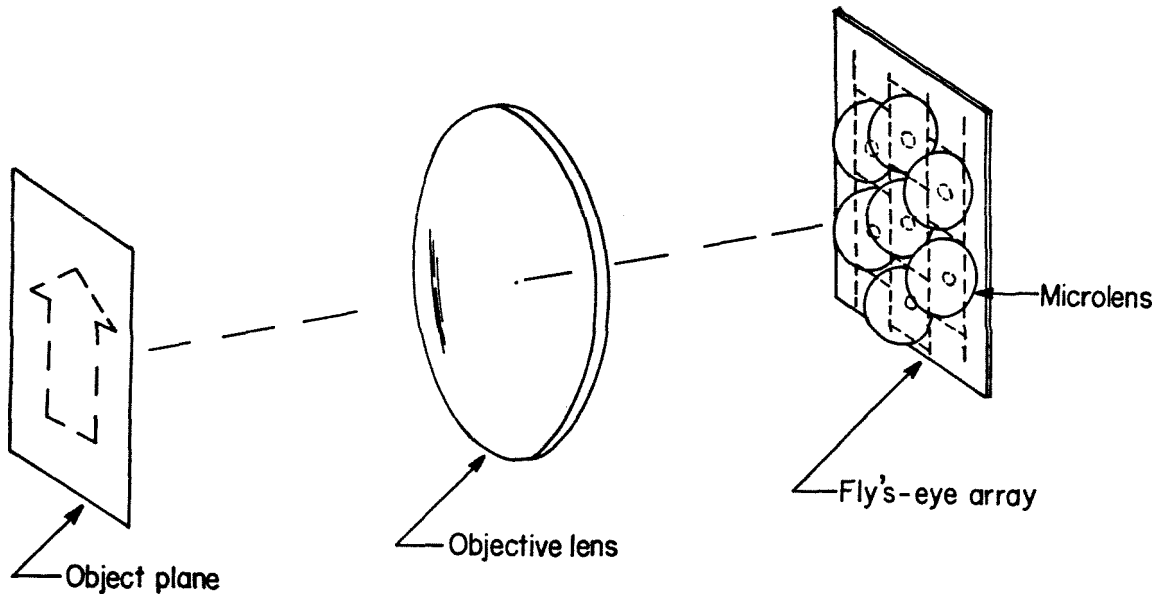


Figure 3. A fly-eye's array of microlenses.

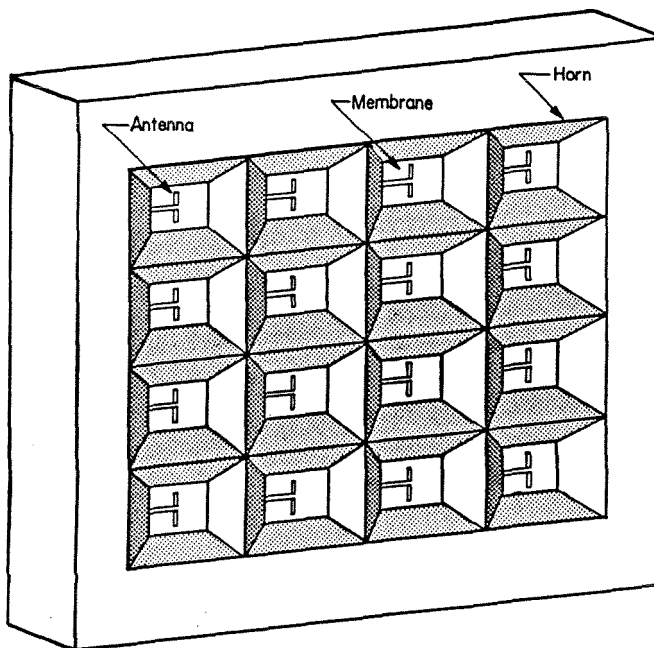


Figure 4. Two-dimensional focal-plane horn imaging array.

antenna impedance should be constant with frequency for wideband applications, and should match the low impedance of an SIS-junction or Schottky-diode mixer. Chapter 2 presents the fabrication, theory and design of a monolithic two-dimensional horn imaging array. The anisotropic etching of silicon and deposition parameters of the membrane layer are discussed in the fabrication section. The theoretical pattern of the horn array is calculated by approximating the horn by a structure of rectangular waveguides. The boundary conditions are matched at each of the waveguide discontinuity and at the aperture of the horn. The pattern is found using reciprocity, by calculating the received fields inside the horn for waves at different incident angles. Finally, the dipole antenna on the membrane is designed using free-space impedance formulas.

Chapter 3 describes the millimeter-wave measurement setup and presents the comparison between the theoretical and experimental results at 93 and 242 GHz. Measurements on a microwave scale model at 7.3 GHz are done in order to determine accurately the impedance of an antenna in a pyramidal cavity. Finally, horn-aperture efficiencies and coupling efficiencies to several f-number imaging systems are measured, and an accurate breakdown of the cross-polarization, mismatch and resistive losses of the horn antenna is presented.

Chapter 4 presents a new wideband log-periodic antenna integrated on a thin membrane. The antenna is tuned by a back-plane reflector. The antenna patterns are measured at 167 GHz, 370 GHz and 700 GHz. The effect of the back-plane reflector on the gain of the antenna is measured at 370 GHz. Finally, a linear log-periodic imaging array is designed and tested at 700 GHz.

Chapter 5 describes several new directions in the area of millimeter-wave monolithic horn arrays. Particular importance is given to new structures of highly efficient heterodyne imaging arrays. High-gain horn antennas, doubly-polarized horns and monolithic low-frequency horns are also proposed.

References

- [1] P. Bhartia and I. J. Bahl, "Millimeter Wave Engineering and Applications," Chap. 1, John Wiley & Sons, Inc., New York, 1984.
- [2] K. Miyanchi, "Millimeter-wave communications," *Infrared and Millimeter Waves*, Chap. 1, pp. 1-94, K. J. Button, ed., Academic Press, New York, 1983.
- [3] E. K. Reedy, G. W. Ewell, "Millimeter Radar," in *Infrared and Millimeter Waves*, vol. 4, pp. 23-94, K. J. Button Ed. Academic Press, New-York, 1983.
- [4] T. G. Phillips and D. B. Rutledge, "Superconducting tunnel detectors in radio astronomy," *Scientific American* vol. 254, pp. 96-102, 1986.
- [5] N. C. Luhman, Jr., "Instrumentation and Techniques for Plasma Diagnostics: An Overview," *Infrared and Millimeter Waves*, vol. 2, Chap. 1, K. J. Button, Ed., Academic Press, Inc., New york, 1983.
- [6] J. Elrich, "Centimeter and millimeter-wave thermography-A survey on tumor detection," *J. Microwave Power*, vol. 14, pp. 95-104, 1979.
- [7] R. C. Compton, R. C. McPhedran, Z. Popović, G. M. Rebeiz, P. P. Tong and D. B. Rutledge, "Bow-Tie antennas on a dielectric half-space: Theory and Experiment," *IEEE Trans. Antennas Propagat*, vol. AP-35, pp. 622-631, June 1987.
- [8] D. B. Rutledge, D. P. Neikirk, and D. P. Kasilingam, "Integrated-circuit antennas," in *Infrared and Millimeter Waves*, vol. 10, K. J. Button ed., Academic Press, New York, 1983, pp. 1-90. (Note: The argument k of the elliptic functions of equation (23) should be $\tan^2(45^\circ - \theta/4)$, rather than $\tan(45^\circ - \theta/4)$, where θ refers to the full bow angle.)
- [9] K. Lee and M. Frerking, "Planar antennas on thick dielectric substrates," *12'th Int. Conf. Infrared Millimeter Waves*, pp. 216-217, Lake Buena Vista, Dec. 1987.

- [10] G. W. Chantry, J. W. Flemming, P. M. Smith, "Far-infrared and millimeter-wave absorption spectra of some low-loss polymers," *Chemical Physics letters*, vol. 10, pp. 473–477, 1971.
- [11] R. L. Rogers, D. P. Neikirk, and H. Ling, "Planar matching of antennas on electrically thick dielectric substrates," *12'th Int. Conf. Infrared Millimeter Waves*, pp. 288–289, Lake Buena Vista, Dec. 1987.
- [12] P. Parrish, T. Sollner, R. Mathews, H. Fetterman, C. Parker, P. Tannenbaum, and A. Cardiasmenos, "Printed dipole–schottky diode millimeter wave antenna array," *SPIE Proc.*, vol. 337, Millimeter Wave Technology, May 6/7, 1982.
- [13] M. J. Wengler, D. P. Woody, R. E. Miller, and T. G. Phillips, "A low-noise receiver for millimeter and submillimeter waves," *Int. J. of Infrared and Millimeter Waves* vol. 6, pp. 697–706, 1985.
- [14] W. J. Wilson, R. J. Howard, A. C. Ibbott, G. S. Parks and W. B. Ricketts, "Millimeter-Wave Imaging Sensor," *IEEE Trans. Microwave Theory Tech*, vol. 34, pp. 1026–1035, 1986.
- [15] J. W. Goodman, "Introduction to Fourier Optics", pp. 4–21, McGraw Hill, New York, 1968.
- [16] D. P. Kasilingam and D. B. Rutledge, "Focusing properties of small lenses," *Infrared and Millimeter Waves*, vol. 7, pp. 1631–1647, 1986.

Chapter 2

Monolithic Two-Dimensional Imaging Antenna Arrays Theory, Fabrication and Design

Millimeter-wave imaging systems are becoming important in many scientific and military applications [1–5]. They provide much better resolution than microwave imaging systems and are less affected by atmospheric conditions than infrared systems. The use of a single detector and a mechanically scanned imaging system is a well established technique for millimeter and submillimeter-wave imaging [6,7]. Scanning systems, whether electronic or mechanical, are inadequate in certain applications. The events may be too fast, or the required integration time too long. The way to circumvent this limitation, is to image all points simultaneously onto multiple sensors. A millimeter-wave imaging array consists of a large number of antenna elements and detectors placed at the focal plane of an imaging system (Fig. 1). The antennas are the feeds for lenses and reflectors, and the output from all the detectors constitutes an image. At frequencies higher than 75 GHz, imaging systems using waveguide components become prohibitively expensive. A monolithic focal-plane imaging array is an attractive solution in these cases. In such a system, the antennas and detectors are integrated on a dielectric substrate such as quartz, silicon or gallium arsenide [8,9]. The substrate is necessary for mechanical support and electronics integration.

Antennas on thick dielectric substrates have relatively poor patterns and suffer from power lost to substrate modes [8]. A substrate lens is often mounted to eliminate the substrate modes [10,11], at the expense of increasing the dielectric losses. Recently, log-periodic and spiral antennas have showed good patterns with a quartz substrate lens [12]. However, the dielectric losses become particularly high at submillimeter wavelengths [13,14]. One way to solve the substrate problem, is

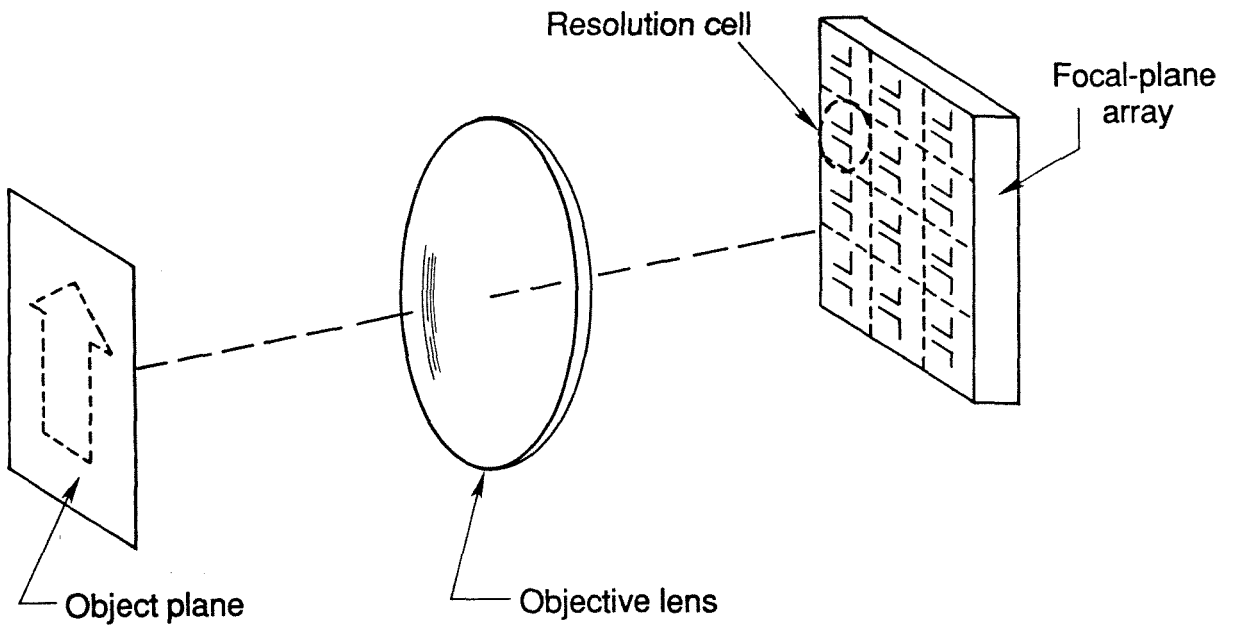


Figure 1. Millimeter-wave imaging system with antennas on a thick substrate.

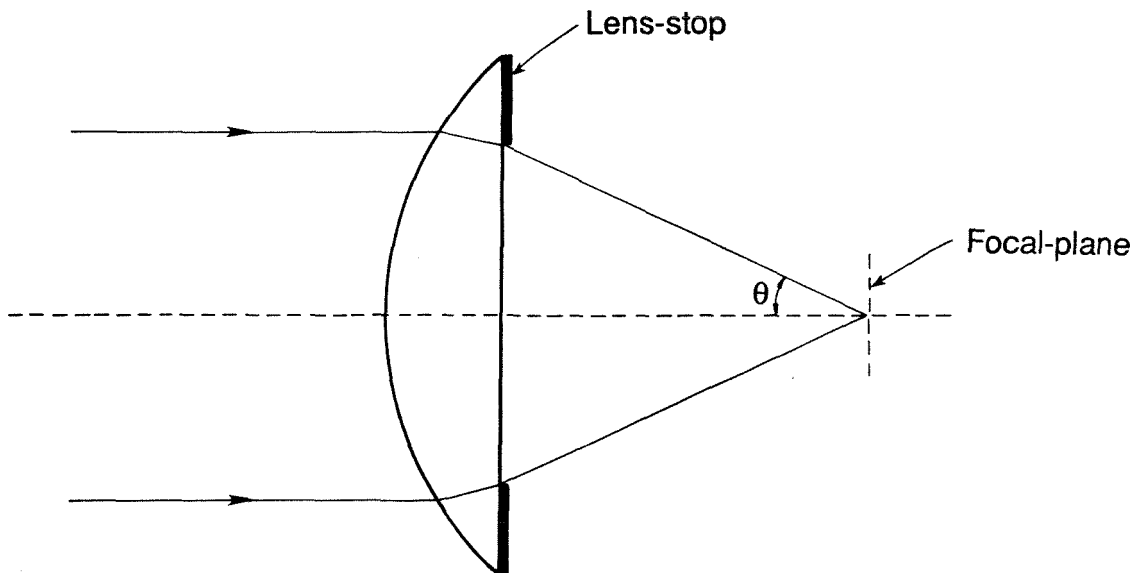


Figure 2. Imaging system with a half-subtended angle θ .

to integrate the antennas on a 1- μm thick dielectric membrane. The membrane is so thin compared to a free space wavelength, that the antenna effectively radiates in free space. This approach eliminates the substrate modes and thus the substrate lens. It also allows the use of free space antenna designs and techniques. Wideband log-periodic antennas and linear imaging arrays have been integrated on membranes for millimeter-wave and submillimeter-wave applications [15].

2.1 Diffraction-Limited Imaging

In a diffraction-limited imaging system, the antenna array should sample the image at such a rate that the resolution of the reconstructed image is limited only by the resolving power of the optical system. The sampling interval in free space, that allows exact reconstruction of a diffraction-limited image is [16]

$$\begin{aligned} T_E &= \lambda f^\# && \text{(for field detection)} \\ T_I &= \frac{\lambda f^\#}{2} && \text{(for intensity detection)} \end{aligned} \quad (2.1)$$

where $f^\#$ is the f-number of the imaging system (Fig. 2), given by

$$f^\# = \frac{1}{2 \sin(\theta)} \quad (2.2)$$

where θ is the half-angle subtended by the exit pupil [17]. If the image is sampled at an interval less than (2.1), the resolution will still be limited by the optical system. That is, one cannot do better than the diffraction limit of the lens. If the sampling interval is larger than (2.1), the resolution will be limited by the sampling rate and the image will be undersampled. The highest resolution is attained with systems with small f-numbers, mainly for an $f^\# = 0.5$, yielding a $T_E = \lambda$ and a $T_I = 0.5\lambda$. However, such systems have serious off-axis aberrations. These are distortions in the image that occur in the focal plane at small distances from the optical axis. Ruze [18] made an accurate analysis of these errors on a paraboloidal reflector, using lateral feed displacement and including diffraction effects. The results indicate that

if a 1-dB loss is tolerated, the maximum number of beamwidths scanned is given by

$$n = 0.44 + 22\left(\frac{f}{D}\right)^2 \quad (2.3)$$

where f is the focal length of the paraboloid, D is the aperture diameter, and a feed illumination taper of -10 dB has been assumed at the edges. It should be noted that the ratio $F = f/D$ is not the f-number of the paraboloidal imaging system. The f-number is still calculated from the half-subtended angle θ , given by

$$\theta = \frac{2}{\tan\left[\frac{1}{4(f/D)}\right]} \quad (2.4)$$

The f-number becomes equal to f/D , for $f/D \geq 1$. From Eq. (2.2), we see that large f-number systems do not suffer from off-axis aberrations. A system with $f/D = 1$ will allow 22 beamwidths off axis, and an array of 2000 elements in the focal-plane is feasible. Most imaging systems are a compromise between high resolution and low aberrations, and will have an f-number between 1 and 2 [19]. Such systems require an antenna spacing in the focal plane of the order of a free-space wavelength.

Monolithic millimeter-wave imaging arrays have been limited to one-dimensional designs. This is due to the fact that focal-plane antennas need to be as large as the spot size, or resolution cell, of the imaging optics to attain good coupling efficiencies. This limits the space available for low-frequency connections. In order to make room for the interconnections, one has to integrate smaller antennas. However, the effective aperture of these antennas has to be increased to maintain efficient diffraction-limited imaging. We have solved this problem by fabricating a two-dimensional array of pyramidal horns etched in silicon (Fig. 4). The antenna is suspended inside a horn on a $1\text{-}\mu\text{m}$ thick dielectric membrane. The antenna is either a dipole or a folded monopole and is much smaller than a resolution cell. The antennas typically occupy less than 25% of the wafer surface. The horn collects the

energy incident on a resolution cell, and focuses it to the antenna on the membrane. The focusing properties of the horn increase the effective area of the dipole, thus leaving plenty of room for interconnections. The horn array is entirely monolithic, with the antennas, detectors and interconnections integrated on the same silicon wafer. This configuration does not require a substrate lens, and therefore does not suffer from dielectric losses at submillimeter wavelengths. It is easily scalable because the dipole antenna effectively radiates in free-space bounded by a pyramidal cavity.

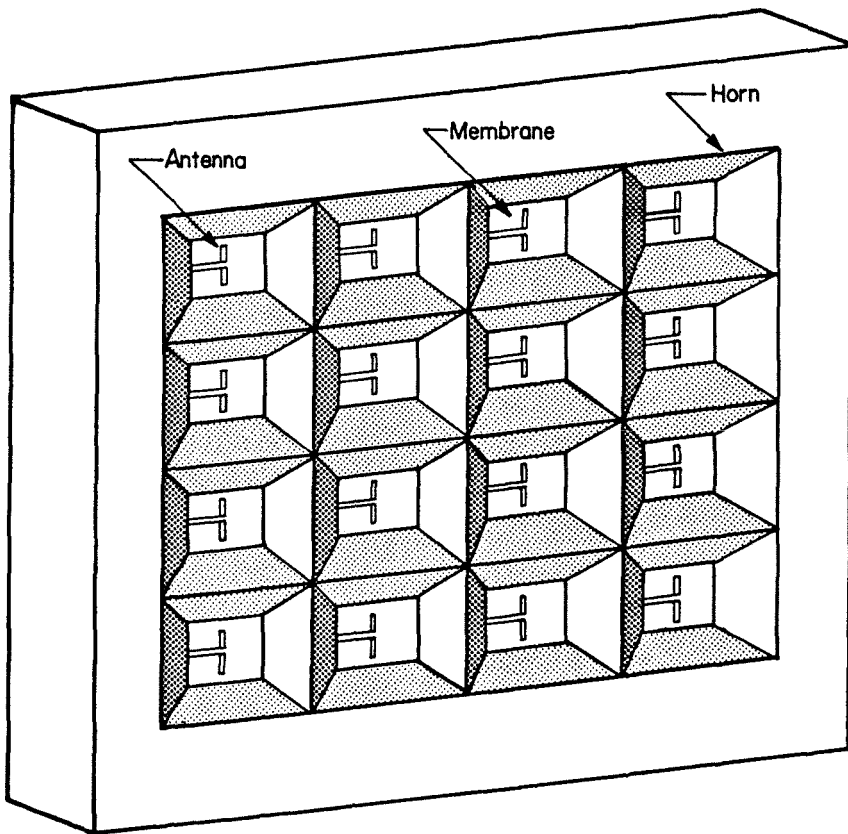


Figure 3. Perspective view of a two-dimensional horn imaging array.

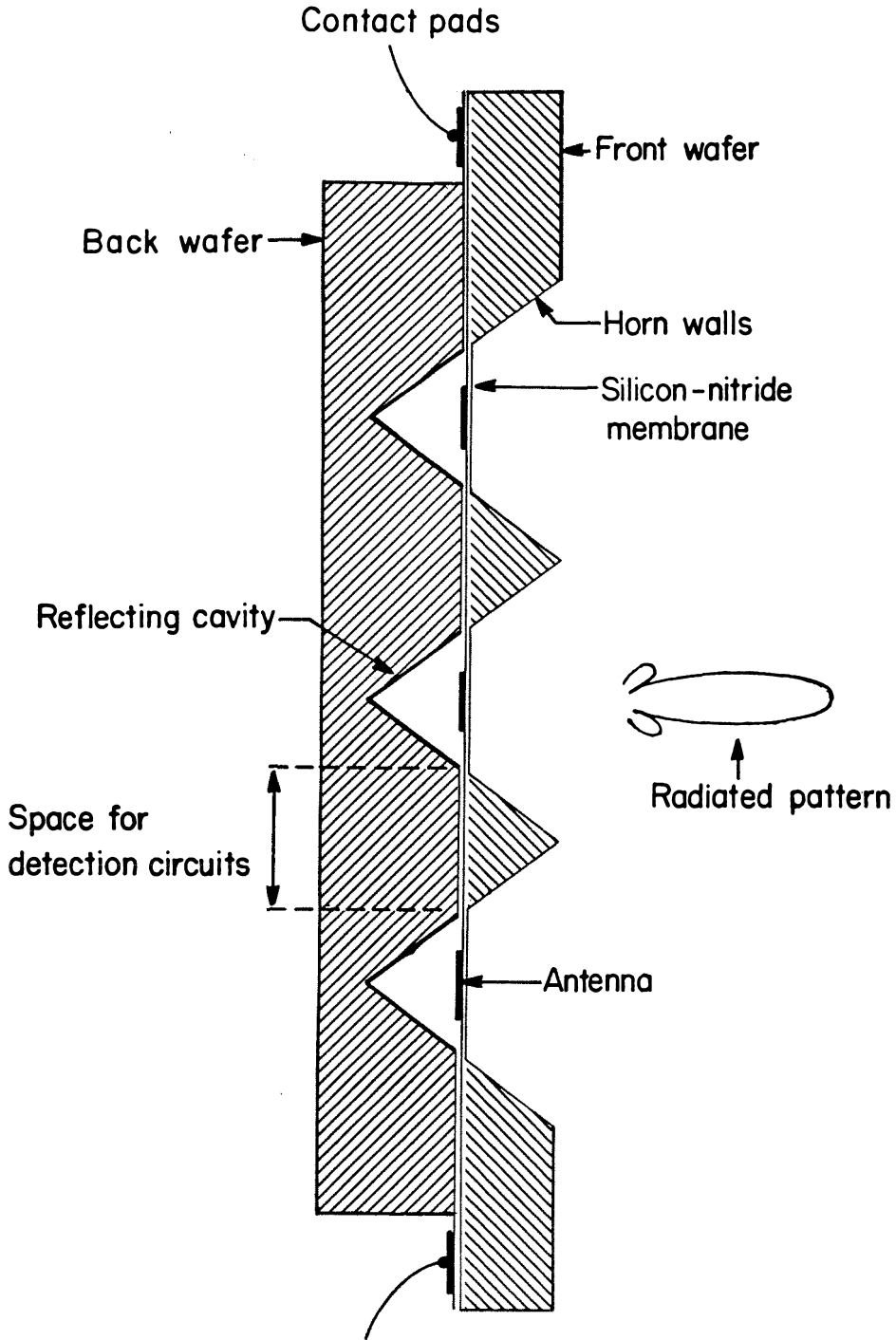


Figure 4. Side view of the horn-array showing the front and back wafers. The antenna is integrated on the membrane.

2.2 Fabrication

The horn array is a stacked silicon-wafer structure. The back wafer acts as a reflecting cavity, while the front wafer acts as the mouth of the horn (Fig. 4). The openings on the front wafer determine the aperture size of the horn antennas. The thickness of the front wafer determines the position of the antennas on the membrane inside the pyramidal horns. Each antenna is integrated on a 1- μm thick dielectric membrane, that is effectively suspended in a pyramidal cavity once the front and back wafers are etched and assembled together. The opening on the back wafer is made equal to the size of the membrane, to produce a pyramidal horn with smooth sidewalls.

To produce the cavities, a 5000 Å thermal oxide is grown on the back wafer [20], and a 1- μm silicon-oxynitride layer is deposited by plasma enhanced chemical vapor deposition on the front wafer. A discussion of the deposition parameters is presented later in this section. The openings are defined by patterning the wafers with photoresist and etching the silicon-oxynitride (on the front wafer) and the thermal oxide (on the back wafer) in a buffered-HF solution. The silicon wafers are then etched to create the pyramidal cavities. Reactive-ion etching or ion-beam milling is well suited for anisotropic etching of silicon, and especially for the fabrication of horn arrays with small flare angles. However, this process is expensive, and the technology is far from mature. On the other hand, chemical etching of silicon is a widely used process. Of importance is the etching in an ethylene-diamine pyrocatechol solution [21]. It can easily be masked by thermal oxide or silicon oxynitride. It yields a very uniform etch and a repeatable process. It is very inexpensive and does not require any special machines. Overetching proceeds at such a slow rate, that the prompt removal of the wafer from the solution is unnecessary. It is well suited for the fabrication of large arrays, 4 or 5 inches in cross section.

The etching process in ethylenediamine-pyrocatechol is anisotropic, etching the

$\langle 100 \rangle$ crystal plane at a much faster rate than the $\langle 111 \rangle$ planes (Fig. 5). The anisotropic $\langle 100 \rangle / \langle 111 \rangle$ etch rate ratio is 50:1. This forms pyramidal cavities bounded by $\langle 111 \rangle$ crystal planes [22]. These side walls form an angle of 54.7° with the $\langle 100 \rangle$ wafer plane. The horn flare angle is then 70.6° . This is larger than the optimum flare angle of horn antennas, but is fundamental to the etching process and cannot be changed. The openings on the front and back wafers have to be carefully aligned to the $\langle 110 \rangle$ crystals planes, otherwise overetching occurs [23]. The effect of misaligning an opening is an increase in the size of the etched hole in silicon (Fig. 6). The overetching stops when the hole perimeter is finally defined by an orthogonal set of $\langle 100 \rangle$ planes. If an opening of square size W is misaligned by an angle θ to the $\langle 110 \rangle$ planes, the resultant hole will have an opening of $W' = W(\sin \theta + \cos \theta)$. Therefore accurate crystallographic alignment of the surface pattern is necessary to achieve good dimensional control.

The horn openings on the front wafer, typically 2 to 3 mm in cross section, are defined very close to each other with a typical separation of $80\mu\text{m}$. This ensures that all the incident power enters the cavities and is not reflected by the array. However a small misalignment on the front wafer, and thus an increase in the opening size, can have a disastrous effect on the fabrication of the horn array. The separation will be overetched, and the horns will join together resulting in a useless array. On the other hand, a small misalignment on the back wafer can be tolerated, because the openings are far from each other. The alignment accuracy in our lab is better than $\pm 1^\circ$ to the $\langle 110 \rangle$ planes, resulting in a cavity that is only 2% bigger than the defined opening.

The back wafer is etched until a closed pyramidal cavity is formed, and etching is practically stopped. The front wafer is etched until the transparent silicon-oxynitride membrane appears. The membrane is resistant to the etch, so the prompt removal of the front and back wafers from the solution is unnecessary. The whole etching process is very uniform, yielding an array of cavities of exactly the same

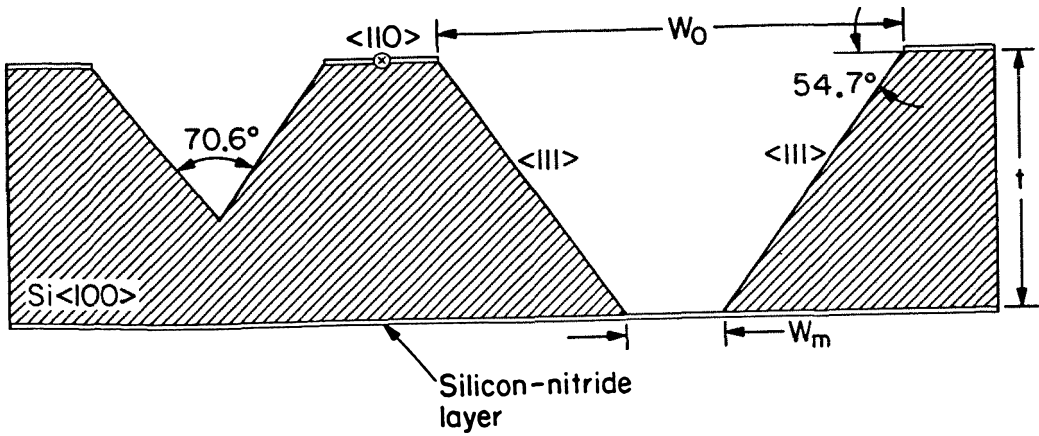


Figure 5. Examples of anisotropic etching in a $\langle 100 \rangle$ silicon wafer. The opening on the back wafer yields a closed pyramidal cavity (left), while the opening on the front wafer yields an opening $W_m = W_f - \sqrt{2}t$ (right).

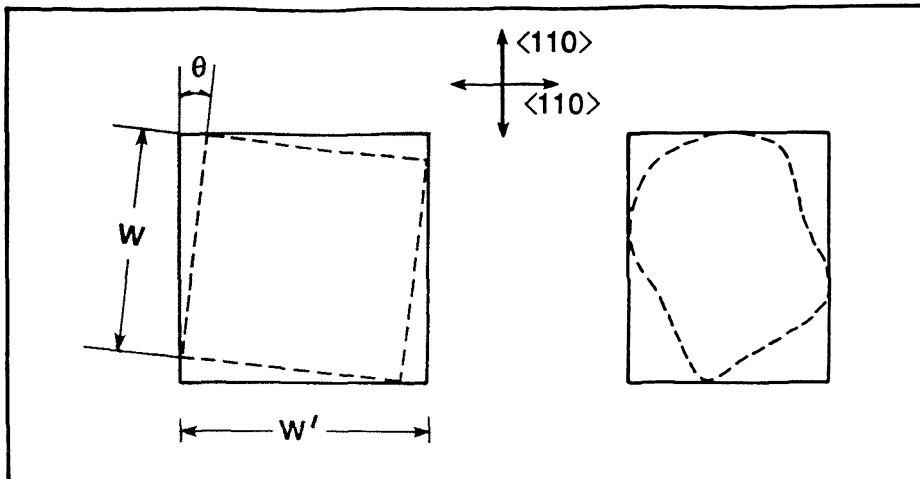


Figure 6. Effect of misalignment with the $\langle 110 \rangle$ crystal planes (left), and (right) the resultant hole of an arbitrary defined opening etched in ethylene-diamine pyrocatechol.

dimensions. After the etching is complete, the wafers are cleaned thoroughly. The $\langle 111 \rangle$ crystal planes are coated with gold to minimize the sidewall losses of the horn antennas.

Next, the antennas, detectors and processing electronics are all integrated on the front wafer, using standard lithographic techniques. The antennas and detectors are integrated on the membranes, while the processing electronics and the transmission lines are integrated on the available space near the membranes. Finally, the wafers are aligned and glued together using a thin layer of photoresist spread around the corners. The back wafer is smaller than the front wafer, to ensure access to the bonding pads. The wafer is mounted in a custom-made chip carrier, and several antennas are connected for pattern measurements. In practice, the design of the antenna will yield non-standard thicknesses for the front and back wafers. The front (and back) wafer may itself be a composite of several stacked wafers, etched to yield a smooth sidewall and glued together. There is approximately a $20 \mu\text{m}$ step in the pyramidal-cavity sidewalls when any two wafers are joined together. This is due to a slight misalignment with the $\langle 100 \rangle$ crystal planes, and to variations in the wafer thicknesses from batch to batch. Also, the resultant separation between two openings on the front wafer is about $40 \mu\text{m}$, which is very small compared to a wavelength (Fig. 7).

2.3 Membrane-Layer Deposition

To produce the membrane, a silicon-oxynitride layer is grown on the front wafer by plasma-enhanced chemical vapor deposition [24]. The deposition parameters are adjusted to produce a layer in tension, that is, the residual stress σ_R in the film are tensile. This is important because a layer in tension will produce flat and rigid membranes. The residual stress is dependent on the relative flow rates of NO_2 and NH_3 gases used to form the film (Fig. 8). The strength of the membrane is also an important design consideration. The hydrostatic strength, Q , is defined as the

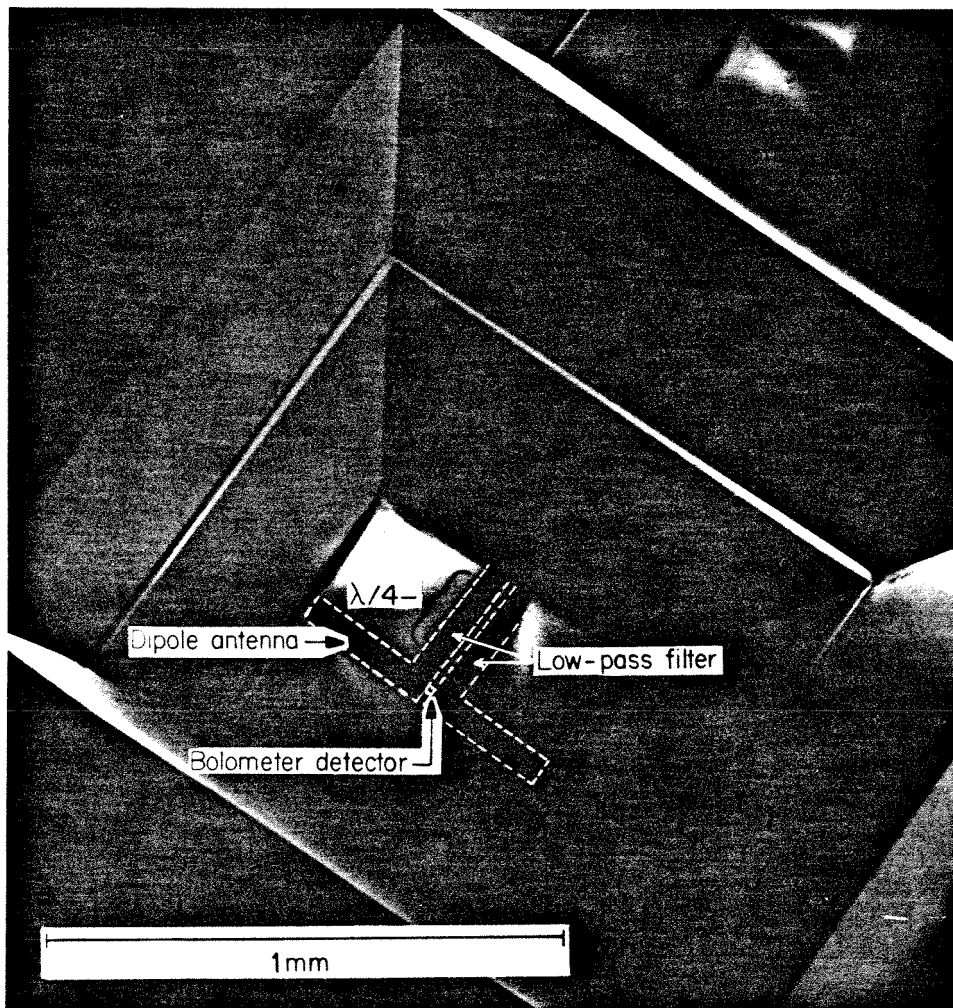


Figure 7. A scanning electron micrograph of a finished horn element.

pressure differential across the membrane sufficient to cause it to rupture. Such pressure differentials are an inevitable part of the fabrication process caused by, for example, by compressed air drying the wafers. For a square membrane, breakage occurs first at the center, when the internal stress in the membrane is equal to the tensile strength σ_B of the film. The hydrostatic strength is given by [25,26]

$$Q = \frac{2E_f d_f}{l} \left(\frac{\sigma_B - \sigma_R}{k(\nu)E_f} \right)^{3/2} \quad (2.5)$$

where l is the length of the membrane edge, and E_f , ν_f , and d_f are the Young's modulus, Poisson's ratio and the thickness of the film, respectively. The function $k(\nu)$ has the value 0.41 for $0.18 \leq \nu \leq 0.5$. Poisson's ratio for silicon oxynitride is around 0.2. From this result, the reduction of the residual stress in the film is effective in the increase of the hydrostatic strength.

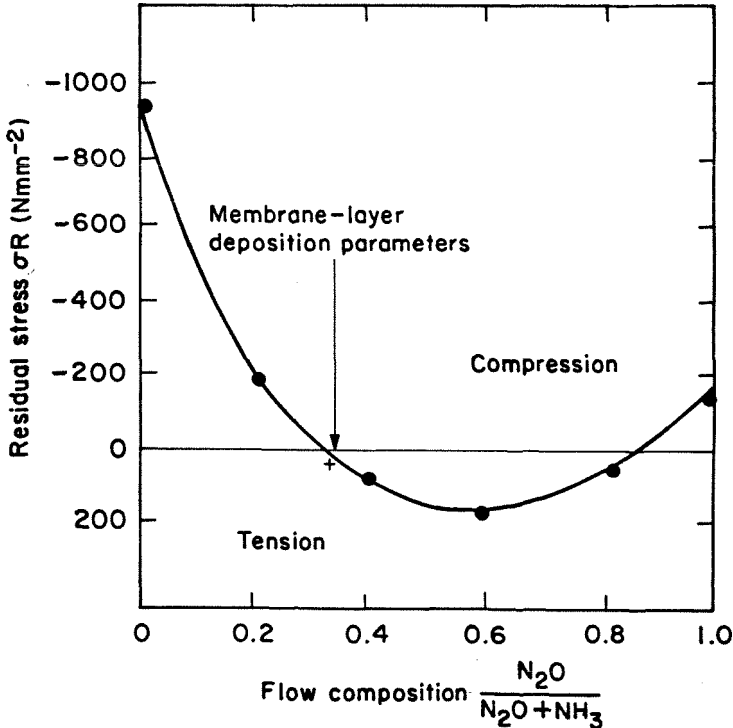


Figure 8. Residual stress versus flow composition. The membranes have a residual stress around 10 Nmm^{-2} .

The tensile strength of silicon-oxynitride is dependent on the deposition parameters. Since silicon-oxynitride is considered to be a low-quality silicon nitride film, its tensile strength is lower than that of silicon nitride. The tensile strength of high quality silicon nitride is 1000 Nmm^{-2} . The tensile strength of silicon-oxynitride is estimated to be around 400 Nmm^{-2} . The silicon-oxynitride films were deposited using a Pacific Western Systems plasma-enhanced chemical-vapor-deposition machine [27] under a deposition temperature of 300°C and a pressure of 2.0 mTorr , with an RF power density of 0.012 Wcm^{-2} and an RF frequency of 440 KHz . The gases used are silane (SiH_4), ammonia (NH_3) and nitrous oxide (N_2O). The flow composition was adjusted to obtain a σ_R around 10 Nmm^{-2} . This is much lower than the tensile strength of the film, and further reduction in the residual stress will not increase the hydrostatic strength of the membrane. We have fabricated a (7×7) array of $1.8 \times 1.8 \text{ mm}$ membranes $1\text{-}\mu\text{m}$ thick for a 93 GHz horn array. The membranes withstood all standard fabrication procedures, such as resist spinning, developing, contact exposure, evaporation and liftoff.

If a film is deposited in stress on a thin silicon substrate, the substrate will bend by a measurable degree. A tensile stress will bend it such that the film surface is concave, and a compressive stress so that it is convex. The method used to measure the stress of the silicon-oxynitride film is based on this principle [28]. A layer is deposited on one side of a silicon wafer, and the deformation of the wafer is measured by a DekTak (surface profiler) machine (Fig. 9). A circular wafer strained by the presence of the stress will bend into a paraboloid, with the peak at the center of the wafer. The residual stress, σ_R , can be related to the deflection h , of a circular wafer of radius r , by the equation

$$\sigma_R = \frac{E_s}{3(1-\nu)} \frac{h}{r^2} \frac{d_s^2}{d_f} \quad (2.6)$$

where E_s is the Young's modulus of the substrate, ν is the Poisson ratio of the substrate, d_s is the substrate thickness, and d_f is the film thickness. ν is between 0.2

and 0.25, and the value of $\frac{E_s}{(1-\nu)}$ for a $\langle 100 \rangle$ silicon substrate is $1.8 \times 10^5 \text{ Nmm}^{-2}$. A $1.6 \mu\text{m}$ layer of silicon oxynitride, deposited with a residual stress around 30 Nmm^{-2} , will deform a $550 \mu\text{m}$ thick silicon wafer with a radius of 1.5 inches, by an easily measurable $1.3 \mu\text{m}$ (Fig. 10).

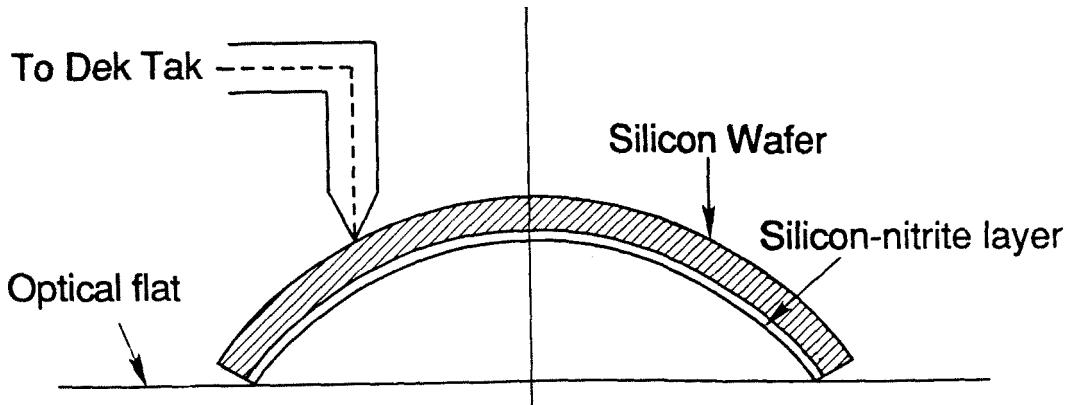


Figure 9. A silicon wafer under a tensile stress.

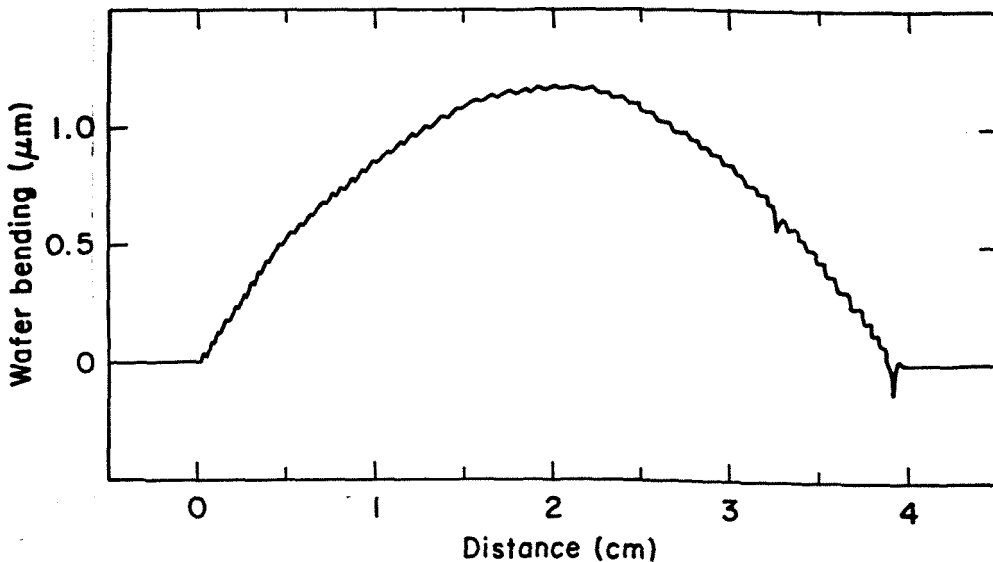


Figure 10. The measurement of the bending profile of a 1.5 in. silicon wafer.

2.4 Theory

The theoretical pattern of a single horn-element is calculated assuming an infinite two-dimensional array of horns. It should be noted that we are *not* calculating the pattern of a two-dimensional array of horns (i.e. a phased array), but rather the pattern of a single element in a two-dimensional array. This is because we are interested in a focal-plane array of antennas for multibeam imaging applications. Since the horn dimensions are comparable to a free-space wavelength, the horn-array has to be rigorously analysed using a complete electromagnetic solution. Earlier methods, summarized by Love [29], used diffraction theory and GTD techniques to predict the radiation patterns of horns. Unfortunately, these methods are not applicable for horns with large horn angles and short axial lengths. In this analysis, a horn-element is approximated by a structure of multiple rectangular waveguide sections (Fig. 11), and the fields in each waveguide section are given by a linear combination of waveguide modes. This method has been used before in the analysis of waveguide transformers [30], and recently applied to the analysis of a corrugated horn [31]. The fields in space are given by two-dimensional Floquet modes [32]. The boundary conditions are matched at each of the waveguide sections, and at the aperture of the horn. The antenna pattern may be calculated by assuming the antenna as either a transmitter or a receiver — the equivalence of these two cases follows from the reciprocity theorem [33]. In our analysis, we assume the horn to be a receiving antenna. The pattern is found by calculating the received fields at the position of an infinitesimal dipole inside the horn. The infinitesimal dipole is assumed not to perturb the fields inside the horn. The pattern of the horn antenna is then given by the power absorbed by the dipole for plane waves incident at different angles. The effect of the membrane on the incident radiation is neglected, since the membrane is very thin compared to a free space wavelength.

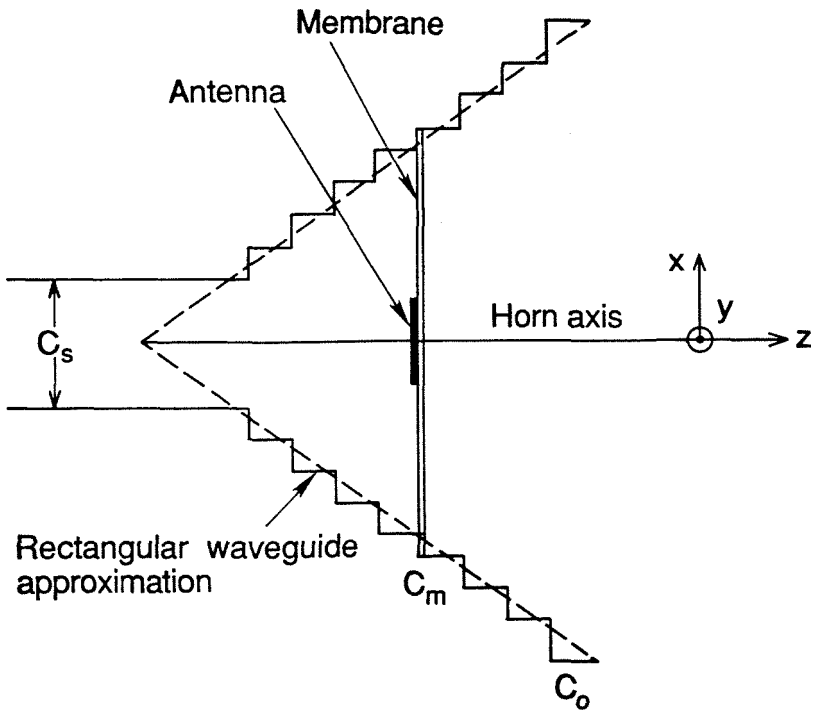


Figure 11. A stepped waveguide approximation of a pyramidal horn. C_0 is the first waveguide and C_m is the membrane waveguide.

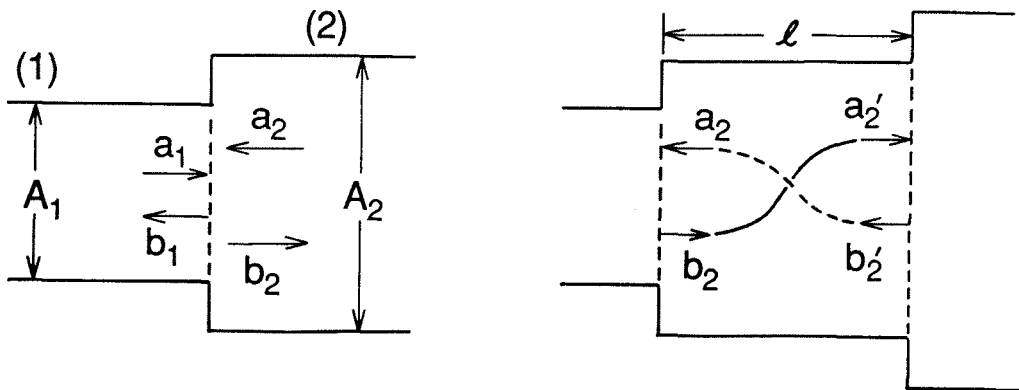


Figure 12. Forward and backward travelling waves on a waveguide step (left), and a waveguide section (right).

2.4a Pyramidal Horn Characterization

In this section, the scattering matrices of a waveguide-step junction and a linear-waveguide section are derived (Fig. 12). Then, a ‘‘Horn’’ matrix \mathbf{H} is calculated, relating the fields in the membrane section C_m to the fields in the opening section C_0 . Finally, the Floquet modes in space are matched to the fields in the opening waveguide, and the fields in section C_m are calculated in terms of incident field using the ‘‘Horn’’ matrix \mathbf{H} .

The transverse fields ($\vec{\mathbf{E}}_t, \vec{\mathbf{H}}_t$) in waveguide section (1) can be represented by a linear combination of TE and TM waveguide modes [34],

$$\begin{aligned}\vec{\mathbf{E}}_t^1 &= \sum_{n=0}^{\infty} \sum_{m=0}^{\infty} a_{mn}^{p1} e^{-j(\gamma_{mn}^{p1})z} \vec{\mathbf{e}}_{mn}^{p1} + \sum_{n=0}^{\infty} \sum_{m=0}^{\infty} b_{mn}^{p1} e^{+j(\gamma_{mn}^{p1})z} \vec{\mathbf{e}}_{mn}^{p1} \\ \vec{\mathbf{z}} \times \vec{\mathbf{H}}_t^1 &= \sum_{n=0}^{\infty} \sum_{m=0}^{\infty} a_{mn}^{p1} Y_{mn}^{p1} e^{-j(\gamma_{mn}^{p1})z} \vec{\mathbf{e}}_{mn}^{p1} - \sum_{n=0}^{\infty} \sum_{m=0}^{\infty} b_{mn}^{p1} Y_{mn}^{p1} e^{+j(\gamma_{mn}^{p1})z} \vec{\mathbf{e}}_{mn}^{p1}\end{aligned}\tag{2.7}$$

where p denotes either a TE or a TM mode, γ_{mn}^{p1} is the wave propagation constant and is real for a propagating wave and imaginary for an attenuating wave, Y_{mn}^{p1} is the wave admittance for a TE/TM mode, and $\vec{\mathbf{e}}_{mn}^{p1}$ is a TE/TM eigenvector normalized such that the power carried by a given wave is proportional to the square of its coefficient (a_{mn}^{p1} or b_{mn}^{p1}). The boldface characters represent vectors. The fields in section (2) follow the same representation. The coefficients a_{mn}^{p1} and b_{mn}^{p1} are unknown, and will be calculated later in terms of the incident field on the horn array. The orthonormalized set of eigenvectors for a waveguide of dimensions C_x and C_y are derived from the potential functions

$$\begin{aligned}\Psi_{TE} &= \cos(k_m x) \cos(k_n y) && \text{(for TE eigenvector)} \\ \Psi_{TM} &= \sin(k_m x) \sin(k_n y) && \text{(for TM eigenvector)}\end{aligned}\tag{2.8}$$

where ($k_m = \frac{m\pi}{C_x}$) and ($k_n = \frac{n\pi}{C_y}$). The boundary conditions at the waveguide-step junction are the continuity of the transverse electric and magnetic fields over the

area A_1 , and the vanishing of the transverse electric field on the area $(A_2 - A_1)$.

$$\begin{aligned}\vec{\mathbf{E}}_t^1 &= \vec{\mathbf{E}}_t^2 & (\text{over } A_1) \\ \vec{\mathbf{H}}_t^1 &= \vec{\mathbf{H}}_t^2 & (\text{over } A_1) \\ \vec{\mathbf{E}}_t &= 0 & (\text{on } A_2 - A_1)\end{aligned}\tag{2.9}$$

Using the Galerkin mode matching technique [35], we get a set of linear equations

$$\begin{aligned}\sum_n \sum_m (a_{mn}^{p1} + b_{mn}^{p1}) V_{mnMN}^{p1p2} &= a_{MN}^{p2} + b_{MN}^{p2} \\ -Y_{mn}^{p1} (a_{mn}^{p1} - b_{mn}^{p1}) &= \sum_N \sum_M Y_{MN}^{p2} V_{MNmn}^{p1p2} (a_{MN}^{p2} - b_{MN}^{p2})\end{aligned}\tag{2.10}$$

where V_{mnMN}^{p1p2} is the scalar product between a TE/TM eigenvector in section (1) and a TE/TM eigenvector in section (2), given by

$$V_{mnMN}^{p1p2} = \int_{A_1} \vec{\mathbf{e}}_{mn}^{p1} \cdot \vec{\mathbf{e}}_{MN}^{p2} dA_1\tag{2.11}$$

V could be considered as the coupling coefficient between a TE/TM mode in section (1) and a TE/TM mode in section (2). The fields in waveguide section (1) can be related to the fields in waveguide section (2) through the matrix equation

$$\begin{pmatrix} V & V \\ Y_1 & -Y_1 \end{pmatrix} \begin{pmatrix} a_1 \\ b_1 \end{pmatrix} = \begin{pmatrix} I & I \\ -V^T Y_2 & V^T Y_2 \end{pmatrix} \begin{pmatrix} a_2 \\ b_2 \end{pmatrix}\tag{2.12}$$

where I is a unit matrix, Y_1 and Y_2 are diagonal admittance matrices of the individual TE/TM modes in sections (1) and (2), respectively. V is a scalar-product matrix of the eigenmodes at the interface, and V^T is the transpose of V . (a_1, b_1) and (a_2, b_2) represent the coefficients of the incident and reflected fields for sections (1) and (2), respectively. The upper half of this equation is the boundary condition for the transverse electric field, and the lower half the boundary condition for the transverse magnetic field.

The fields in a lossless waveguide section (Fig. 12) are related by a simple phase-delay matrix, given by

$$\begin{pmatrix} a_2 \\ b_2 \end{pmatrix} = \begin{pmatrix} 0 & e^{-j(\gamma_{mn})l} \\ e^{+j(\gamma_{mn})l} & 0 \end{pmatrix} \begin{pmatrix} a_2' \\ b_2' \end{pmatrix}\tag{2.13}$$

The case of small losses in the pyramidal horn sidewalls can be modelled by multiplying the phase-delay factor by an attenuation factor $e^{-(\alpha_{mn}l)}$, where α_{mn} is the attenuation per unit length of a TE/TM waveguide mode, and l is the length of the waveguide section. Notice that we can only treat small losses in this analysis, since large losses will induce a tangential component of the electric field on the sidewalls, and the TE/TM mode representation will not be valid anymore.

The coefficients of the fields in the membrane section C_m can be related to the coefficients of the fields in the first section C_0 by multiplying the “step” and “delay” matrices of a large number of waveguide sections together. The resultant matrix is called the horn matrix \mathbf{H} . The smallest waveguide section C_s is not taken at the apex, but is chosen to be small enough to have only rapidly decaying evanescent waves. This section is then assumed to be an infinite rectangular waveguide with waves travelling only in the negative z -direction. This is a reasonable assumption because the waves decay so fast that the reflected fields beyond this section are negligible. It is important for the numerical solution because large exponential decay constants are avoided. It also provides a needed boundary condition, mainly that the reflected waves at C_s are zero. The boundary condition relates the forward and backward travelling waves in the waveguide sections together. This results in only one independent set of variables at C_0 to match to the incident field.

2.4b Matching to the Floquet Modes

The transverse fields in air ($\vec{\mathbf{E}}_t^f, \vec{\mathbf{H}}_t^f$) can be represented by a linear combination of TE and TM Floquet modes [32] (Fig. 13),

$$\begin{aligned}\vec{\mathbf{E}}_t^f &= a_{00}^{pf} e^{+j(\gamma_{00}^{pf})z} \vec{\mathbf{e}}_{00}^{pf} + \sum_{n=-\infty}^{\infty} \sum_{m=-\infty}^{\infty} b_{mn}^{pf} e^{-j(\gamma_{mn}^{pf})z} \vec{\mathbf{e}}_{mn}^{pf} \\ \vec{\mathbf{z}} \times \vec{\mathbf{H}}_t^f &= -a_{00}^{pf} Y_{00}^{pf} e^{+j(\gamma_{00}^{pf})z} \vec{\mathbf{e}}_{00}^{pf} + \sum_{n=-\infty}^{\infty} \sum_{m=-\infty}^{\infty} b_{mn}^{pf} Y_{mn}^{pf} e^{-j(\gamma_{mn}^{pf})z} \vec{\mathbf{e}}_{mn}^{pf}\end{aligned}\tag{2.14}$$

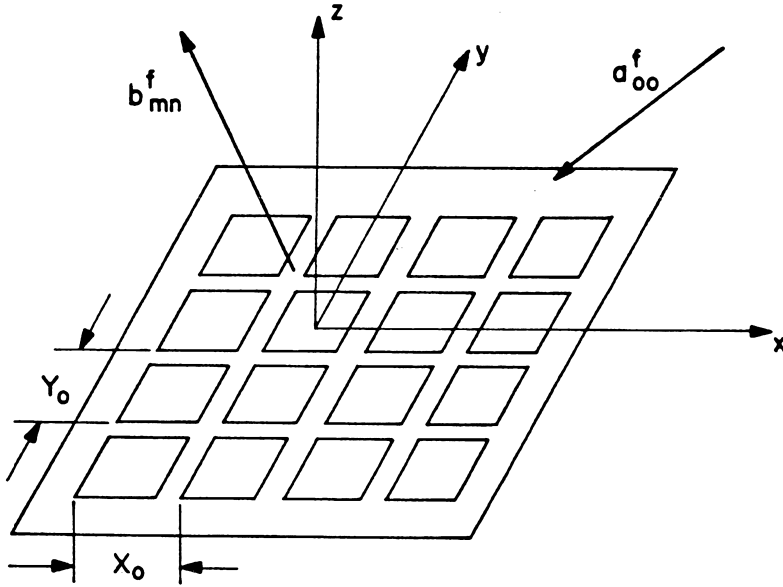


Figure 13. Reflected Floquet modes from a doubly-periodic structure. X_0 and Y_0 are the periods in the x and y directions, respectively.

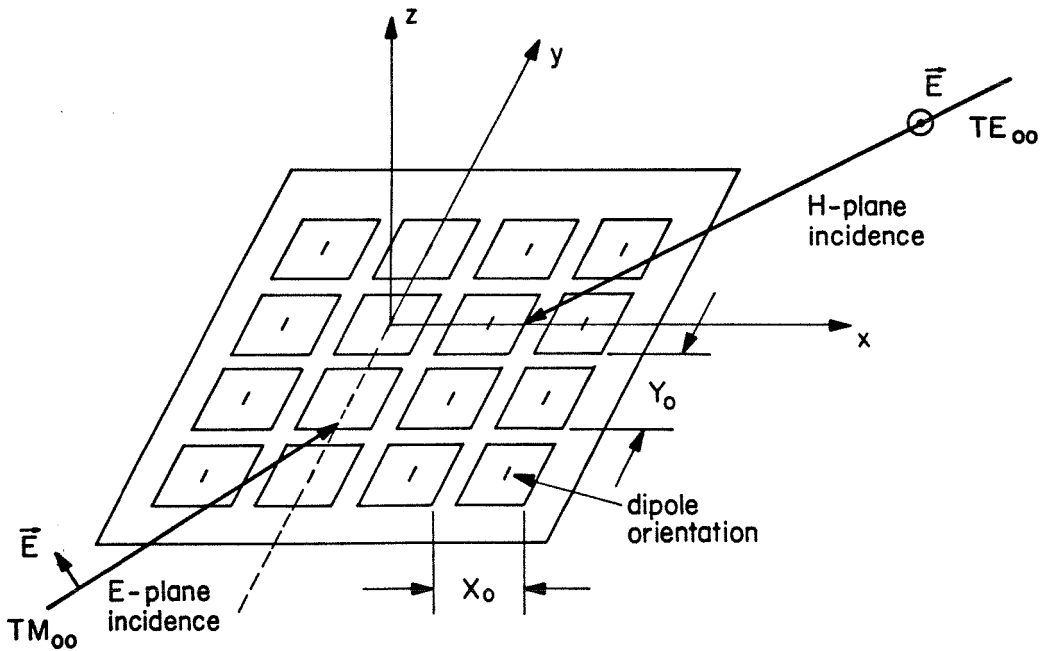


Figure 14. Incident plane waves for E & H-plane pattern calculation.

where p , γ_{mn}^{pf} , Y_{mn}^{pf} and \vec{e}_{mn}^{pf} are in the same notation as the fields in waveguide section (1). The orthonormalized set of eigenvectors \vec{e}_{mn}^{pf} are derived from the plane-wave potential function

$$\Psi_{mn} = e^{\alpha_m x + \beta_n y \pm \gamma_{mn} z} \quad (2.15)$$

where

$$\begin{aligned} \alpha_m &= \alpha_0 + \frac{2m\pi}{X_0} \\ \beta_n &= \beta_0 + \frac{2n\pi}{Y_0} \\ \gamma_{mn} &= \sqrt{k_0^2 - \alpha_m^2 - \beta_n^2} \end{aligned} \quad (2.16)$$

$(\alpha_0, \beta_0, \gamma_{00})$ is the vector propagation constant of the incident wave, $k_0 = \frac{2\pi}{\lambda}$, and (X_0, Y_0) are the periods of the array on the x and y directions, respectively. The same method outlined above is used to match the fields in air to the fields in C_0 . The coefficients of the fields in waveguide section C_0 can be related to the coefficients of the fields in air through the matrix equation

$$\begin{pmatrix} F & F \\ Y_0 & -Y_0 \end{pmatrix} \begin{pmatrix} a_0 \\ b_0 \end{pmatrix} = \begin{pmatrix} I & I \\ -F^T Y_f & F^T Y_f \end{pmatrix} \begin{pmatrix} a_f \\ b_f \end{pmatrix} \quad (2.17)$$

where I is a unit matrix, Y_0 and Y_f are diagonal admittance matrices of the individual waveguide and Floquet modes, and (a_0, b_0) and (a_f, b_f) are the coefficients of the incident and reflected fields for C_0 and air, respectively. F is a matrix of the scalar product between a TE/TM eigenvector in waveguide section C_0 and a TE/TM Floquet eigenvectors in air, given by

$$F_{mnMN}^{p1pf} = \int_{A_0} \vec{e}_{mn}^{p1} \cdot \vec{e}_{MN}^{pf} dA_0 \quad (2.18)$$

F could be considered as the coupling coefficient between a Floquet mode and a waveguide mode. The incident field is a plane wave of unit amplitude and its coefficients a_{00}^{pf} are known. The coefficients of the reflected Floquet modes b_{mn}^{pf} , and the coefficients of the waveguide modes a_{mn}^{p0} and b_{mn}^{p0} can be calculated in

terms of the coefficients of the incident field. The incident field is a TM_{00} plane wave for the E-plane pattern calculations, and a TE_{00} plane wave for the H-plane pattern (Fig. 14). The fields in the membrane section, and thus the antenna pattern, can be calculated using the horn matrix \mathbf{H} derived above.

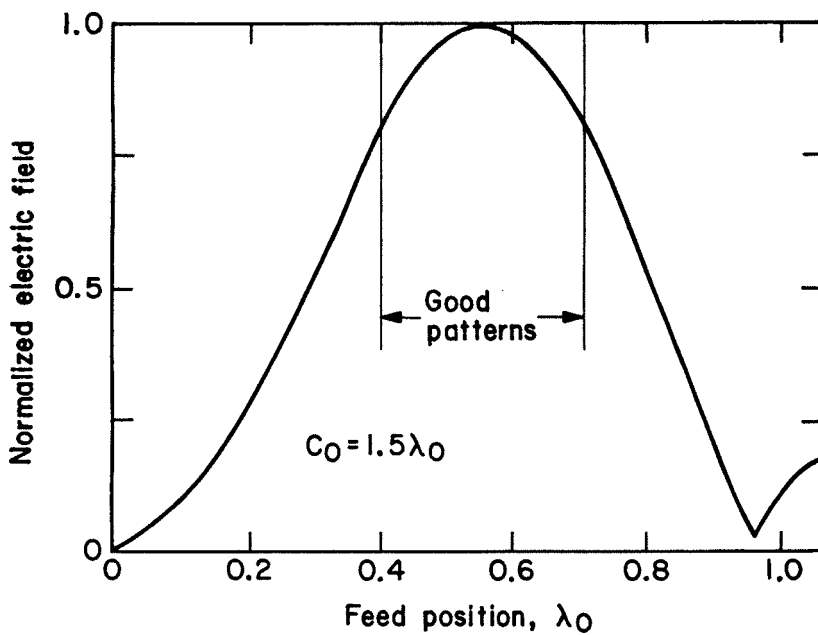


Figure 15. The fields at the horn axis for a plane wave incident normal to the aperture. The opening of the horn array is 1.5λ .

2.5 Design of the Horn Structure

The position of the antenna inside the horn, the dimensions of the horn, and the coupling to the dipole are the parameters one has to consider in this design. The fields along the horn axis have to be known to find the position at which the antenna is to be placed. The larger the fields, the greater the radiation resistance will be. But this is not the only criterion. The pattern has to be a good feed-pattern for an imaging system. Figure 15 shows the normalized electric field along the horn axis for a plane wave incident normal to a 1.5λ square horn array. At a feed position smaller than 0.35λ , the membrane cross-section is smaller than

0.5λ , and the fields decrease uniformly because all the waveguide modes are in the cut-off region. There is also a de-focussing effect around a feed position of 0.92λ . The patterns calculated at feed positions of 0.42λ , 0.56λ and 0.71λ show good horn patterns. This shows the wide bandwidth of the horn. The pattern at 0.42λ was better than the pattern at 0.56λ . This shows that the point of maximum radiation resistance is not necessarily the point which gives the best radiation pattern. This radiation resistance is a qualitative number, because it is calculated for an infinitesimal dipole.

The theory developed above is valid for horns with any rectangular cross-section, having an arbitrary separation between the horn apertures. The only condition is that the array is periodic and infinite in extent. A computer program was written for an IBM AT to calculate the patterns. The code was written in Turbo Pascal. Selection of the appropriate step height and the number of waveguide modes is important. The horn was modelled by 50 steps per wavelength, the smallest section C_s being 0.2λ . In the case of E and H-plane pattern calculations, only certain waveguide modes are excited because of symmetry. The pre-selection of these modes greatly reduces the computation time. All relevant modes were considered up to $M = N = 7$. The separation gap between two horn openings on the front wafer can vary between 0.02λ to 0.05λ depending on the alignment accuracy. The patterns were calculated for square apertures, with the periods of the two-dimensional array, X_0 and Y_0 , taken equal to the horn aperture C_0 . The error in neglecting the separation is small, since the horn aperture C_0 is between 1.0λ and 2.0λ . The horn sidewalls are assumed to be lossless. The following tests were conducted to check the accuracy of the results :

- (1) Conservation of power — The sum of power in the reflected modes should be equal to the power in the incident modes. This is true because the infinitesimal dipole does not absorb any power, and the walls are assumed to be lossless.

- (2) **Boundary conditions** — The fields at C_0 calculated from the waveguide-modes representation should match the fields calculated from the Floquet-modes representation.
- (3) **Reciprocity theorem** — The coupling between any two Floquet modes should remain the same if the incident and reflected modes are interchanged.

The experimental patterns will be measured with a quarter-wave dipole on the membrane. So, how is it that the theoretical horn patterns with an infinitesimal-dipole feed will be compared with the experimental ones? To answer this fundamental question, let us look at the Lorentz reciprocity theorem, assuming the absence of any magnetic sources

$$\int_V \vec{\mathbf{E}}^b \cdot \vec{\mathbf{J}}^a dV = \int_V \vec{\mathbf{E}}^a \cdot \vec{\mathbf{J}}^b dV \quad (2.19)$$

where V is a finite volume containing all the sources, and $\vec{\mathbf{E}}^a$ and $\vec{\mathbf{E}}^b$ are the fields in volume V arising from the sources $\vec{\mathbf{J}}^a$ and $\vec{\mathbf{J}}^b$, respectively. The current in a quarter-wave dipole peaks at the center, but goes to zero at the ends. It is similar, to a good approximation, to the current of an infinitesimal dipole which peaks at the center and is constant throughout the dipole. This is why the patterns in free space of both antennas are very similar. Therefore, by the reciprocity theorem, the horn pattern with an infinitesimal-dipole feed will be similar to that with a quarter-wave dipole feed. The power absorbed in the quarter-wave dipole is much greater than that in an infinitesimal dipole. However, the pattern of any antenna is the same if it is matched or not, and thus the power absorbed does not have any effect on the pattern.

2.6 Design of the Dipole Antenna

Imaging arrays with square horn apertures of 1.0λ , 1.45λ and 2.1λ were fabricated for 242 GHz, and a 1.0λ array was fabricated for 93 GHz. In all cases, the

membrane cross-section was around 0.55λ . There are several advantages for choosing a small membrane. First, the fabrication on small membranes has higher yields than on larger ones, and the available space for processing electronics increases considerably with the choice of smaller membranes. The membrane size was $680 \times 680 \mu\text{m}$ for 242 GHz, and $1.8 \times 1.8 \text{ mm}$ for 93 GHz. Second, is the ease of designing a low-pass filter with a half-wavelength membrane. As shown in Fig. 16, the coplanar strips are designed to have a characteristic impedance of 200Ω when suspended on the membrane, (calculated from the quasi-static solution to coplanar strips in free space [36]) and an impedance of 4Ω when sandwiched between two silicon wafers. The quarter-wave section of coplanar strips transforms the 4Ω impedance into a very large impedance at the dipole apex. The bolometer presents there a much lower impedance, and therefore absorbs all the received power. The coplanar strips also provide a dc-bias line and a low-frequency connection to the bolometer.

In order to have optimal power transfer, the bolometer resistance should be matched to the antenna impedance. Also, the antenna must be resonant at the design frequency, that is antenna impedance must be purely resistive. The impedance of a cylindrical antenna in free space [33, pp. 301–305] having a circular cross section of radius a , is given by

$$Z = [122.65 - 204.1(kl) + 110(kl)^2] - j[120(\ln \frac{2l}{a} - 1) \cot(kl) - 162.5 + 140(kl) - 40(kl)^2] \quad (2.20)$$

where l is the half-length of the dipole, and $k = \frac{2\pi}{\lambda}$. This approximation is accurate in the range $1.3 \leq kl \leq 1.7$ and $0.001588 \leq a/\lambda \leq 0.009525$. For a strip antenna with a rectangular cross-section, the effective radius is

$$a_e = \frac{1}{4}(w + t) \quad (2.21)$$

where t and w are the thickness and width of the strip, respectively. The dipole antenna on the membrane is designed to have a resonant free-space impedance of

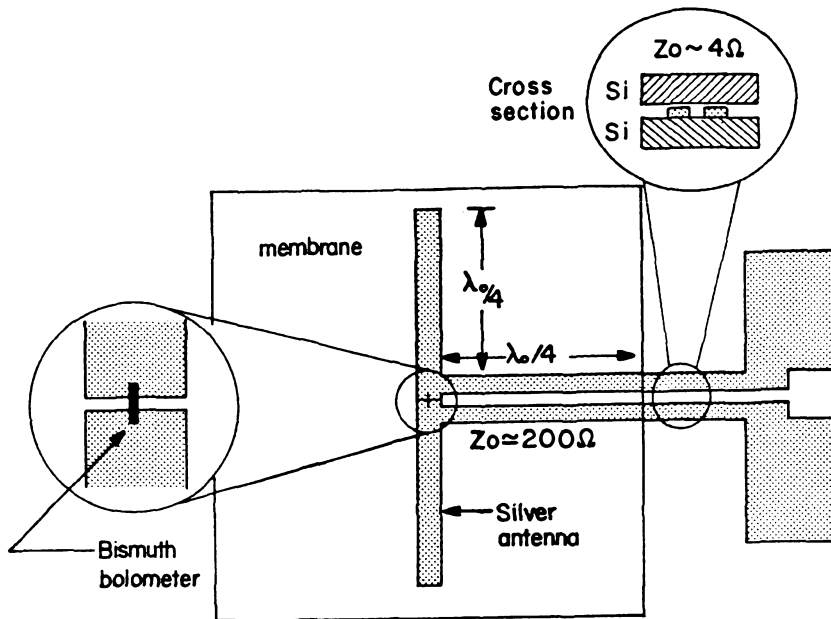


Figure 16. A quarter-wave dipole with a low-pass filter on the membrane.

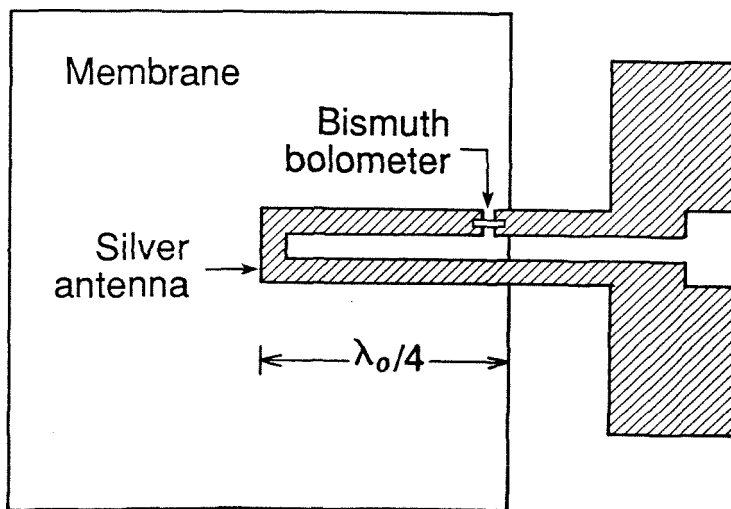


Figure 17. A quarter-wave folded monopole on the membrane. This antenna does not require a low-pass filter.

60 Ω at 93 GHz and 242 GHz. The impedance of the antenna *inside* the pyramidal cavity can be calculated by solving a Pocklington integral equation involving the current on the dipole and the near-field boundary conditions presented by the cavity. This is not within the scope of this research. The free-space impedance is used as an estimate for choosing the bolometer resistance for a good match. The true antenna resistance may vary by as much as half or twice the free-space value. The dipole antenna may also have a strong reactive component due to the back-shortening cavity. Impedance measurements on a 7.3 GHz scale model are presented in Chap. 3.

In case of a folded monopole, the coplanar strips imbedded in silicon provide a near RF short-circuit, and the tip of the antenna reaches the center of the membrane (Fig. 17). The antenna loop forms the RF circuit and allows the dc-bias and low-frequency connection to the bolometer. The antenna dimensions are chosen using available design rules [37]. The folded-monopole impedance in free space is around 120 Ω . The advantage of the monopole design is that it allows the integration of a complex detector, such as the GaAs Schottky diode, on the supporting wafer and not on the center of the membrane.

References

- [1] E. K. Reedy, G. W. Ewell, "Millimeter Radar," in *Infrared and Millimeter Waves*, vol. 4, pp. 23–94, K. J. Button Ed. Academic Press, New-York, 1983.
- [2] K. Miyanchi, "Millimeter-wave communications," *Infrared and Millimeter Waves*, Chap. 1, pp. 1–94, K. J. Button, ed., Academic Press, New York, 1983.
- [3] P. E. Young, D. P. Neikirk, P. P. Tong, D. B. Rutledge, and N. C. Luhman, "Multichannel far-infrared imaging for fusion plasmas," *Rev. Sci. Instruments*, vol. 56, pp. 81–89, 1985.
- [4] T. G. Phillips and D. B. Rutledge, "Superconducting tunnel detectors in radio astronomy," *Scientific American* vol. 254, pp. 96–102, 1986.
- [5] M. J. Wengler, D. P. Woody, R. E. Miller, and T. G. Phillips, "A low-noise receiver for millimeter and submillimeter waves," *Int. J. of Infrared and Millimeter Waves*, vol. 6, pp. 697–706, 1985.
- [6] W. J. Wilson, R. J. Howard, A. C. Ibbott, G. S. Parks and W. B. Ricketts, "Millimeter-wave imaging sensor," *IEEE Trans. Microwave Theory Tech*, vol. 34, pp. 1026–1035, 1986.
- [7] J. P. Hollinger, "A versatile millimeter-wave imaging system," *IEEE Trans. Microwave Theory Tech*, vol. MTT-24, pp. 786–793, 1976.
- [8] C. Zah, D. P. Kasilingam, J. S. Smith, D. B. Rutledge, T. Wang, and S. E. Schwarz, "Millimeter-wave monolithic Schottky diode imaging arrays," *Int. J. of Infrared and Millimeter Waves* 6, pp. 981–997, 1985.
- [9] D. B. Rutledge, D. P. Neikirk, and D. P. Kasilingam, "Integrated-circuit antennas," in *Infrared and Millimeter Waves*, vol. 10, K. J. Button ed., Academic Press, New York, 1983, pp. 1–90. (Note: The argument k of the elliptic functions of equation (23) should be $\tan^2(45^\circ - \theta/4)$, rather than $\tan(45^\circ - \theta/4)$, where θ refers to the full bow angle.)

- [10] R. C. Compton, R. C. McPhedran, Z. Popović, G. M. Rebeiz, P. P. Tong and D. B. Rutledge, "Bow-tie antennas on a dielectric half-space: Theory and experiment," *IEEE Trans. Antennas Propagat.*, vol. AP-35, pp. 622-631, June 1987.
- [11] D. B. Rutledge and M. S. Muha, "Imaging antenna arrays," *IEEE Trans. Ant. Propag.*, vol. AP-30, pp. 535-540, July 1982.
- [12] K. Lee and M. Frerking, "Planar antennas on thick dielectric substrates," *12'th Int. Conf. Infrared Millimeter Waves*, pp. 216-217, Lake Buena Vista, Dec. 1987.
- [13] G. W. Chantry, J. W. Flemming, P. M. Smith, "Far-infrared and millimeter-wave absorption spectra of some low-loss polymers," *Chemical Physics letters*, vol. 10, pp. 473-477, 1971.
- [14] M. N. Afsar, "Dielectric Measurements of Millimeter-Wave Materials," *IEEE Trans. Microwave Theory Tech.*, vol. MTT-32, pp. 1598-1609, 1984.
- [15] G. M. Rebeiz, W. G. Regehr, D. B. Rutledge, R. L. Savage, and N. C. Luhmann Jr., "Submillimeter-wave antennas on thin membranes," *Int. J. Infrared Millimeter Waves*, vol. 8, pp. 1249-1255, October 1987.
- [16] J. W. Goodman, "Introduction to Fourier Optics", pp. 4-21, McGraw Hill, New York, 1968.
- [17] M. Born and E. Wolf, "Principles of Optics," pp. 484-486, Pergamon Press, Oxford, 1980.
- [18] J. Ruze, "Lateral feed displacement in a paraboloid," *IEEE Trans. Ant. Propag.*, vol. AP-13, pp. 660-665, Sept. 1965.
- [19] A. R. Gillespie and T. G. Phillips, "Array detectors for millimeter line astronomy," *Astronomy and Astrophysics*, vol. 73, pp. 14-18, 1979.

- [20] B. E. Deal and A. S. Grove, "General relationship for the thermal oxidization of silicon", *J. Applies Physics*, vol. 36, pp. 3770–3778, Dec. 1965.
- [21] A. Reisman *et al.*, "The controlled etching of silicon in catalized ethylene-diamine-pyrocatechol-water solutions," in *J. Electrochemical Soc.*, vol. 126, pp. 1406–1425, 1979.
- [22] K. E. Peterson, "Silicon as a mechanical material", *Proc. IEEE*, vol. 70, pp. 420–457, May 1982.
- [23] K. E. Bean, "Anisotropic etching of silicon", *IEEE Trans. Electron Devices*, vol. ED-25, pp. 1185–1193, October 1978.
- [24] D. W. Hess, "Plasma-enhanced CVD: Oxides, nitrides, transition metals, and transition silicides", *J. Vac. Sci. Technol.* vol. 2, pp. 244–252, Apr–June 1984.
- [25] M. Sekimoto, H. Yoshihara, and T. Ohkubo, "Silicon nitride single-layer x-ray mask", *J. Vac. Sci. Technol.*, vol. 21, pp. 1017–1021, Nov–Dec 1982.
- [26] S. Timoshenko and S. Woinowsky-Krieger, "Theory of Plates and Shells," McGraw Hill, New York, 1959.
- [27] Pacific Western Systems, Model GL-450G-L-450 Coyote.
- [28] L. I. Maissel and R. Glang, "Handbook of thin film technology", pp. 12-21 to 12-30, McGraw-Hill, New York, 1970.
- [29] A. W. Love, "Electromagnetic Horn Antennas," IEEE Press, New York, 1976.
- [30] H. Patzelt and F. Arndt, "Double-plane steps in rectangular waveguides and their applications for transformers, irises and filters", *IEEE Trans. Microwave Theory Tech.*, vol MTT-30, pp. 771–776, May 1982.
- [31] J. A. Encinar, J. M. Rebollar, "A hybrid technique for analysing corrugated and non-corrugated rectangular horns", *IEEE Trans. Antennas Propagat.*, vol. AP-34, pp. 961–968, Sept. 1986

- [32] N. Amitay, V. Galindo, and C. P. Wu, "Theory and Analysis of Phased Array Antennas", pp. 37-44, Wiley-Interscience, New York, 1972.
- [33] R. S. Elliott, "Antenna Theory and Design", pp. 41-46, Prentice-Hall, Englewood Cliffs, 1981.
- [34] R. F. Harrington, "Time-Harmonic Electromagnetic Fields," McGraw-Hill, New York, 1961.
- [35] R. F. Harrington, "Fields Computation by the Methods of Moments", McMillan and Sons, New York, 1968.
- [36] K. C. Gupta, R. Garg, and I. J. Bahl, "Microstrip Lines and Slotlines", pp. 195-213, Artech House, Dedham, Massachusetts, 1979.
- [37] H. Jasik, "Antenna Engineering Handbook," pp. 24-3 to 24-6, McGraw-Hill, New York, 1961.

Chapter 3

Monolithic Two-Dimensional Imaging Antenna Arrays Measurements

The receiving patterns of the horn antennas were measured at 93 GHz and 242 GHz. At 93 GHz, the source was a Varian reflex klystron modulated at 1 KHz with a power output of 80 mW. At 242 GHz, the source was a crossguide-tripler fed by an 80.7 GHz Gunn diode modulated at 1 KHz. The power output of the tripler was about 1 mW. The silver antennas on the membrane were 1000 Å thick. The detectors are bismuth microbolometers [1] with a dc resistance of 130 Ω, and a dc responsivity of 10 V/W at a bias of 100 mV. The horn array was mounted at the center of a two-axis rotation gimbal system. The system is rotated by two computer-controlled stepper motors (Fig. 1). The detected signal is fed to a computer-interfaced lock-in amplifier. The variations in the transmitted power were minimal. Measurements were made in the E and H planes and 45° planes of both the co-polarized and cross-polarized components (Fig. 2). Full two-dimensional scans were also made of the co-polarized component. This is necessary for an accurate measurement of the directivity of the horn antenna. Also, care was taken to reduce the scattering from the antenna and source mounts. Placing absorber to cover the two-axis gimbal mount reduces this scattering, at the expense of shadowing the receiving horn array at large angles. The system was aligned using a He-Ne laser, but the reproducibility of the patterns was not affected by small misalignments.

When measuring the antenna patterns, a 4 × 4 subarray is contacted, and the patterns are measured on at least 4 distinct elements. The elemental patterns are very similar. This was expected since all the pyramidal cavities, antennas and detectors were defined at the same time. No measurements were done on a corner or edge element. The feed antenna to the horn was either a dipole or a folded

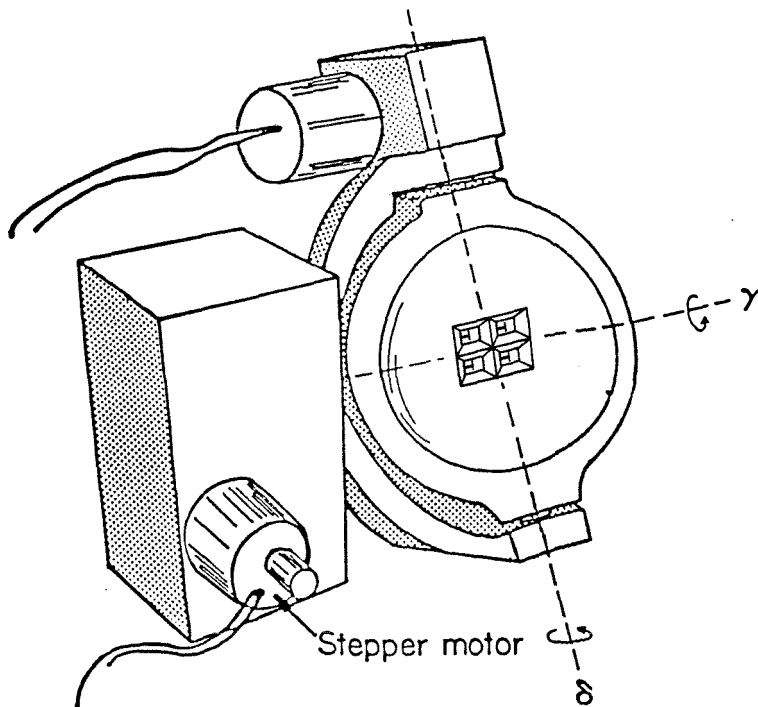
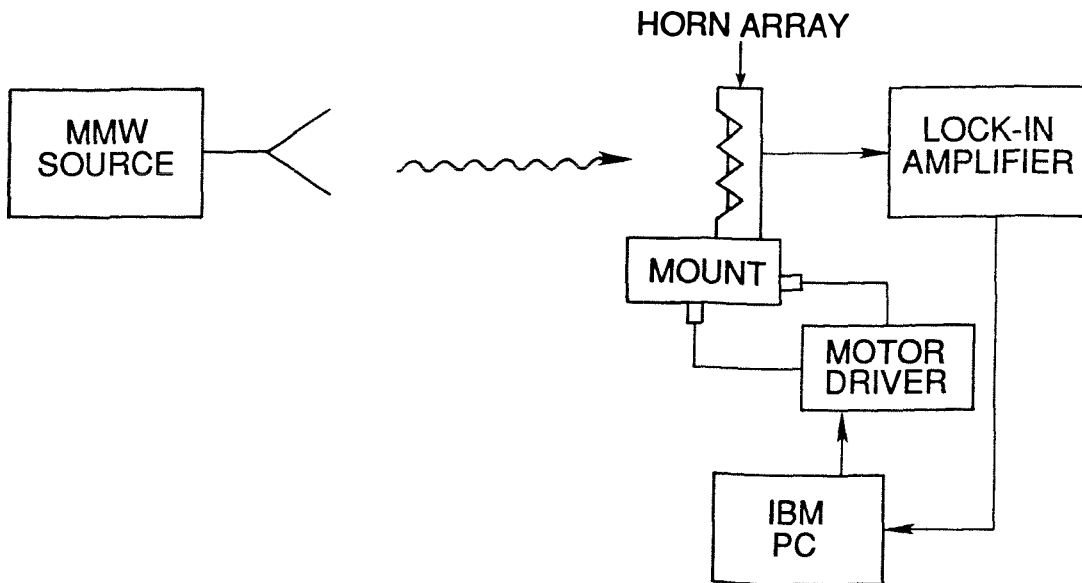


Figure 1. Detailed view of the measuring system (top) and the two-axis gimbal mount (bottom). The horn-array is placed in the far-field of the transmitting horn.

monopole. Both feed antennas gave very similar horn patterns. The patterns of a dipole-fed horn were slightly more symmetrical than a monopole-fed horn.

3.1 Comparison of Theory and Experiment

The measured patterns at 93 GHz and 242 GHz show a good agreement with theory (Fig. 3–6). The measured E-planes of 1.0λ and 1.45λ arrays at 242 GHz do not show any sidelobes. We attribute this discrepancy to losses in the cavity sidewalls, since they were not coated by a gold layer. In contrast, the sidewalls for the 93 GHz array were gold coated, and the measured E-plane at 93 GHz (Fig. 4) on a 1.0λ array shows slight gain suppression at normal incidence and -14 dB sidelobe, exactly as predicted by the theory. The E and H plane patterns of the 1.0λ array measured at 242 GHz and 93 GHz are very similar. This verifies the scaling properties of the horn antenna. The discrepancy in the E-plane pattern of the 2.1λ arrays can also be explained by the large resistive sidewall losses. In this case, the cavity was not gold coated, and the silicon wafer used was lightly doped. The effect of horn-wall losses on the efficiency of the antenna will be presented later in this chapter. The 45° plane patterns were narrower than either the E or H-plane patterns. The reason is because the far-field pattern is the Fourier transform of the aperture distribution [2], and the horn cross-section in the 45° plane is $\sqrt{2}C_0$, larger than the cross-section C_0 in the E and H plane.

The antennas were all linearly polarized with the direction of polarization given by the dipole orientation on the membrane. The cross polarized component at normal incidence was lower than the noise floor, which ranged from -20 dB to -30 dB depending on the quality of the bolometers. There was also no measurable cross-polarized component in either the E or H planes. This is due to the symmetrical structure of the antenna. The 45° cross-polarized patterns were symmetrical to normal incidence, and showed a peak cross-polarized component at $\pm 60^\circ$. A -17.5 dB component was measured at 242 GHz on the 1.45λ imaging array, and a -15 dB

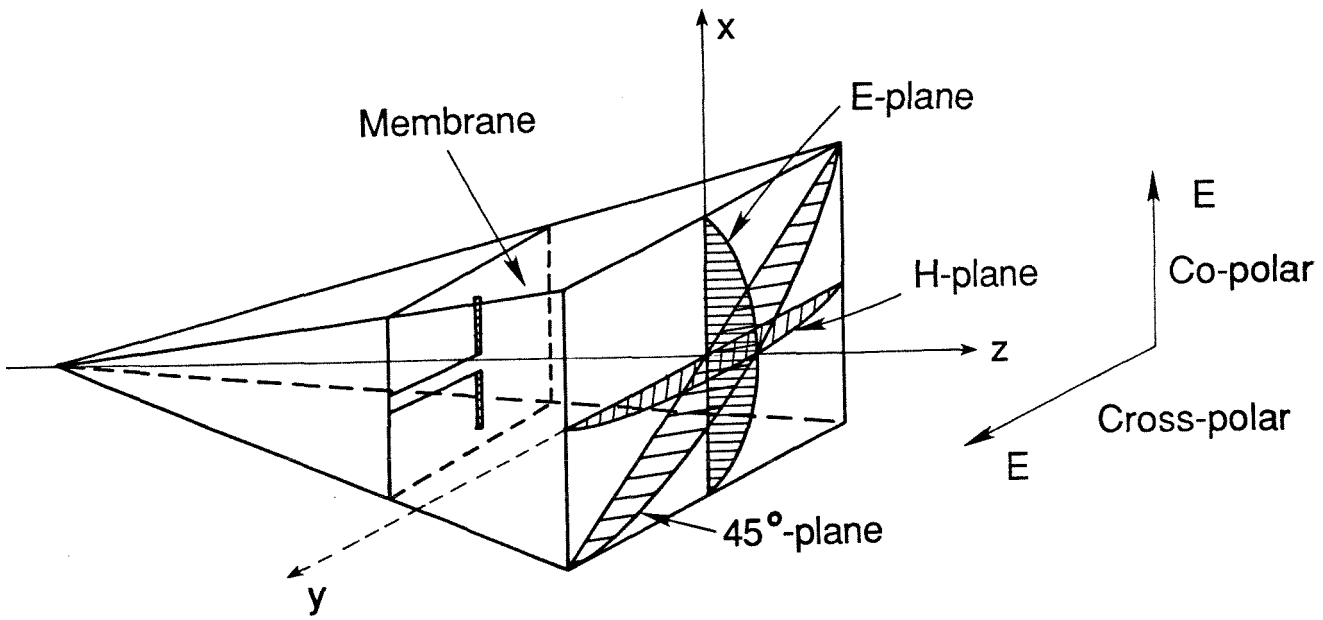


Figure 2. Definition of the co-polarized and cross-polarized E and H-plane patterns, and the 45°-plane patterns.

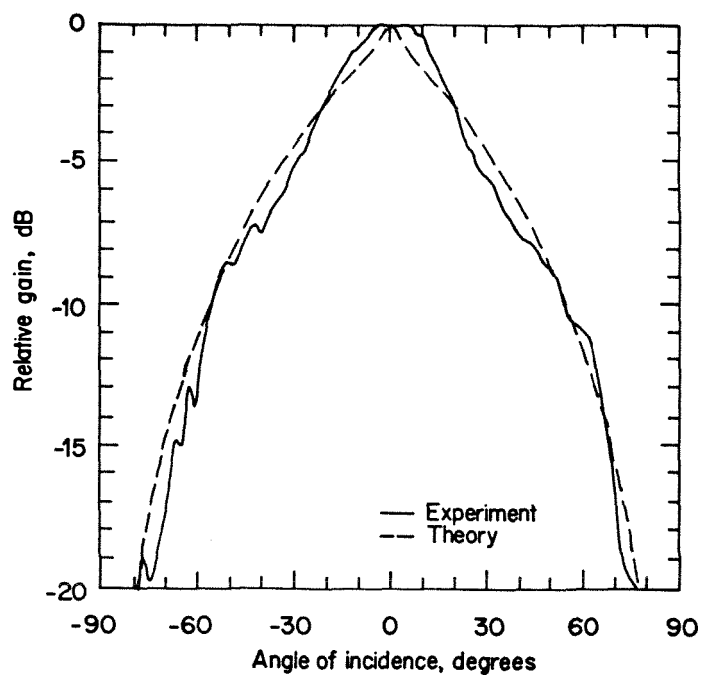
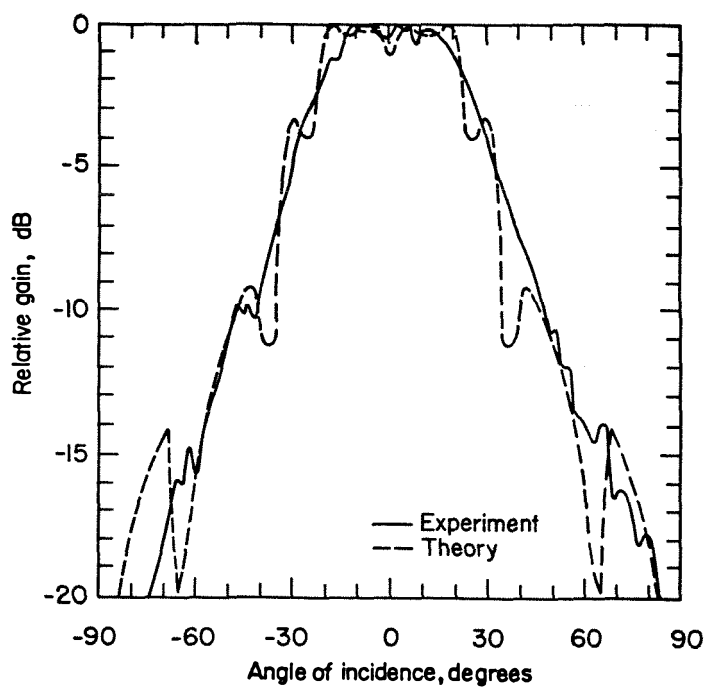


Figure 3. Typical E-plane (top) and H-plane (bottom) patterns measured at 242 GHz on a (12×12) , 1.0λ imaging array. Notice the absence of sidelobes in the E-plane.

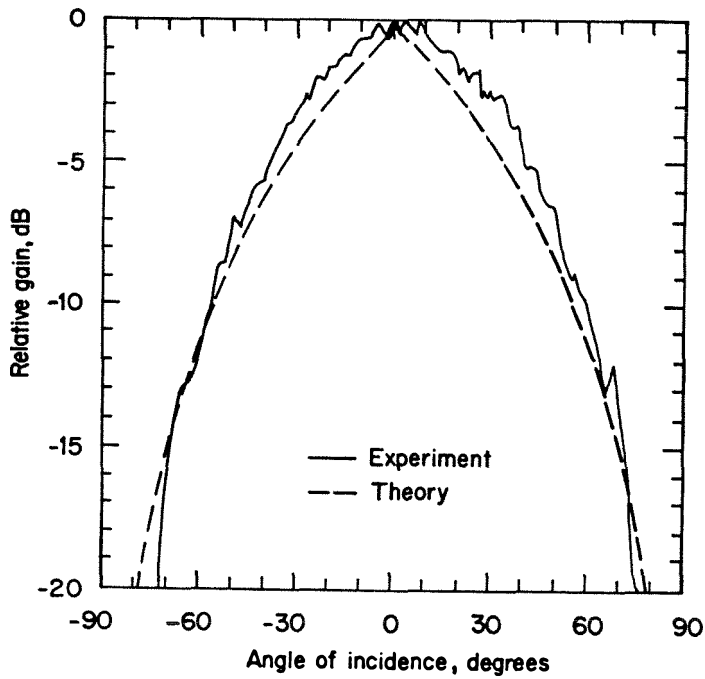
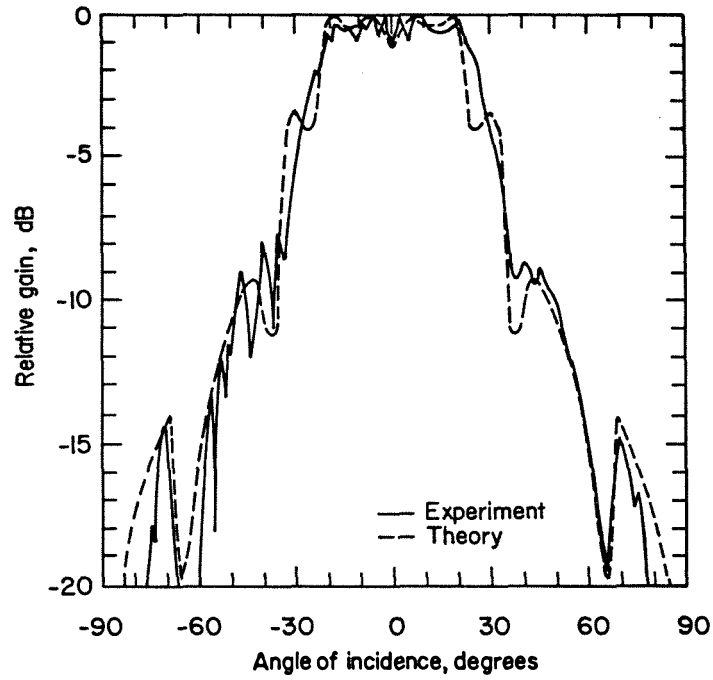


Figure 4. Typical E-plane (top) and H-plane (bottom) patterns measured at 93 GHz on a (7×7) , 1.0λ imaging array. Notice the -14 dB sidelobes in the E-plane.

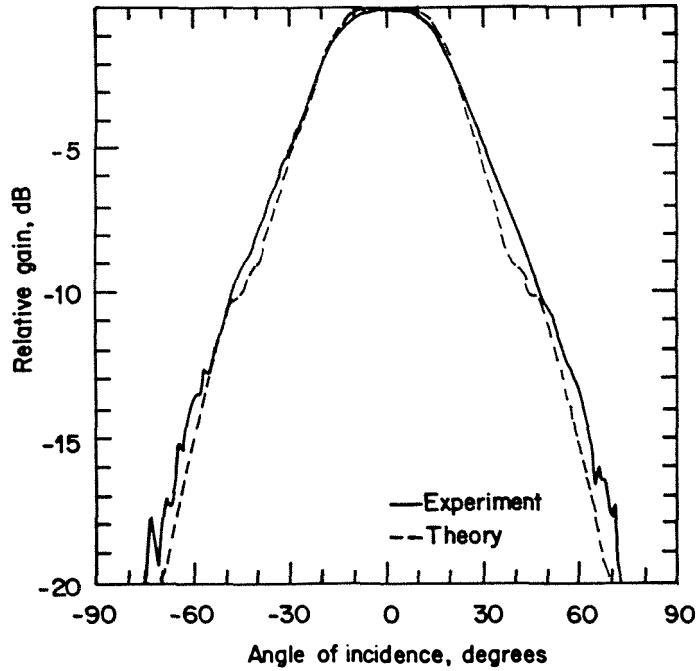
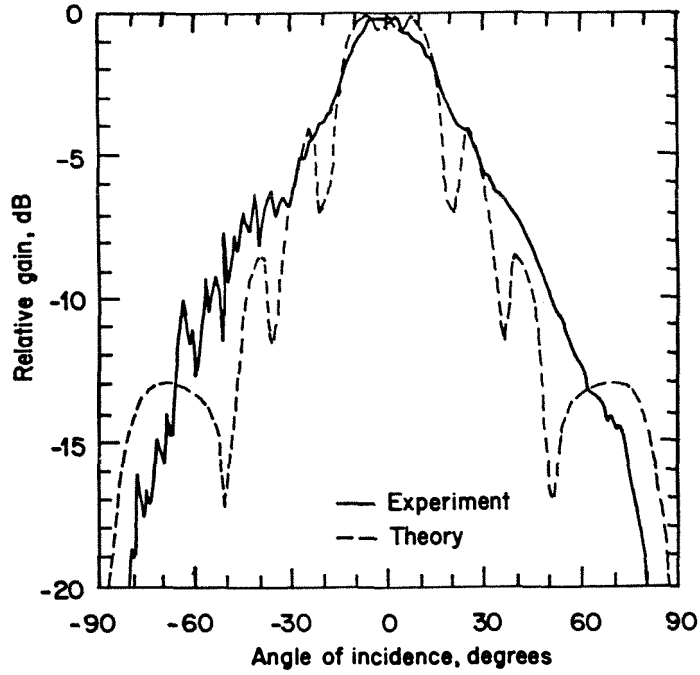


Figure 5. Typical E-plane (top) and H-plane (bottom) patterns measured at 242 GHz on a (9×9) , 1.45λ imaging array. The ripples on the E-plane pattern are due to scattering from the antenna mount.

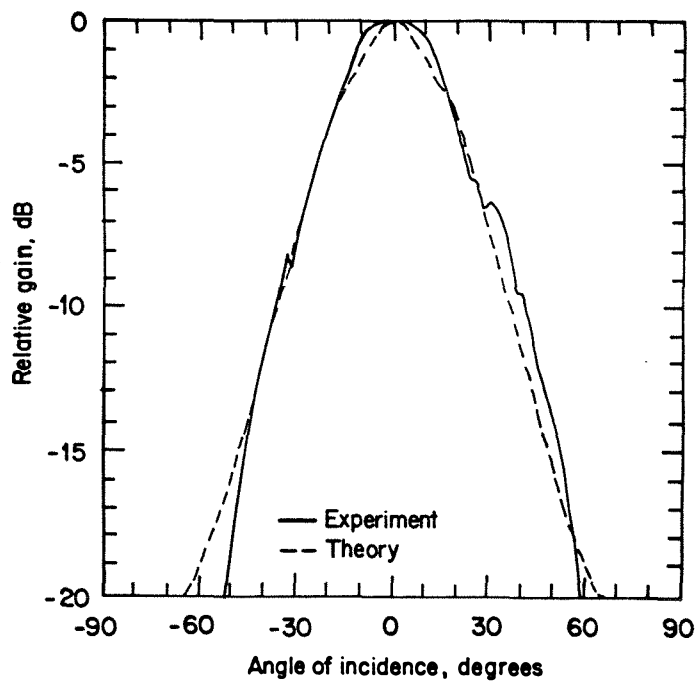
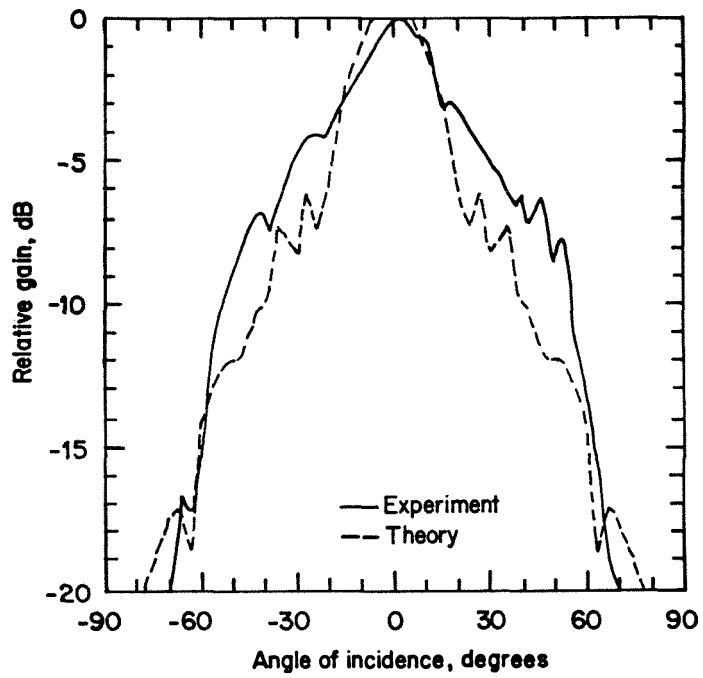


Figure 6. Typical E-plane (top) and H-plane (bottom) patterns measured at 242 GHz on a (7×7) , 2.1λ imaging array.

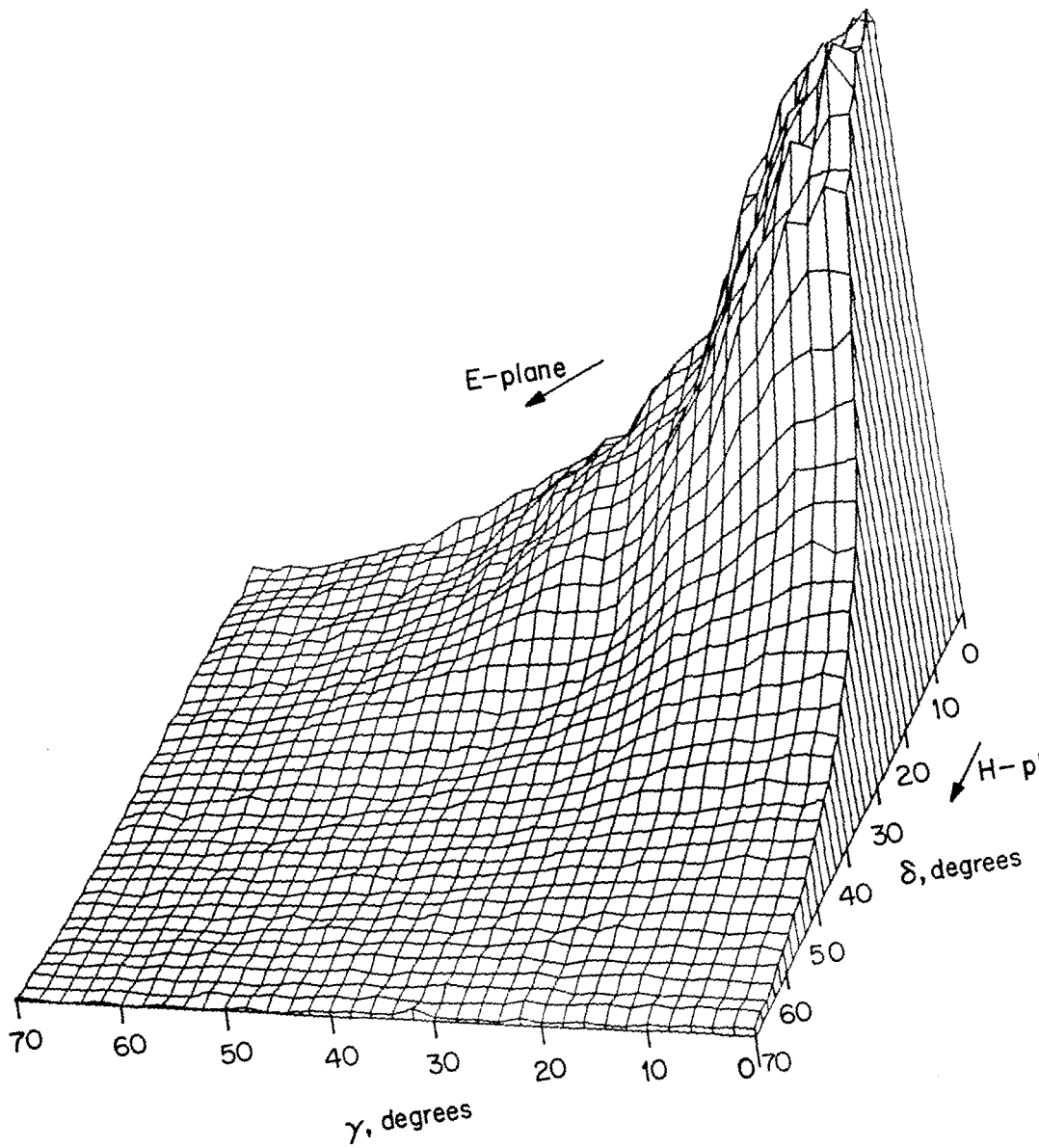


Figure 7. Measured two-dimensional scans of a (9×9) array at 242 GHz. The plot is linear in power.

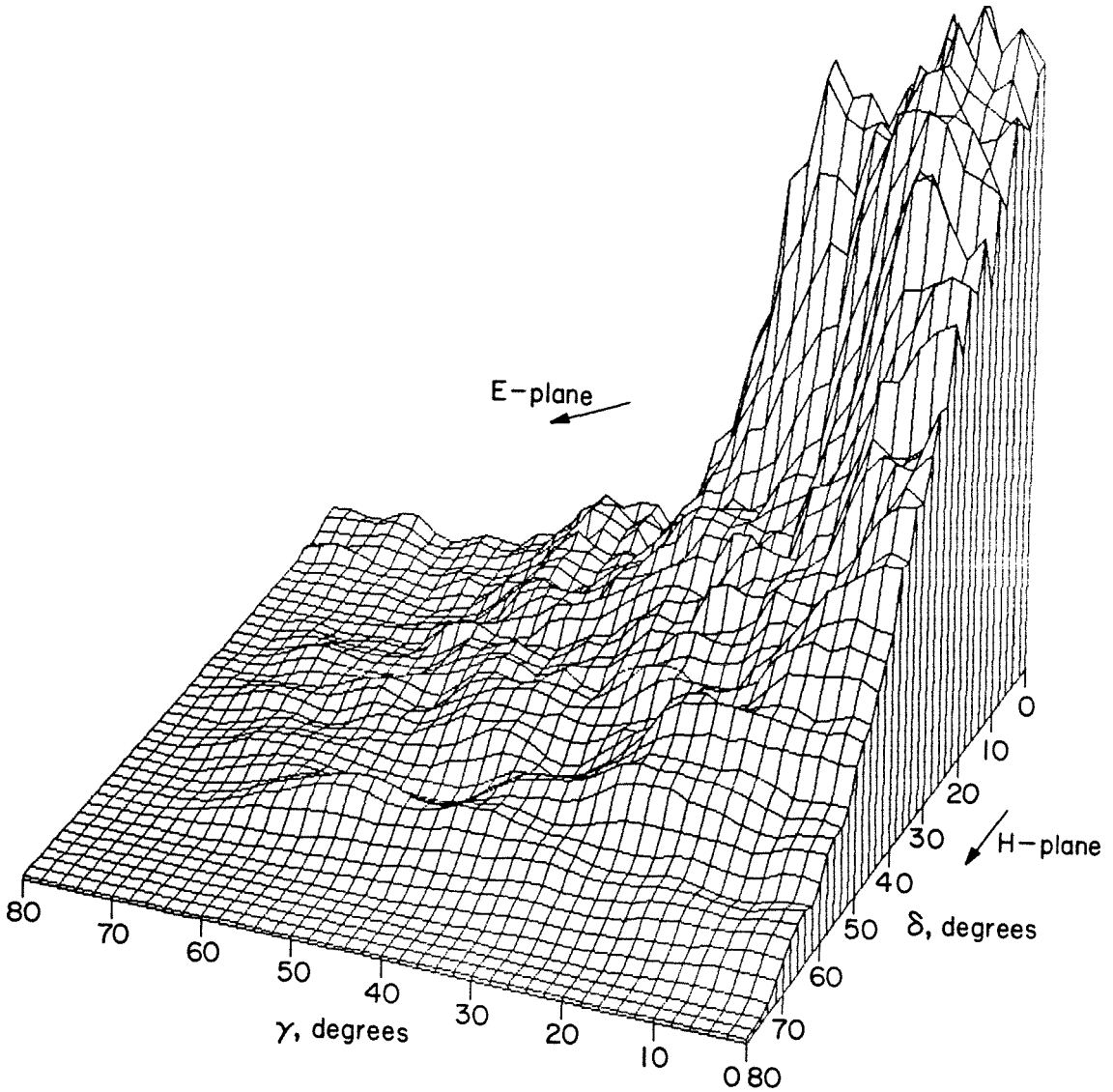


Figure 8. Measured two-dimensional scans of a (7×7) array at 93 GHz. The graph is linear in power. The ripples at 93 GHz are due to scattering from the measurement setup.

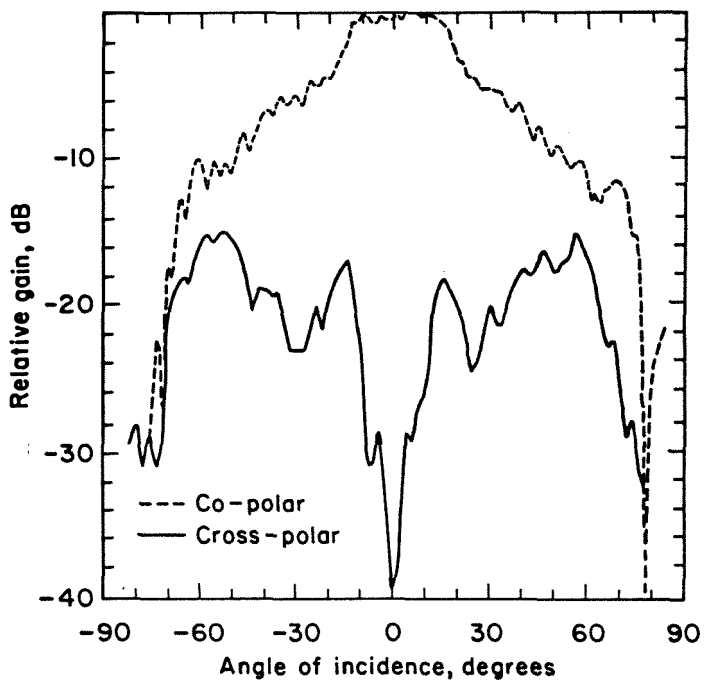
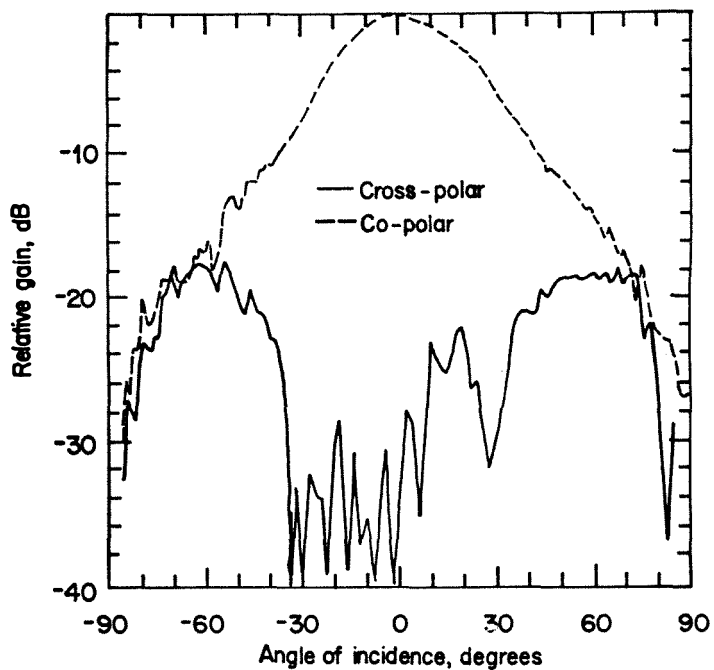


Figure 9. Typical 45° co-polar and cross-polar plane patterns measured at 242 GHz on a (9×9) , 1.45λ imaging array (top), and at 93 GHz on a (7×7) , 1.0λ imaging array (bottom).

level was measured on the 1.0λ array at 93 GHz (Fig. 9).

Tabulated in Fig. 10 are the exact dimensions of the imaging arrays, with the corresponding measured 3-dB and 10-dB beamwidths of the E and H-plane patterns. The H-plane pattern is well behaved, while the E-plane pattern shows sidelobes. This is due to the boundary condition at the horn aperture C_0 . The electric field is tangential to the sidewall in the H-plane scan, resulting in a distribution with a peak at the center and a null at the boundary. On the other hand, the electric field is normal to the sidewall in the E-plane scan, resulting in a large component at the boundary. Also, the H-plane pattern narrows with increasing aperture size, while the E-plane pattern stays the same after 1.45λ . This is also due to the far-field pattern being the Fourier transform of the aperture distribution.

The co-polarized peak directivity of the horn antenna is defined as

$$D = \frac{4\pi}{\int_0^{2\pi} \int_0^{\frac{\pi}{2}} P_{co-p} \sin \theta \, d\theta \, d\phi} \quad (3.1)$$

where P_{co-p} is the normalized co-polarized radiation pattern of the antenna. The effect of the cross-polarized component will be presented later in this chapter. The aperture efficiency ϵ_{ap} , defined as the effective aperture of the horn antenna divided by the physical aperture size, is given by

$$\epsilon_{ap} = \frac{\left(\frac{\lambda^2}{4\pi}\right) D}{C_0^2} \quad (3.2)$$

In physical terms, the aperture efficiency denotes the power received by a matched load divided by the total power incident on the horn aperture. The aperture efficiency of a uniformly illuminated antenna with no phase errors is 100% [3]. The calculated directivities from the two-dimensional scans show a decreasing horn-aperture efficiency with increasing aperture size. From a transmitting point of view, a horn with a large aperture is not uniformly illuminated by the dipole and suffers from aperture taper (non-uniform field distribution) and phase errors. In

Array	1.0λ	1.45λ	2.1λ
f	94 GHz	242 GHz	242 GHz
C_o	1.01	1.42	2.09
l	0.02	0.03	0.02
S_{mbr}	25%	13.5%	7.5%
E(3-dB)	54°	35°	35°
E(10-dB)	100°	95°	97°
H(3-dB)	62°	46°	32°
H(10-dB)	110°	90°	70°
D_{cp}	11.9	17.3	21
ϵ_{cp}	95%	97%	38%

Figure 10. Measured 3-dB and 10-dB beamwidths of several millimeter-wave imaging arrays. l is the separation between two openings C_o , and S_{mbr} is the percentage of the space on the wafer occupied by the membranes and the antennas.

practice, the measured aperture efficiency is lower than the one calculated above due to mismatch, resistive and cross-polarization losses.

3.2 Phased-Array Applications

The horn arrays have potential applications in millimeter-wave phased-array systems. The amplifiers and phase shifters could be integrated directly near the radiating element on a GaAs substrate. The GaAs substrate could be sandwiched between two silicon wafers (Fig. 11), and appropriately etched using reactive ion etching [4] or wet chemical etching [5] to produce a horn with smooth sidewalls. The silicon wafers offer mechanical rigidity and the electromagnetic focussing effect. Amitay, Galindo and Wu have analysed waveguide phased arrays in their authoritative text [6]. The radiating element in a phased array should be smaller than a wavelength in order to avoid grating lobes. The element patterns of the 1.0λ array designed for 93 GHz were measured at 80.7 GHz (Fig. 12). The membrane cross-section is 0.48λ , which puts it slightly in the cutoff region. The aperture size is 0.86λ , which is acceptable for a phased array scanned $\pm 10^\circ$. If scanned further, grating lobes would appear in the endfire directions [7]. The theoretical horn aperture efficiency was 94%, calculated from a two-dimensional scan. This result, together with the 1.0λ results, shows that horn arrays smaller than a wavelength have an aperture efficiency near 100% and give good patterns for phased array applications.

A 0.75λ horn array can be readily built at 60 GHz for a $\pm 20^\circ$ scanned phased array. If the antenna is located on a 0.5λ membrane, the total space occupied by the antenna is only 44% of the area of a unit cell. The space available for the supporting electronics of a single antenna is 7.8 mm^2 . A single stage IF amplifier could be integrated on 1.6 mm^2 with the current state of the art [8], and a variable phase shifter on 4 mm^2 . This leaves plenty of room for interconnections and processing electronics.

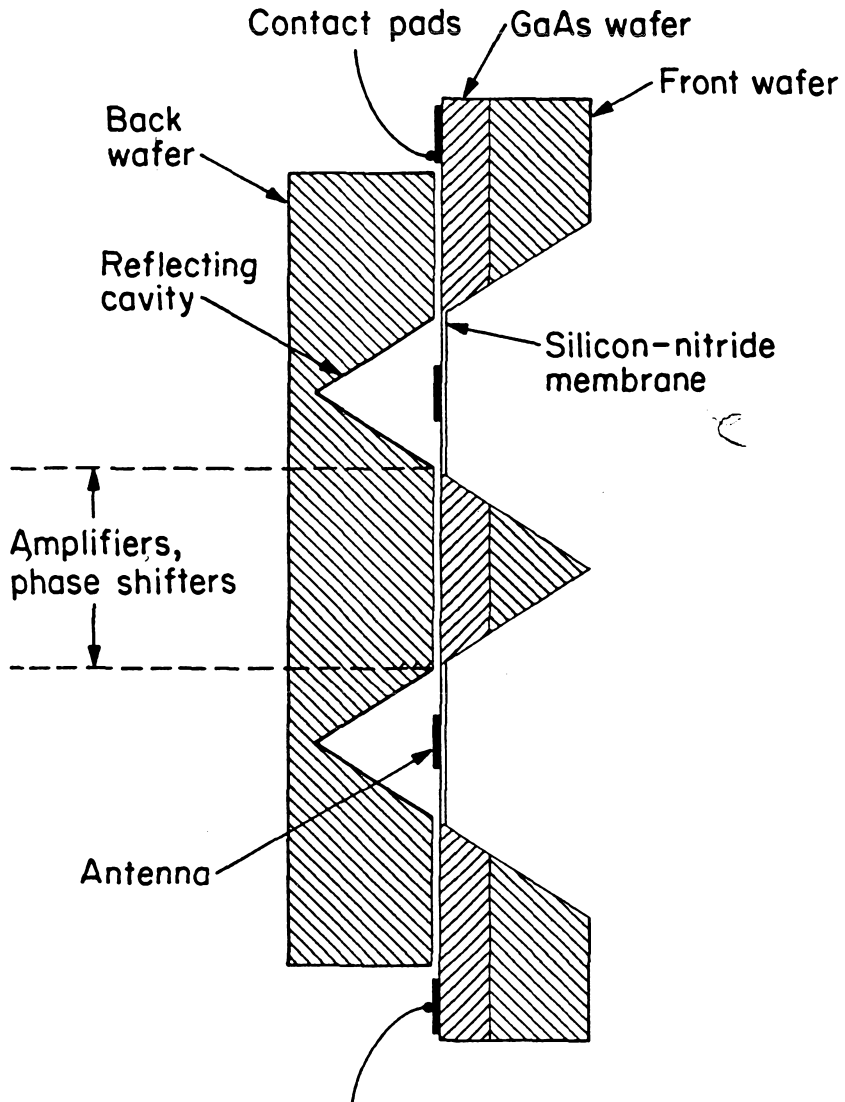


Figure 11. Side view of a phased array, showing the GaAs wafer sandwiched between two silicon wafers.

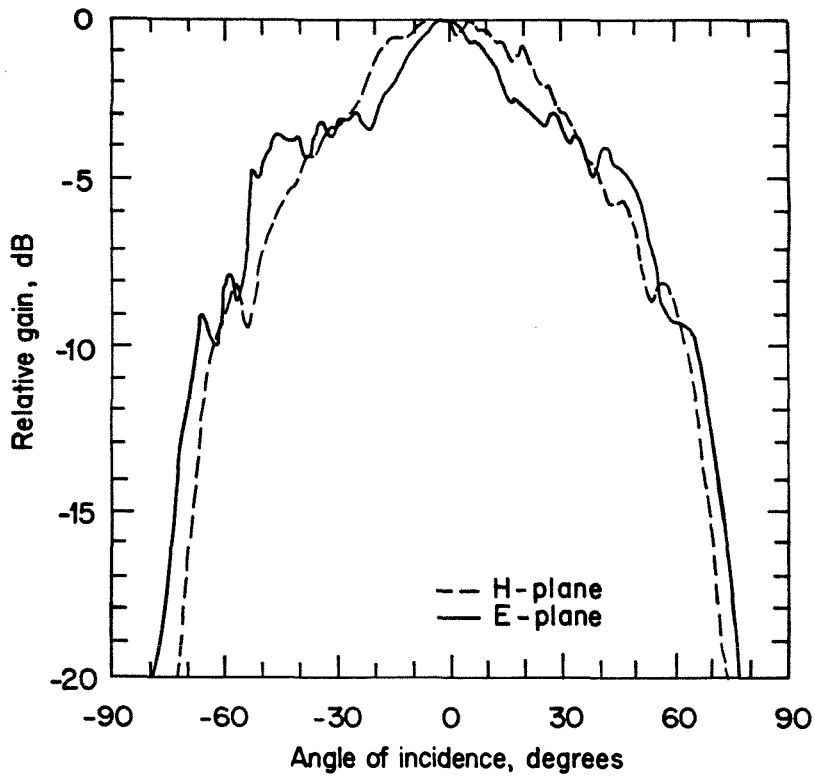


Figure 12. The E and H-plane patterns measured at 80.7 GHz of a single element in a 0.86λ imaging array.

3.3 Microwave Scale-Model Measurements

Measurements on a 3×3 horn-array microwave scale model were done around 7.3 GHz to determine the impedance of the dipole antenna inside the pyramidal cavity [9]. The coaxial line feeds a dipole antenna and a coplanar-strip transmission line which is shorted $\lambda/4$ away from the feed (Fig. 13). This design has two purposes. It models the coplanar strips on the membrane effectively, and it provides an effective Balun [10] for the coax-dipole feed.

The radiation impedance of a coaxial-fed quarter-wave dipole over an $8.0\lambda \times 8\lambda$ ground plane was measured at 7.3 GHz. Similar measurements were done on several quarter-wave dipoles inserted inside the horn-array scale model. The dipoles are placed at a feed position of 0.4λ from the horn apex, which corresponds to a membrane size of 0.56λ . This is the exact position of the antenna inside the 93 GHz horn array. As seen in Fig. 13, the effect of the cavity is to decrease the radiation resistance and increase the reactive impedance of the dipole. The radiation impedance is changed from $65\Omega + j28\Omega$ over a ground plane, to around $50\Omega + j95\Omega$ when inserted in the pyramidal horn. This result is expected because the pyramidal cavity behind the monopole antenna has a cross-section smaller than 0.5λ . The waveguide modes are all cut-off, and the cavity presents a strong reactive effect on the dipole. The cavity can be modelled by a back-plane reflector that is much closer to the antenna than the horn apex of 0.4λ . Such a reflector decreases the radiation resistance and increases the reactive impedance of the antenna.

Similar measurements were done on a monopole antenna from 7.2 GHz to 7.4 GHz. As seen in Fig. 14, the effect of the cavity is to decrease the radiation resistance and increase the reactive impedance of the monopole. The radiation impedance is changed from $46\Omega + j15\Omega$ over a ground plane, to around $25\Omega + j40\Omega$ when inserted in the pyramidal horn. This is in strong agreement with the dipole antenna measurements.

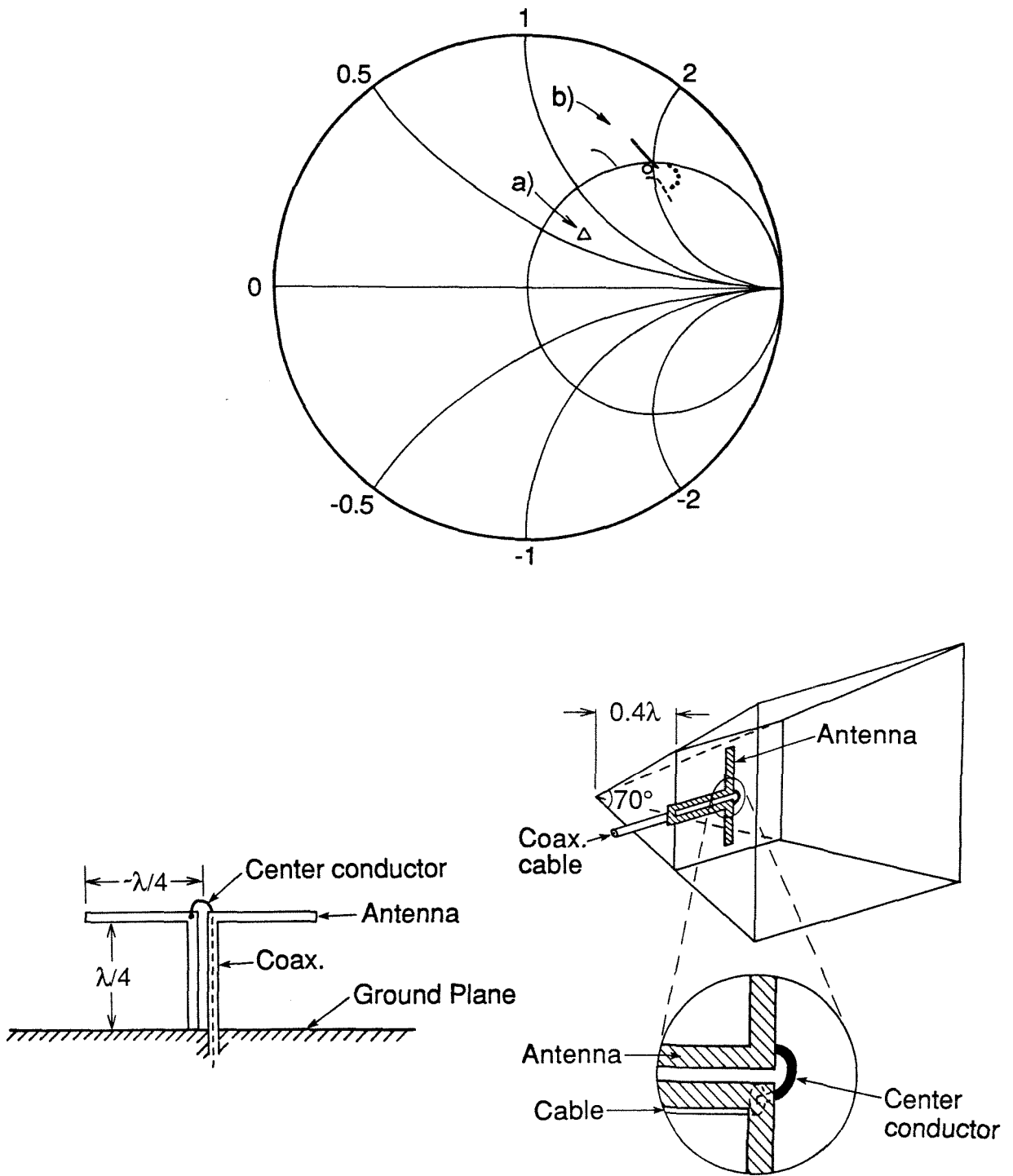


Figure 13. The microwave scale model impedance measurements on a quarter-wave dipole over a ground plane (a) and in a pyramidal cavity (b).

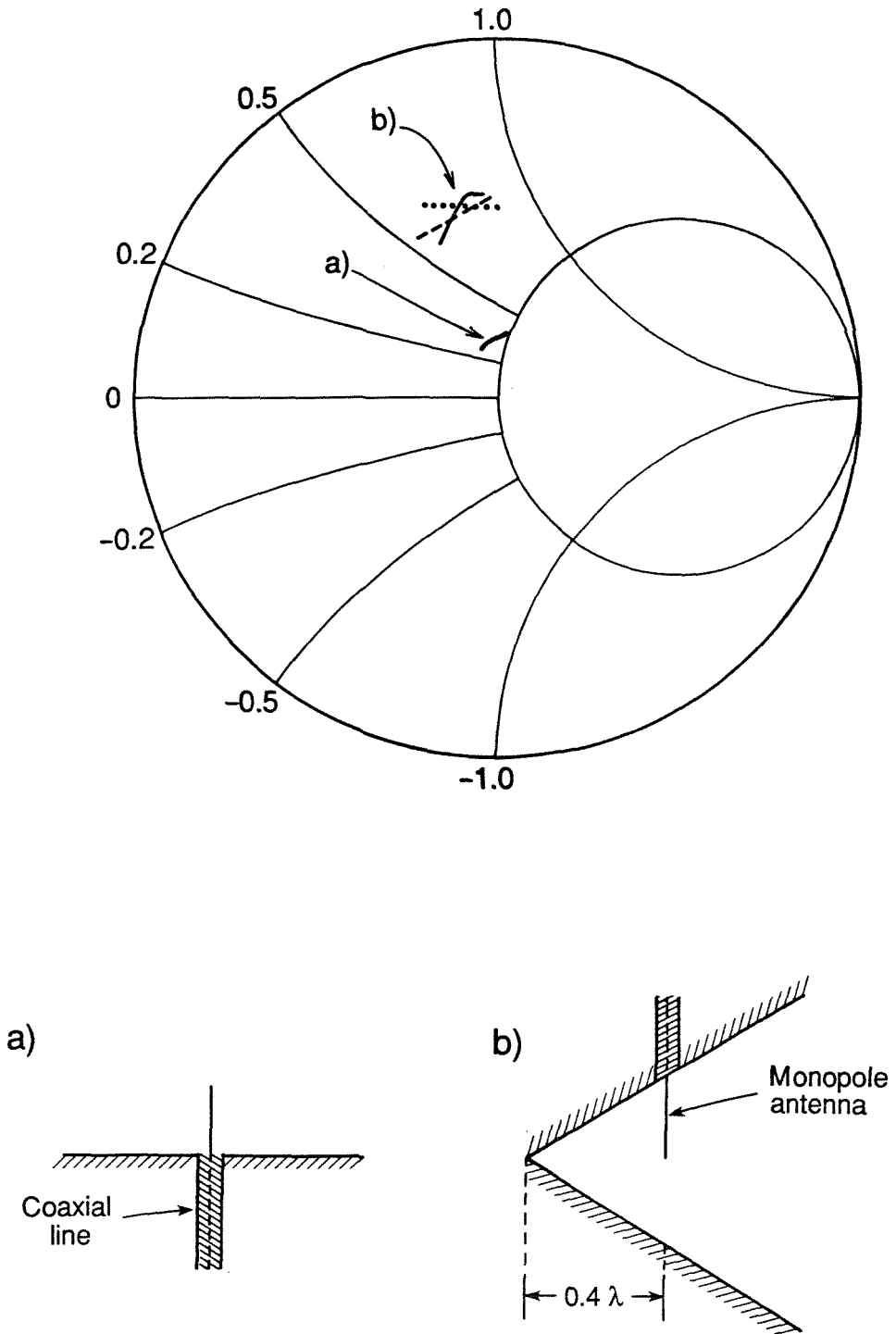


Figure 14. The microwave scale model impedance measurements on a monopole over a ground plane (a) and in a pyramidal cavity (b).

3.4 System Calibration at 93.2 GHz

Absolute power calibration can be readily made at 93 GHz using commercially available power meters [11]. In this case, 4 different power meters were compared at this frequency. The maximum deviation was $\pm 5\%$ from the average. The gain of the transmitting horn was accurately measured by the two-antenna measurement method [12]. In this method, two identical antennas are used for transmitting and receiving the power. The ratio of the received power to the transmitted power is given by

$$\frac{P_R}{P_T} = \left(\frac{\lambda}{4\pi R} \right)^2 G^2 \quad (3.3)$$

where R is the separation between the transmitting and receiving antennas, and G is the gain of the antenna. The transmitted and received power are measured using the same power meter. The measured gain of the antenna is thus independent of any miscalibrations, if any, in the power meter. The range was checked by measuring the received power versus distance (Fig. 14). The gain of the transmitting horn was $23 \text{ dB} \pm 0.1 \text{ dB}$ at 93.2 GHz. The measurements were done at a distance of $\frac{8D^2}{\lambda}$, which is much farther than the far-field criterion of $\frac{2D^2}{\lambda}$, D being the large cross-section of the transmitting horn.

The bolometer dc responsivity can be accurately measured by biasing the bolometer at increasing voltages and measuring the drop in resistance (Fig. 15). This measurement gives the responsivity of the bolometer in series with the resistance of the thin-film transmission line that connects the antenna to the bonding pad. The series resistance, R_s , is found by fabricating another array and measuring the input resistance with a shorted bolometer. The effect of this resistance is normalized out of the measurement, and the true dc responsivity of the bolometer is found (Fig. 16). The frequency response of the bolometer is found by measuring the received voltage from a 93 GHz plane wave modulated from 2 Hz to 2 KHz. The amplitude of the 93 GHz plane wave and the duty cycle of the modulation are

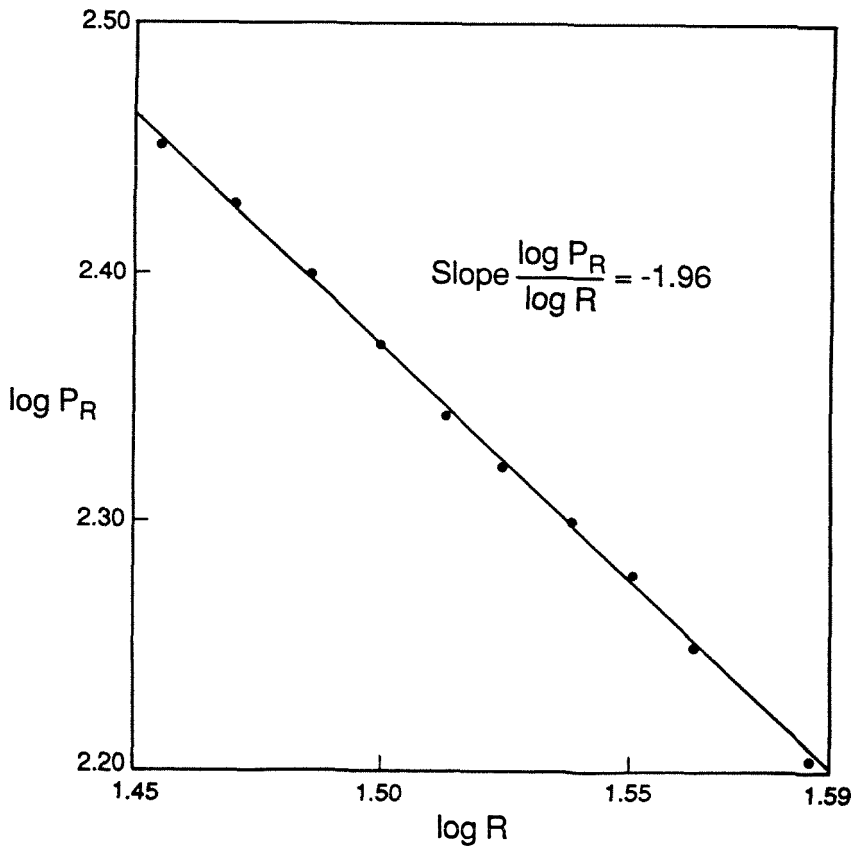


Figure 15. The received power vs distance in a two-antenna measurement setup.

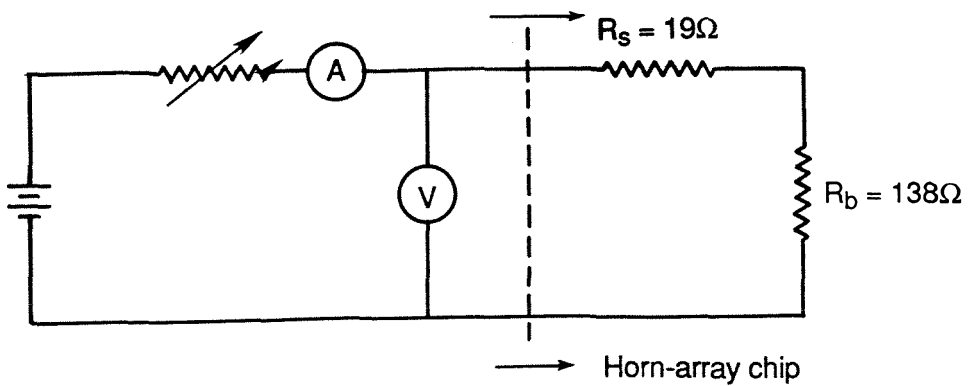


Figure 16. The method used for measuring the dc responsivity of the bolometer.

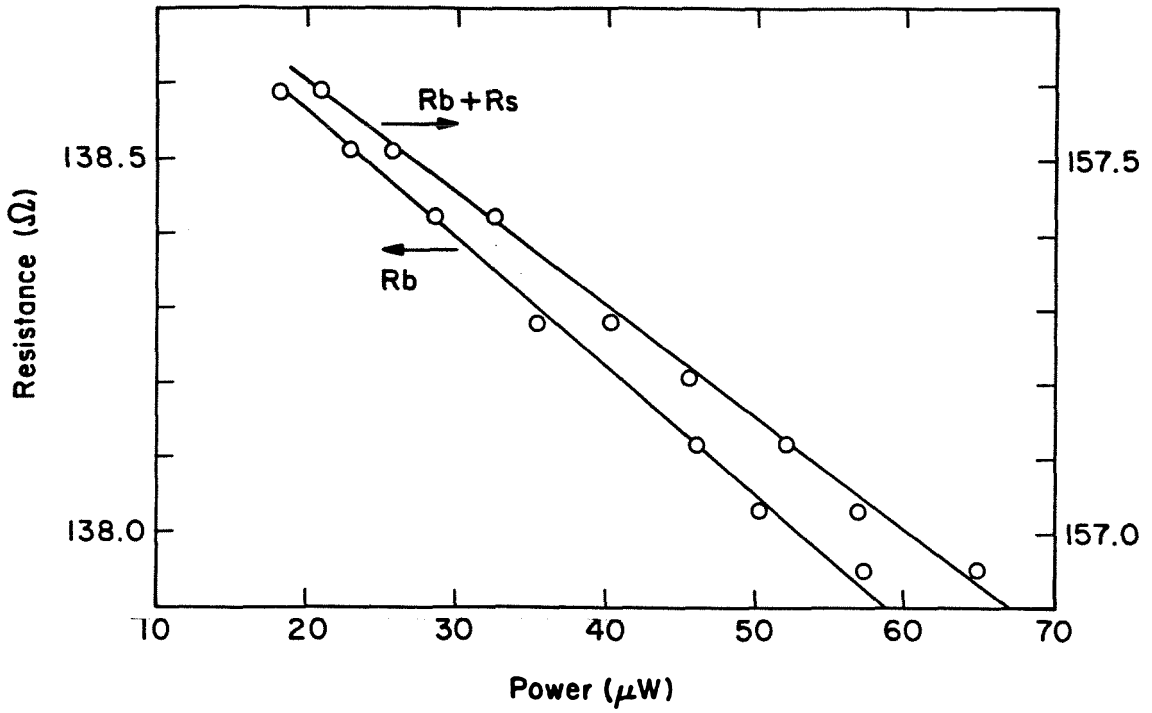


Figure 17. The measured dc responsivity of a bolometer.

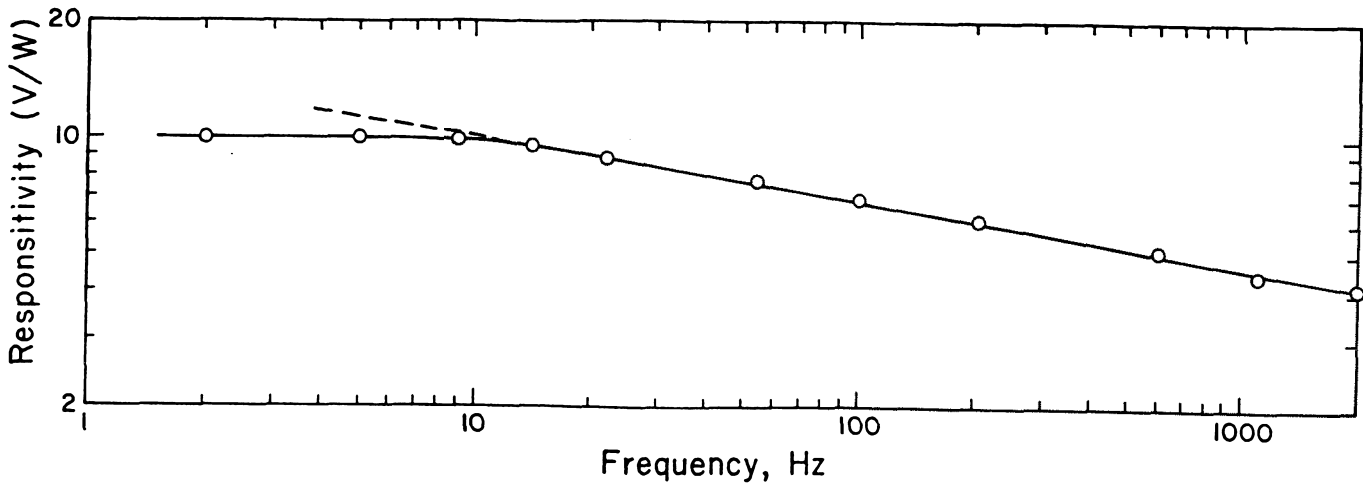


Figure 18. The measured frequency response of the bolometer.

kept constant. This measurement gives the relative response of the bolometer versus modulation frequency. The 2 Hz ac measurement is then normalized to the dc measurement, and the absolute bolometer responsivity at 1 KHz is found (Fig. 17). The system is now ready for absolute power measurements at 93 GHz.

3.5 Horn-Aperture Efficiency Measurements

The horn aperture efficiency of a single element in the array is defined as the power received by the bolometer divided by the total power incident on the horn aperture C_0^2 , when the array is illuminated by a plane wave of known power density. This definition includes the mismatch loss between the dipole antenna and the detector, and the resistive losses in the antenna and the coplanar-strip low-pass filter. It also includes the resistive losses in the horn sidewalls, the cross-polarization losses, and the loss due to coupling to the neighboring elements. Horn aperture efficiencies of $44 \pm 4\%$ were obtained. The theoretical horn-aperture efficiency was calculated from the co-polar two-dimensional scan to be 95%. This results in a total combined loss at 93 GHz of 3.35 dB.

3.5a Cross-Polarization Losses

The cross-polarized component was measured on several elements at 93 GHz. A peak component of -15 dB was found in the 45° and 30° planes. There was no measurable component in either the E or H-plane pattern. An upper limit on the cross-polarization losses is found by assuming that the cross-polarized 45° plane-pattern is rotationally symmetric, and calculating the power radiated from this pattern. The co-polar antenna directivity is then given by

$$D = \frac{4\pi}{\int_0^{2\pi} \int_0^{\frac{\pi}{2}} P_{co-p} \sin \theta \, d\theta \, d\phi + \int_0^{2\pi} \int_0^{\frac{\pi}{2}} P_{x-p} \sin \theta \, d\theta \, d\phi} \quad (3.4)$$

where P_{co-p} and P_{x-p} are the measured co-polar and cross-polar patterns. The effect of the cross-polarized pattern is to decrease the aperture efficiency from 95% to 91%. Therefore, the total cross-polarization losses are about 0.1–0.2 dB.

3.5b Horn-Sidewalls Resistive Losses

The 93 GHz horn array was assembled from four different stacked wafers (Fig. 18). The horn sidewalls of the back-shorting cavity and the front wafer are gold coated. The membrane-wafer is not, because it is hard (but not impossible) to evaporate gold on its sidewalls without covering the membrane with gold.

The sidewall losses are estimated by assuming that a TE_{10} wave is launched by the dipole on the membrane, and calculating the resistive losses using the TE_{10} current distribution on the sidewalls [13]. The effect of the high-order modes is neglected. The losses are assumed to be small, otherwise the TE_{10} waveguide mode representation is not valid. The sidewall losses P_{loss} are related to the total transmitted power P_{out} by

$$\frac{P_{loss}}{P_{out}} = \frac{\sqrt{2}R_s}{377} \int_{C_1}^{C_2} \frac{[1 + 2(\frac{\lambda}{2C_z})^2]}{\sqrt{2}C_z \sqrt{1 - (\frac{\lambda}{2C_z})^2}} dC_z \quad (3.5)$$

where C_z is the variable cross-section of the pyramidal cavity, and R_s is the millimeter-wave surface resistance of the sidewalls, given by

$$R_s = \sqrt{\frac{\pi f \mu}{\sigma}} \quad (3.6)$$

where μ and σ are the permittivity and conductivity the horn sidewalls, and f is the frequency. The integral in Equ. 3.4 is not valid for cross-sections smaller than 0.5λ . The losses of the gold coated sections are negligible because R_s is very small. The resistivity of the membrane-wafer was measured using a four-point probe [14]. The membrane-wafer has an $R_s = 46\Omega$ at 93 GHz and is located between $C_1 = 0.56\lambda$ and $C_2 = 0.7\lambda$. The total sidewall losses are then calculated to be around 0.7 dB.

3.5c Other Losses

A $2\text{--}4\mu\text{m}$ thick dielectric layer is sandwiched between two wafers every time they are assembled together. This layer presents a series resistance to the axially

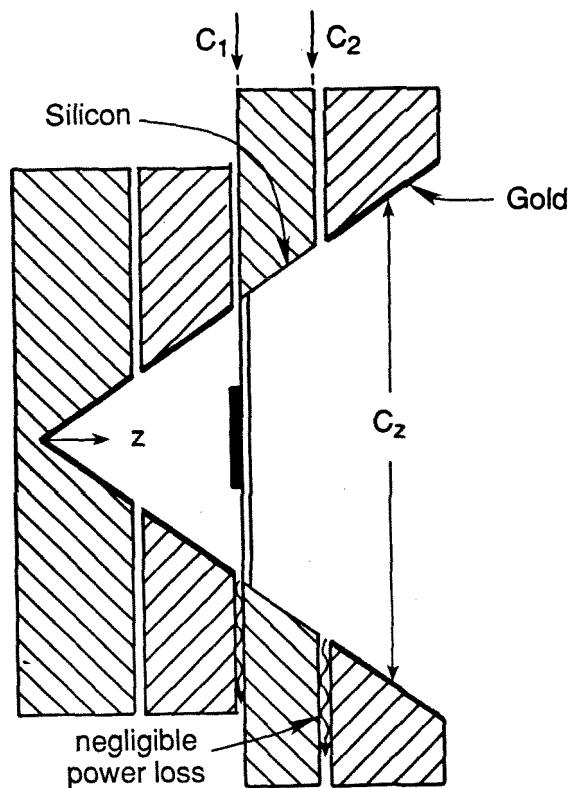


Figure 19. Detailed sketch of the 93 GHz imaging array.

Intrinsic Pattern Loss	-0.2 dB
Mismatch Loss	-2.2 dB
Horn Sidewalls Loss	-0.7 dB
Cross-Polarization Loss	(-0.2, -0.1) dB
Horn-to-Horn Coupling Loss	(-0.2, -0.1) dB
Total Losses	-3.4 dB

Figure 20. The accurate breakdown of the horn losses.

directed (\vec{z}) current arising from the TE₁₀ mode. The equivalent series resistance is about 0.5Ω [15] and the losses in this layer are truly negligible (Fig. 18). Also, the series resistance losses in the coplanar-strips low-pass filter is small, because it presents a very high impedance at the dipole apex. The coupling between two different horns was investigated at 7.2 GHz. Coupling values of -20 dB in the E-plane and -30 dB in the H-plane were measured at 7.2 GHz for a dipole feed. These figures are much lower than the estimated values given by Amitay [6]. The coupling losses are then estimated to be around 0.1–0.2 dB.

3.5d Antenna Losses

The receiving antenna on the membrane is a quarter-wave silver dipole with a full-length of $1560\mu m$, a width of $80\mu m$ and a thickness of 1000\AA . The RF series resistance is equal to the dc resistance since the dipole thickness is a third of a skin-depth at 93 GHz. The current distribution on the dipole is sinusoidal with the peak at the center and a null at the tips. This yields an effective length for series-resistance calculations equal to half of the dipole full-length. The series resistance is equal to 4Ω . The antenna is designed to have a resonant impedance of 60Ω in free-space. Microwave measurements at 7.3 GHz resulted in a dipole impedance around $50\Omega + j95\Omega$ (section 3.3).

The available power to a matched load from the dipole is given by $\frac{V_a^2}{4R_a}$, where V_a is the voltage across the dipole, and R_a is the radiation resistance. The power absorbed by the bolometer P_b divided by the available power P_{av} is given by

$$\frac{P_b}{P_{av}} = \frac{4R_a R_b}{(R_t^2 + X_a^2)} \quad (3.7)$$

where R_b is the bolometer resistance, R_t is the sum of the antenna resistance, the bolometer resistance and the series resistance in the circuit, and X_a is the dipole reactive impedance. The bolometer RF resistance is equal to its dc value of 138Ω . The total antenna losses are calculated to be 2.2 dB. The loss in the series resistance

of the antenna is negligible due to the the large antenna impedance, and the loss is then entirely due to the mismatch between the dipole and the bolometer. This brings the total calculated losses to 3.2 dB. There is no need to search for the last 0.1 dB, because our measurement error is about ± 0.4 dB.

Tabulated in Fig. 19 are the antenna losses discussed above. All the losses, except for the cross-polarization losses, are easily minimized. If the horn sidewalls are all gold coated, and the antenna is matched to a low impedance slightly capacitive detector, the aperture efficiency of a 1.0λ square horn will be greater than 88%.

3.6 Coupling Efficiency Measurements

The coupling efficiency to an imaging system is defined as the power received by a *single* element placed at the focal point of an imaging system, divided by the total power incident on the lens, when the lens is illuminated by a plane wave of known power density (Fig. 20). The theoretical coupling efficiency [16] of a horn array of square aperture size of 1.5λ are presented in Fig. 21. This figure also shows the spillover and taper loss. The coupling efficiency peaks around 60% for an f-number around 0.85. A 1.5λ imaging array was constructed at 242 GHz. However, a comparison with the theoretical results is not possible at this frequency, because absolute power measurements cannot be made accurately.

The coupling efficiency of the 1.0λ imaging array was measured at 93 GHz for systems of different f-numbers (Fig. 23). About 24% of the incident power is absorbed by a single detector for an f-number of 0.7, and 14% for an f-number of 1.1. This translates to a coupling efficiency around 54% for an $f\backslash 0.7$ system, with a matched antenna and low-resistive losses. This is in strong agreement with the peak theoretical coupling-efficiency of 60% attainable with similar feed patterns.

The distribution of power in the focal plane for an incident plane-wave normal to the lens, is measured for two separate lenses with f-numbers of 1.1 and 0.7,

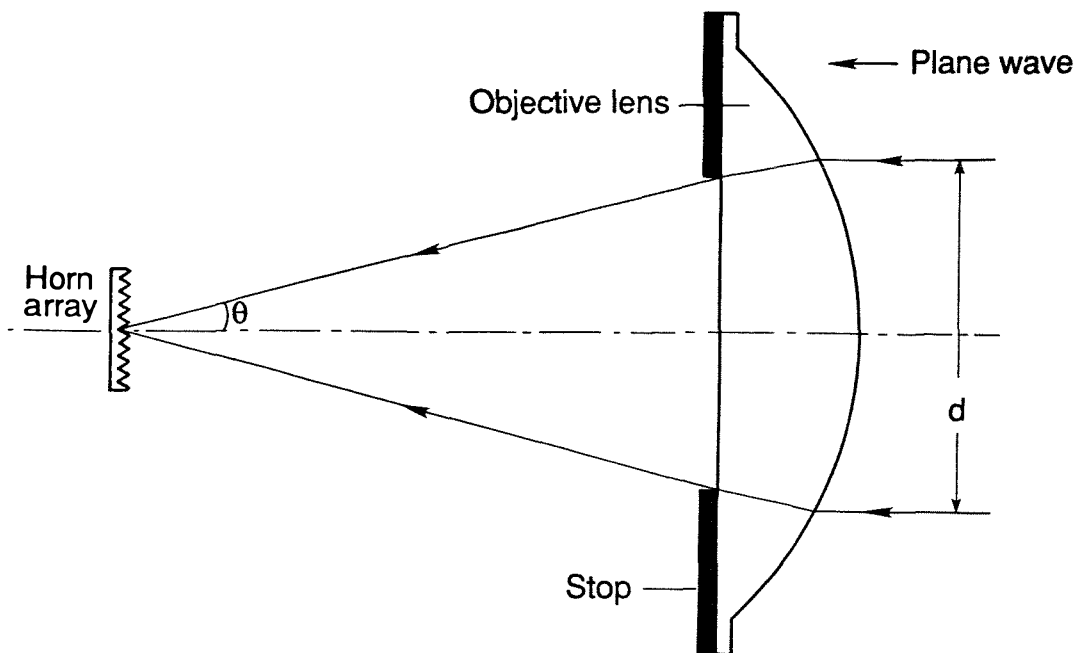


Figure 21. The coupling efficiency measurement system. Various lens-stops yield different f-number systems.

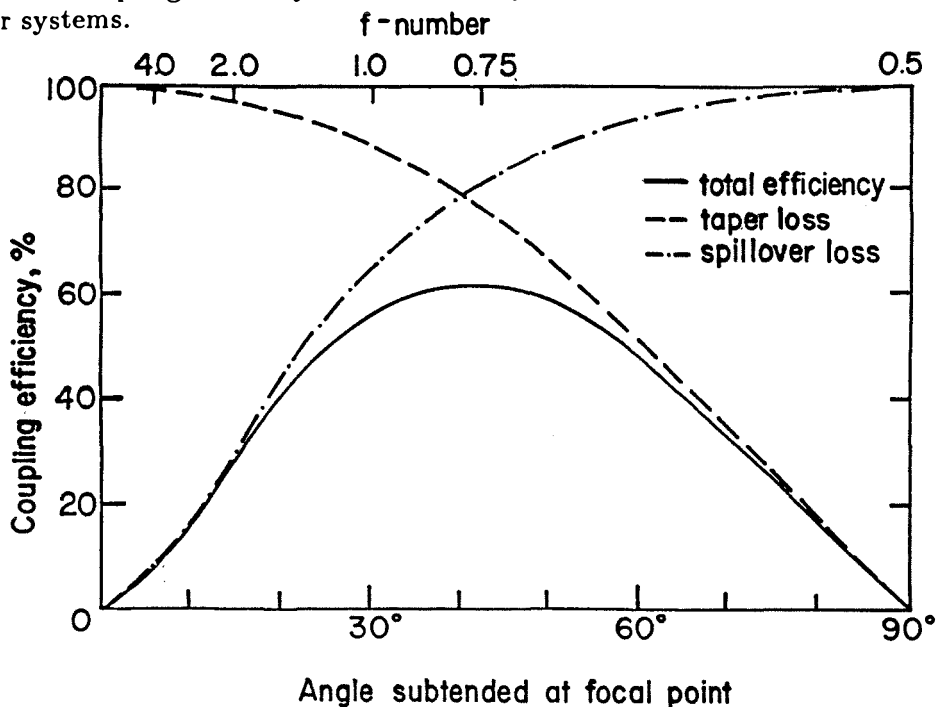


Figure 22. The theoretical coupling efficiency of a horn element in a 1.5λ imaging array.

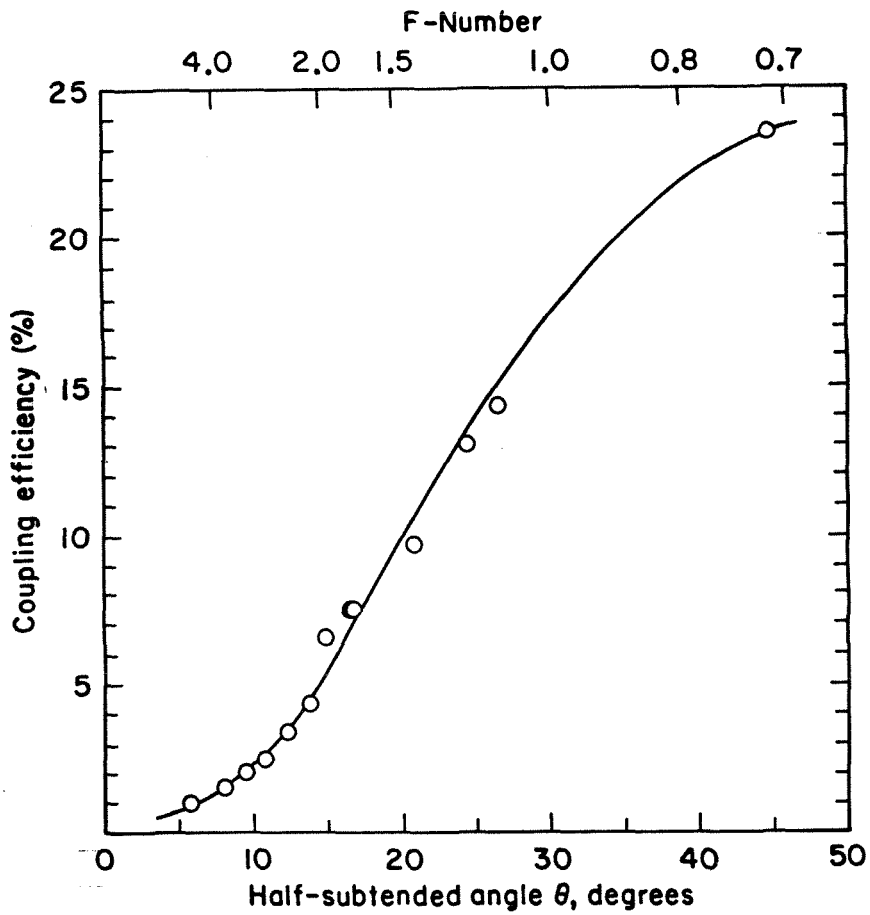


Figure 23. The coupling efficiency of a horn element in a 1.0λ imaging array. The measured points, indicated by circles, include the mismatch and resistive losses in the horn element, and the taper and spillover losses of the lens.

respectively (Fig. 23, 24). The sum of the total power on the focal plane yields a total coupling efficiency of 25% in both cases. The lens Airy pattern [17] has a first dark-ring radius of 0.61λ and 1.22λ for an $f\backslash 0.7$ and $f\backslash 1.1$ lens, respectively. The center element receives 96% of the total power incident on the focal plane for an $f\backslash 0.7$ lens, and 56% for an $f\backslash 1.1$ lens. There is then a strong optical coupling between the elements for an $f\backslash 1.1$ lens, i.e: for a diffraction limited imaging array. In Prof. Thomas Phillips words: "Hence, a significant fraction of the power received from the area in the sky appropriate to the central element is distributed among adjacent elements, and this central element also receives power from the areas of the sky appropriate to its neighbors" [18]. This optical coupling will blur the image, although in principle, the information is recoverable by coherent processing. On the other hand, if an $f\backslash 0.8$ to $f\backslash 0.7$ system is chosen, the coupling efficiency to the central element will increase to around 50%, and the optical coupling between the central element and its neighbors will decrease sharply. The penalty paid is an undersampling of the image.

In conclusion, the system design is a compromise between a diffraction limited image with medium coupling efficiency and large optical coupling, or an undersampled image with a high coupling efficiency and small optical coupling.

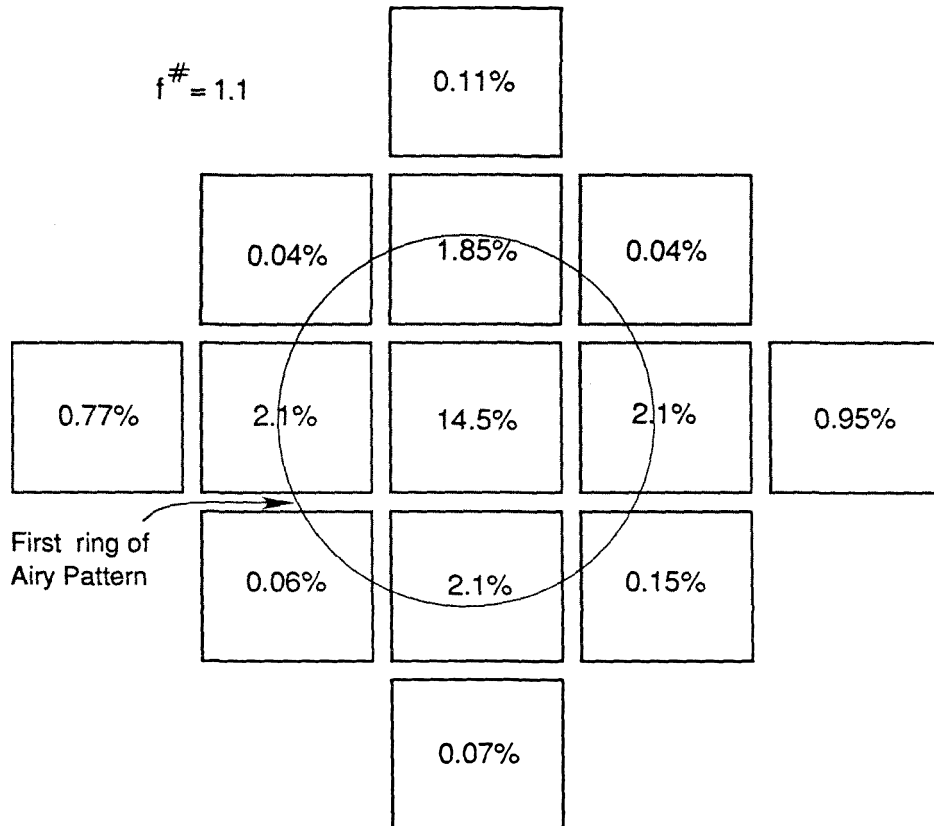


Figure 24. The distribution of power in the focal plane for an $f/1.1$ lens.

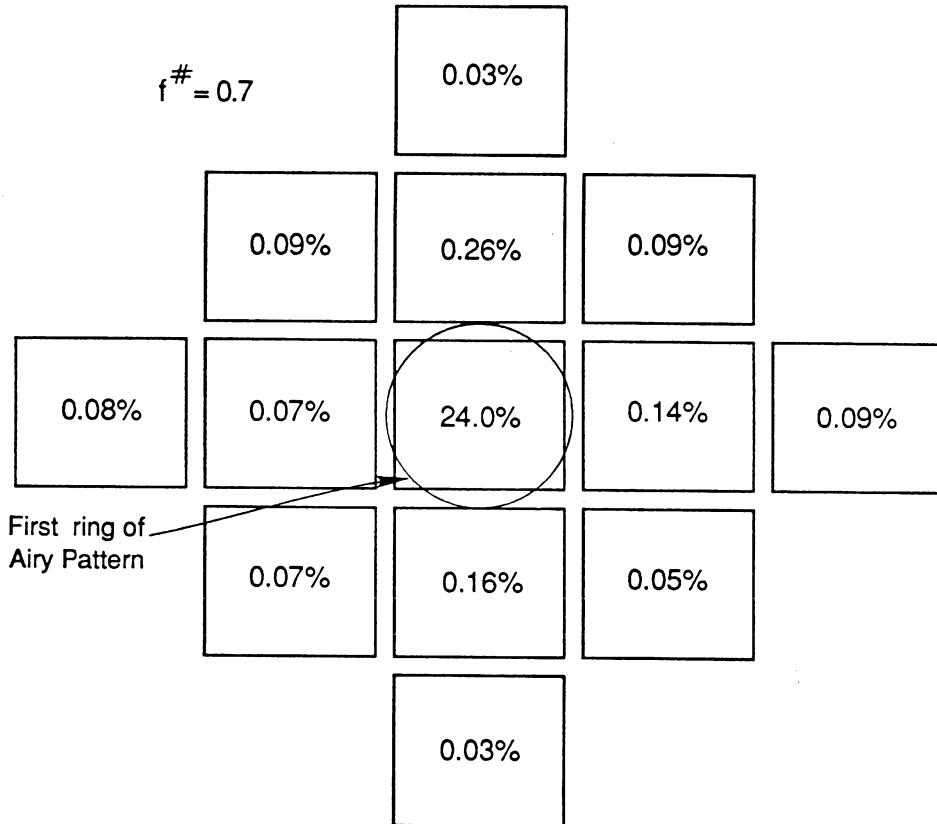


Figure 25. The distribution of power in the focal plane for an $f/0.7$ lens.

References

- [1] D. P. Neikirk, W. W. Lam and D. B. Rutledge, "Far-infrared microbolometer detectors," *Int. J. of Infrared and Millimeter Waves* **5**, pp. 245–278, 1984.
- [2] R. S. Elliott, "Antenna Theory and Design", Chap. 1, Prentice-Hall, Englewood Cliffs, 1981.
- [3] C. A. Balanis, "Antenna Theory and Design," Chap. 11, Harper and Row, New York, 1984.
- [4] G. Smolinsky, R. P. Chang and T. M. Mayer, "Plasma etching of III-V compound semiconductor materials and their oxides", *J. Vac. Sci. technol.*, vol. 18, pp. 12–16, Jan.–Feb. 1981.
- [5] D. W. Shaw, "Localized GaAs etching with acidic hydrogen peroxide solutions", *J. electrochem. Soc.: Solid-State Science and Technology*, vol. 128, pp. 874–880, April 1981.
- [6] N. Amitay, V. Galindo, and C. P. Wu, "Theory and Analysis of Phased Array Antennas", pp. 37–44, Wiley-Interscience, New York, 1972.
- [7] R. J. Mailloux, "Phased array theory and technology", *Proc. IEEE*, vol. 70, pp. 246–291, March 1982.
- [8] M. Upton, P. M. Smith and P. C. Chao, "HEMT low-noise amplifier for Ka-band," *Int. Symp. IEEE Microwave Theory Techniques*, pp. 1007–1010, June 1987.
- [9] W. L. Williams, R. C. Compton and D. B. Rutledge, "Elf: Computer automation and error correction for a microwave network analyser," *IEEE Trans. Instrum. Measurements*, vol.
- [10] O. M. Woodward, Jr., "Balance measurements on Balun transformers," *Electronics*, vol. 26, pp. 188–191, Sept. 1953.

- [11] Anritsu Corporation, 15 Thornton Rd., Oakland NJ 07436.
- [12] W. Kummer and E. S. Gillespie, "Antenna Measurements-1978", *Proc. IEEE*, vol. 66, pp. 483-511, April 1978.
- [13] R. F. Harrington, "Time-Harmonic Electromagnetic Fields," McGraw-Hill, New York, 1961.
- [14] D. R. Zruscky, H. D. Bush and J. R. Fassett, "Sheet resistivity techniques," *Rev. Sci. Inst.*, vol. 42, p. 283, April 1965.
- [15] S. Ramo, J. R. Whinnery and T. Van Duzer, "Fields and Waves in Communication Electronics," Chap. 7, John Wiley & Sons, New York, 1965.
- [16] C. E. Zah, R. C. Compton and D. B. Rutledge, "Efficiencies of elementary integrated circuit antennas," *Electromagnetics*, vol. 3, pp. 239-254, 1984.
- [17] E. Hecht and A. Zajac, "Optics," Chap. 10, Addison-Wesley Publishing Co., Reading, Massachusetts, 1979.
- [18] A. R. Gillespie and T. G. Phillips, "Array detectors for millimeter line astronomy," *Astronomy and Astrophysics*, vol. 73, pp. 14-18, 1979.

Chapter 4

Log-Periodic Antennas on Thin Membranes

Submillimeter-wave antennas have been fabricated on $1\text{-}\mu\text{m}$ thick silicon-nitride membranes. This approach results in better patterns than previous lens-coupled integrated circuit antennas, and eliminates the dielectric loss associated with the substrate lens. Measurements on a wideband log-periodic antenna 700 GHz, 370 GHz and 167 GHz, show no sidelobes and a 3-dB beamwidth between 40° and 60° . A linear imaging array shows similar patterns at 700 GHz. The patterns are bidirectional, so a back plane reflector is used to make the patterns unidirectional. At 370 GHz, the effective receiving aperture is increased by 5.5 dB at a mirror position of 0.7λ . Possible applications for membrane antennas include wideband superconducting tunnel-junction receivers for radio astronomy, and imaging arrays for radiometry and plasma diagnostics.

4.1 Introduction

At millimeter and submillimeter wavelengths, integrated-circuit antennas are often mounted on a substrate lens to eliminate losses due to substrate modes [1,2]. This approach takes advantage of the fact that antennas on dielectrics are more sensitive to radiation from the substrate. However, coupling efficiencies for these antennas have been limited to about 25% because of poor patterns and dielectric losses. Substrate-lens coupled log-periodic and spiral antennas [3] have much better radiation patterns than bow-tie antennas, and are therefore expected to have a higher coupling efficiency. However, the dielectric losses become particularly severe at submillimeter wavelengths [4]. We have solved the dielectric loss problem, and improved the patterns by fabricating the antennas on $1\text{-}\mu\text{m}$ thick dielectric membranes (Fig. 1). The membrane is much thinner than a wavelength, so that the antenna effectively radiates in free space. This approach eliminates the substrate

lens and thus greatly reduces the dielectric losses, and allows the use of free-space antenna designs and techniques. One could design a high gain series-fed dipole array by using simple free-space design equations. In our application, we have integrated a wideband self-complementary log-periodic antenna on the membrane. The antenna patterns are bidirectional with the peak of the pattern normal to the wafer. The antenna impedance is constant over all frequencies, and is equal to 189Ω in free space [5]. A back-plane reflector is needed to make the patterns unidirectional, and thus increase the effective receiving aperture of the antenna.

4.2 Fabrication

A $1\text{-}\mu\text{m}$ silicon-oxynitride layer is deposited on both sides of a $\langle 100 \rangle$ silicon wafer using plasma-enhanced chemical vapor deposition. The layer must be in tension to yield flat and rigid self-supporting membranes. The deposition parameters and the tension measurements of the silicon-oxynitride layer, are explained in Chapter 2. The membranes are fabricated in two steps. First, an opening is defined on the back of the wafer by patterning the silicon oxynitride with photoresist and etching it in a buffered-HF solution. Then the silicon is etched in an ethylenediamine-pyrocatechol solution [6] until the transparent membrane is exposed. The etching process is anisotropic and forms pyramidal cavities bounded by $\langle 111 \rangle$ crystal planes. These side walls form an angle of 54.7° with the $\langle 100 \rangle$ wafer plane. Next the antennas and detectors are lithographically defined on the membrane. The membranes are mechanically strong and can withstand all standard fabrication steps. The detectors are bismuth microbolometers with a dc resistance of 150Ω and a dc responsivity of 10 V/W at a bias of 0.1 V .

The mirror is made in a similar way. An oxide layer is thermally grown on both sides of a $\langle 100 \rangle$ silicon wafer. The oxide is stripped off one side except for square patches which are slightly larger than the membrane. Then the silicon wafer is etched down to the desired depth, and this determines the distance between

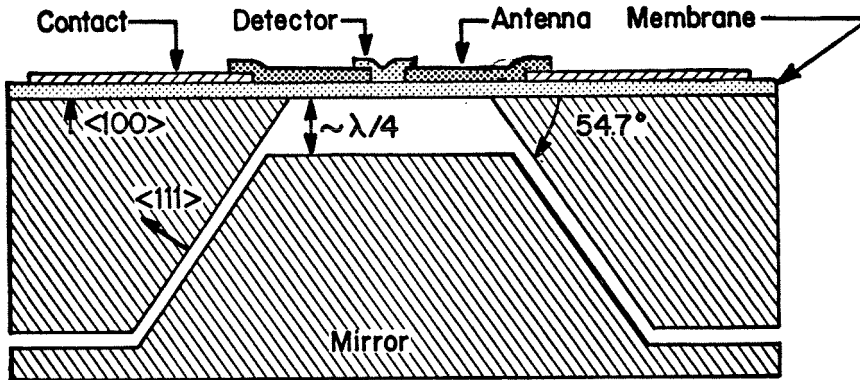


Figure 1. Antenna on a thin membrane with a back-plane reflector.

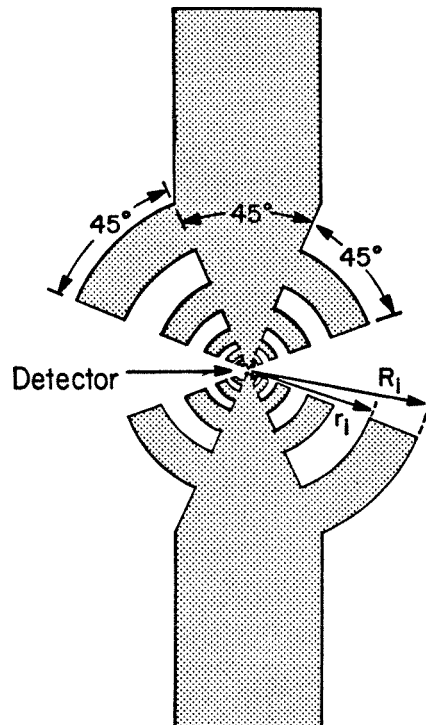


Figure 2. Self-complementary log-periodic antenna.

the antenna on the membrane and the mirror. The corners of the square are not protected from the anisotropic etch, and considerable etching occurs around the corners. This results in a roughly circular mirror. Finally, a layer of gold is evaporated on the mirror structure. The mirror is inserted in the cavity and aligned parallel to the membrane with a He-Ne laser.

Another fabrication process follows a similar approach. The antenna, detector and contacts are first defined on a silicon-oxynitride layer deposited in tension, on the top side of a silicon wafer. Then they are covered by a $1\text{-}2\mu\text{m}$ layer of silicon nitride or silicon dioxide deposited at low temperatures by plasma enhanced chemical vapor deposition. This layer protects the metalization from the anisotropic etchant. An infrared mask aligner is then needed to define an opening on the back side of the wafer, which is aligned to the antenna. The wafer is then etched in an ethylene-diamine-pyrocatechol solution, until the transparent membrane appears. This fabrication process has the advantage that no lithography, aligning or evaporation is done on thin membranes, and therefore will have higher yields. The radiation properties of the antenna should not be affected if it is sandwiched between two $1\text{-}\mu\text{m}$ thick dielectric layers.

4.3 Wideband Log-Periodic Antenna

The antenna follows the classical log-periodic design of DuHamel and Isbell [7]. The n^{th} tooth is characterized by an inner radius r_n and an outer radius R_n where $R_n/r_n = \sigma = \sqrt{2}$ and $R_{n+1}/R_n = \tau = 2$ (Fig. 2). The antenna is a self-complementary design with an impedance of 189Ω over the frequency range from 100 to 1400 GHz, and is linearly polarized along the resonant tooth. The high-frequency cutoff is determined by the smallest tooth, and the low-frequency response is limited by the size of the membrane. In our case, the membrane was 1.85 mm, resulting in a low-frequency cutoff of 115 GHz. The mirror used in the 370 GHz measurements has a diameter of 1.7 mm (Fig. 3).

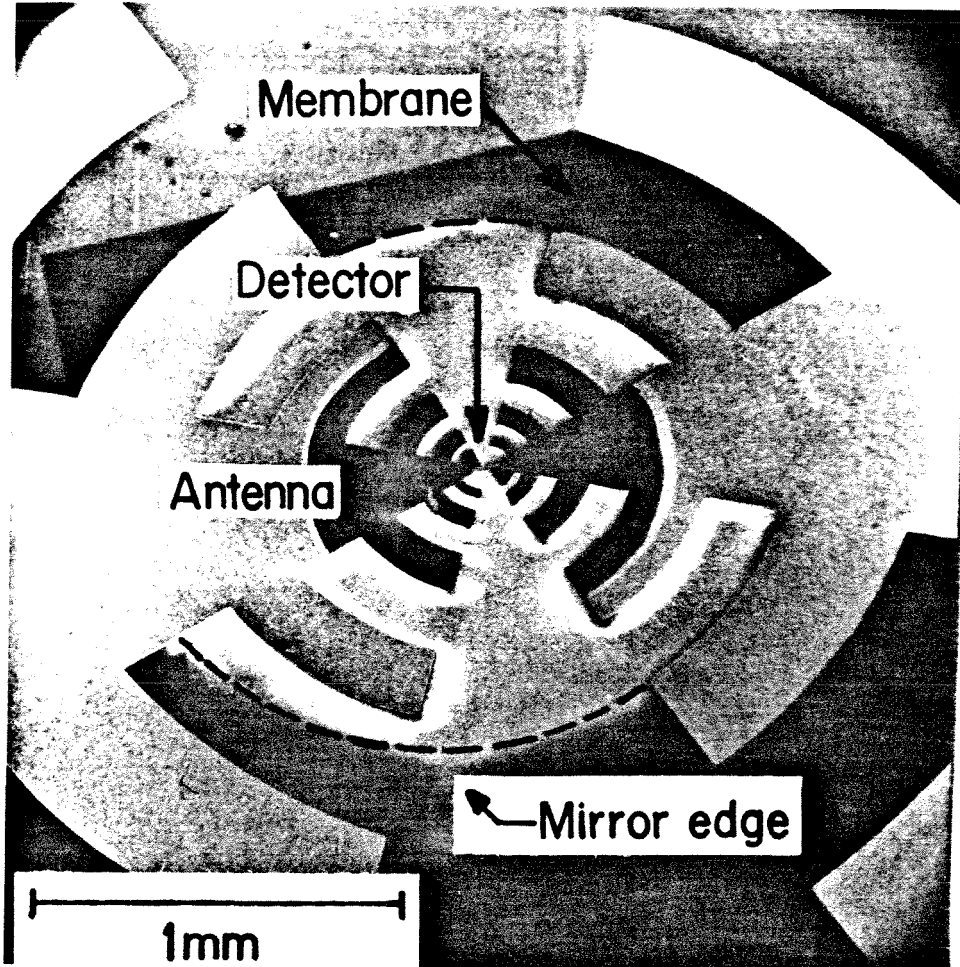


Figure 3. Scanning electron micrograph of a log-periodic membrane antenna with a back-shorting mirror in the cavity.

4.3a Pattern Measurements

The patterns were measured at 700 GHz, 370 GHz and 167 GHz (Fig. 3). The sources were a CO₂ pumped far-infrared laser at 700 GHz, a Thompson-CSF BWO at 370 GHz, and a Micronow BWO sweeper at 167 GHz. The power was monitored by corner cubes with schottky diodes [8] at 700 GHz and 370 GHz (Fig. 8), and by an Anritsu waveguide power-sensor [9] at 167 GHz. The E and H-plane measurements follow the same procedure outlined in Chap. 3.

The antenna was placed on rotation and translation stages, and for the 700 GHz and 370 GHz measurements, scans were made in the plane of the antenna to insure a gaussian mode distribution of the incident power. The antenna was placed at the peak of the gaussian mode. The antenna is linearly polarized along the resonant tooth, and the on-axis cross-polarization ratio was greater than 20 dB at all frequencies. The pattern measurements were taken from the top side of the wafer. The back-side patterns were similar to the front-side ones, but with additional shoulders from reflections off the <111> facets. The E and H plane patterns are very similar (Fig. 4, 5). Table 4.1 shows the average 3-dB and 10-dB beamwidths measured at 167 GHz, 370 GHz and 700 GHz. The directivity of the antenna at 370 GHz is 7.85 dB. Duhamel and Isbell [7] reported an average 3-dB beamwidth of 55° from their measurements around 1 GHz. The effect of the membrane is therefore negligible, and the antenna is easily scalable to higher frequencies. The structure in the 167-GHz pattern is probably due to the interaction of the resonant tooth lying near the edge of the membrane with the neighboring silicon. The ripples in the 370 GHz pattern are due to scattering from the antenna mount.

4.3b Mirror Measurements

A back-plane reflector makes the patterns unidirectional, and therefore increases the effective receiving aperture. The received power versus mirror position for normal incidence is calculated as follows. First, a gaussian pattern is fitted to

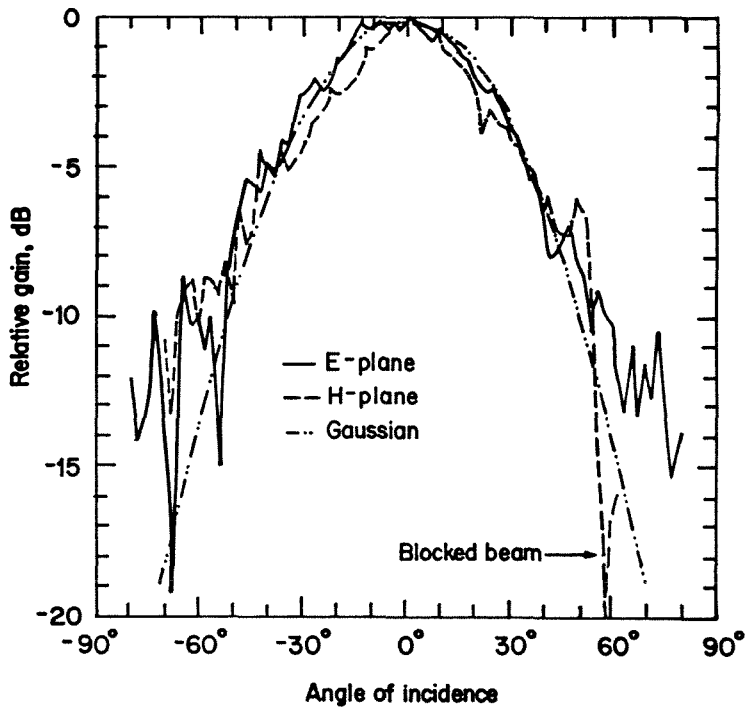
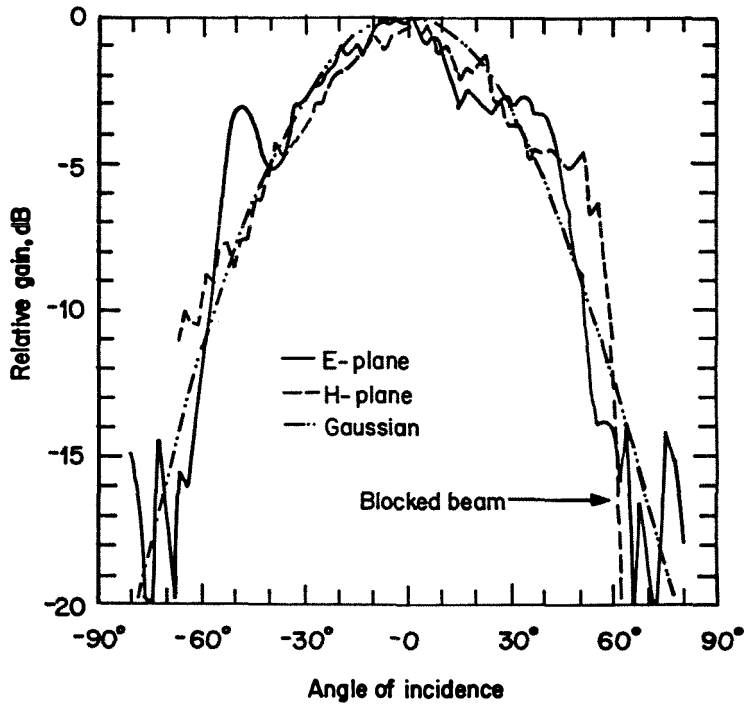
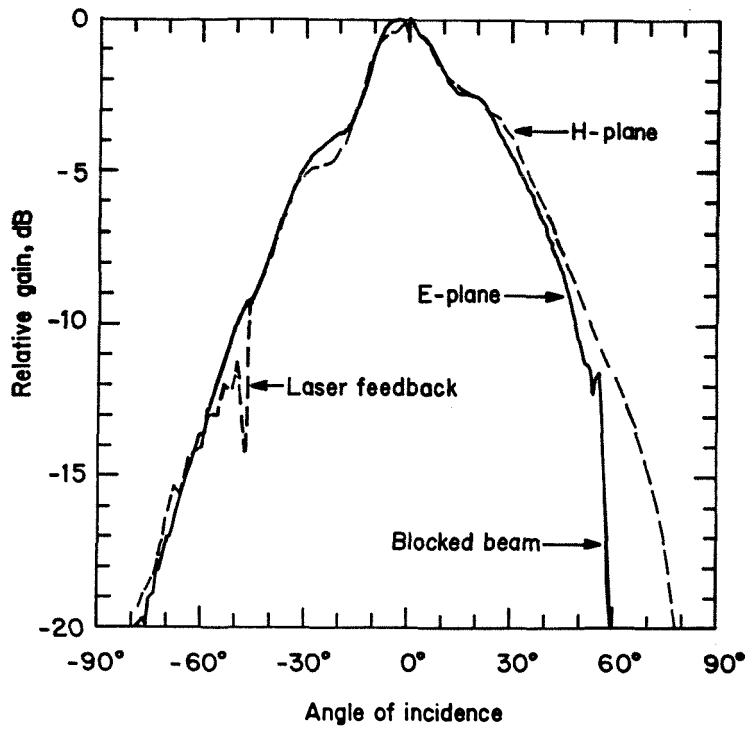


Figure 5. Measured E and H-plane patterns at 167 GHz (top) and 370 GHz (bottom).



	E-H(3-dB)	E-H(10-dB)
700 GHz	40°	98°
370 GHz	55°	103°
167 GHz	60°	110°

Figure 4. Measured E and H-plane patterns at 700 GHz (top), and the tabulated values of the 3-dB and 10-dB beamwidths of the log-periodic antenna (bottom).

the measured pattern at 370 GHz. This is done according to the coordinate system shown in Fig. 6. Since the E and H-plane patterns are similar, the fitted gaussian is rotationally symmetric and equal to $e^{(-\theta^2/0.35)}$, where θ is in radians. The pattern of the antenna with a back-plane reflector is given by

$$G_f(\theta) = 4 C e^{(-\theta^2/0.35)} \sin^2(kh \cos \theta) \quad (4.1)$$

where $k = \frac{2\pi}{\lambda}$, h is the distance between the antenna and the reflector, C is a normalizing constant, and $4 \sin^2(kh \cos \theta)$ is the array factor resulting from the antenna and its image [5, pp. 65–68]. The gain at normal incidence is

$$G_M(\theta = 0) = \frac{2 \sin^2(kh)}{\int_0^{\frac{\pi}{2}} e^{(-\theta^2/0.35)} \sin^2(kh \cos \theta) \sin \theta d\theta} \quad (4.2)$$

The received power P_R at normal incidence is proportional to the gain of the antenna, and is given by

$$P_R = \frac{\lambda^2}{4\pi} G_M(\theta = 0) (1 - \rho_M^2) P_I \quad (4.3)$$

where P_I is the incident power density, and $\rho = \frac{R_M - R_B}{R_M + R_B}$ is the mismatch between the radiation resistance of the antenna with a back-plane reflector and the bolometer impedance of 150Ω . The new radiation resistance is calculated assuming that the currents on the antenna are not affected by the mirror. This is true if we neglect the mutual coupling between the antenna and its image. The radiation resistance (Fig. 10) is then proportional to the total radiated power, calculated by integrating Equ. (4.1) over half-space.

Fig. 8 shows the effect of the mirror on the received power. If the mismatch factor was not taken into account, the predicted response becomes nearly flat from 0.05λ to 0.30λ . The fact that the measured response drops in this region, indicates two important things. First the bolometer submillimeter-wave impedance is equal

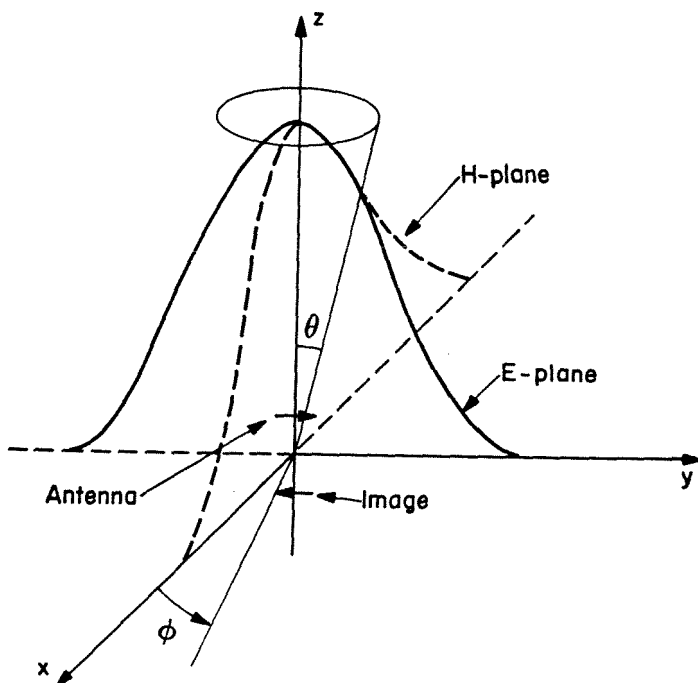


Figure 6. Coordinate axis for pattern calculations.

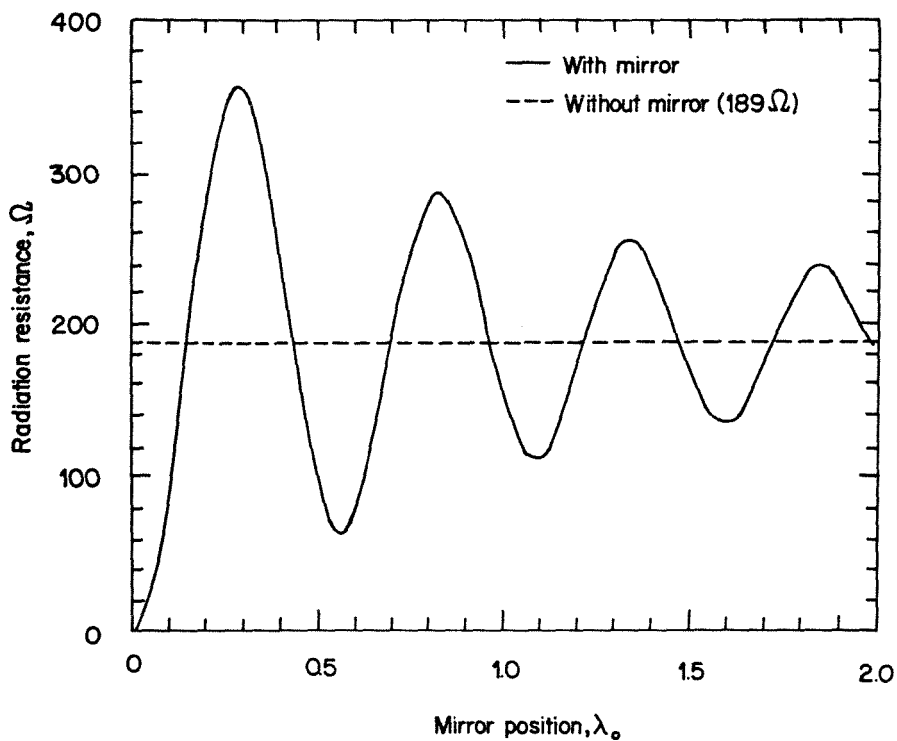


Figure 7. Calculated radiation resistance of a log-periodic antenna with a back-plane reflector.

to its dc value. This is because the bolometer is still much smaller than a wavelength at 370 GHz. Second, the submillimeter-wave antenna impedance is equal to the predicted radiation resistance (Fig. 7), calculated neglecting the membrane and the neighboring silicon wafer. This implies that free-space antenna techniques are applicable for submillimeter-wave antennas integrated on thin membranes.

The high gain measured around 0.75λ results from an interaction between the element pattern and the array pattern. At this spacing, the array pattern has a narrow main lobe, with a grating-lobe cone centered at 70° . However, the element pattern is 17 dB down at this angle. The result is a high-gain pattern with a narrow main lobe and -17 dB sidelobes. The measured received power increases by 5.5 dB at 0.7λ . The gain of the log-periodic antenna with a back-plane reflector is 13.35 dB. This amounts to an effective receiving aperture of $1.7\lambda^2$. For comparison, the effective aperture of a quarter-wave dipole backed by a ground plane is $0.5\lambda^2$, and is $1.7\lambda^2$ for a monolithic horn etched in silicon with a square opening of 1.6λ (ref. Chap. 3). The log-periodic antenna is therefore an efficient focal-plane antenna suitable for single-element imaging.

4.3c Coupling Efficiency

The coupling efficiency of a paraboloid of subtended half-angle θ_0 resulting from a rotationally symmetric feed pattern $G_f(\theta)$, is given by [10]

$$\epsilon = \cot^2(\theta_0) \left| \int_0^{\theta_0} \sqrt{G_f(\theta')} \tan\left(\frac{\theta'}{2}\right) d\theta' \right|^2 \quad (4.4)$$

where $G_f(\theta)$ is the pattern of a log-periodic antenna with a back-plane reflector given by (2.1). For a given feed pattern, the coupling efficiency is only dependent on the subtended half-angle θ the reflector, not on its size. The ratio $F = f/D$ of a paraboloid is related to θ by Eq. (2.4). Fig. 9 shows the calculated coupling efficiencies for different mirror positions. A value of 88% is possible for paraboloids

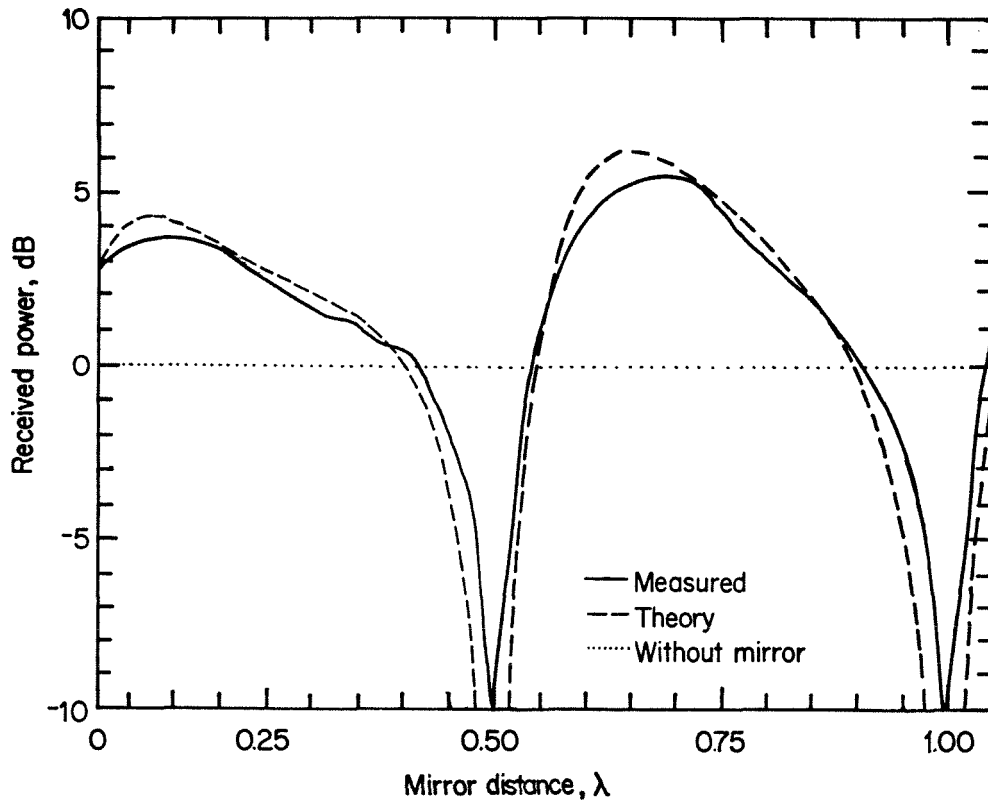


Figure 8. Measured received power for normal incidence at 370 GHz vs. mirror position.

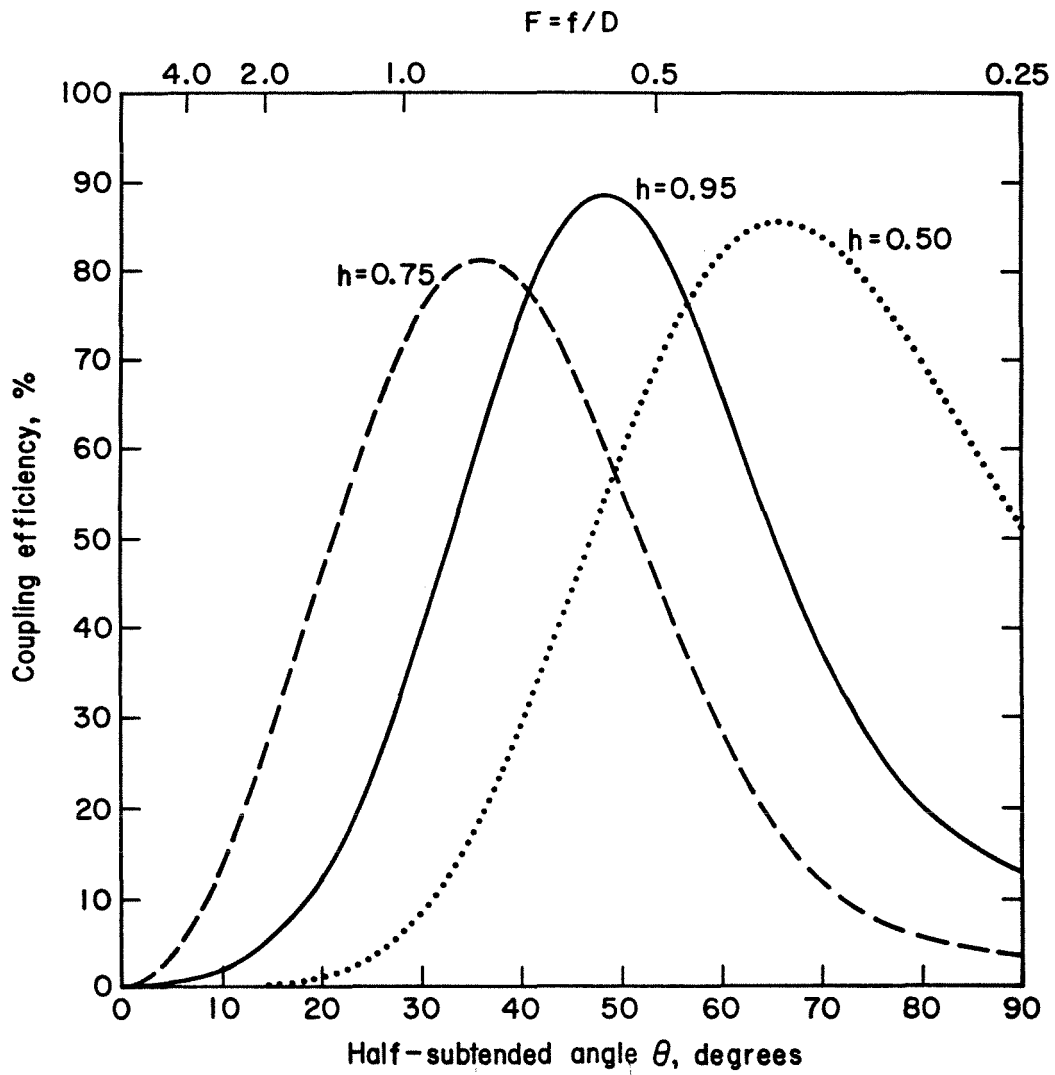


Figure 9. Calculated coupling efficiencies for different mirror positions.

with f/D equal to 0.6, and higher than 70% for f/D around 1. Measured coupling efficiencies should be lower due to cross-polarization, mismatch and ohmic losses.

4.4 Linear Imaging Array

A linear array of antennas was built and tested at 700 GHz (Fig. 10). The spacing between the antennas was 0.9λ . These antennas were shaped like bow-tie antennas with a pair of $\lambda/4$ teeth and a pair of $\lambda/4$ slots. The idea is to make an antenna with a pattern and impedance at a single frequency that are similar to the complementary log-periodic antennas. The measured cross-polarization ratio is 13 dB, and the polarization axis is shifted clockwise 20° from the tooth toward the array axis. Since the polarization does not match the array axis, the E field was rotated by a half-wave plate to yield the maximum signal from the detector, and the horizontal-plane (array-axis) and vertical-plane (bow-axis) patterns were measured (Fig. 11). The patterns were measured on several central elements from the top side of the wafer. The patterns are similar to the 700 GHz log-periodic patterns, except that the bow-axis beamwidth (50°) is wider than the array-axis beamwidth (40°). The 10-dB beamwidths are similar and equal to 120° . A back-plane reflector should sharpen the patterns, but no measurements with a back-plane reflector were done at this frequency.

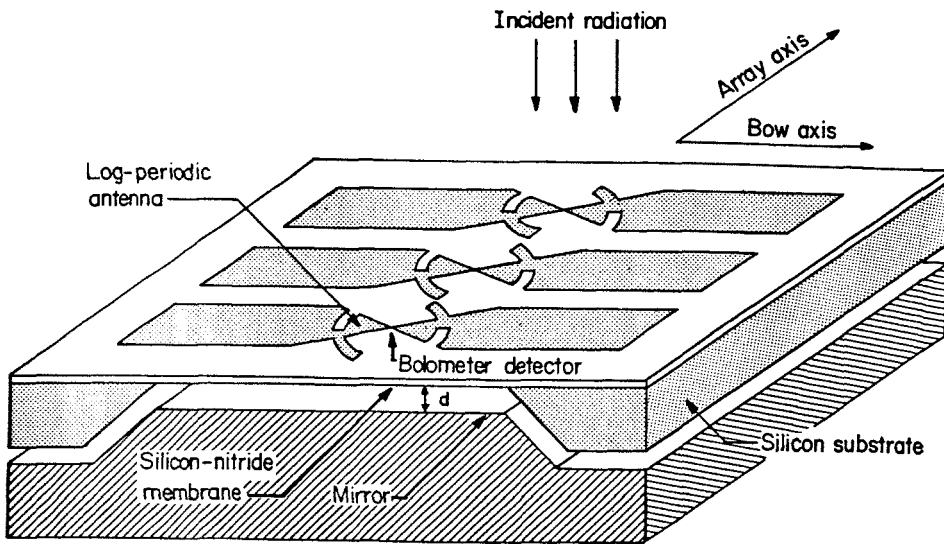


Figure 10. Linear imaging array for 700 GHz.

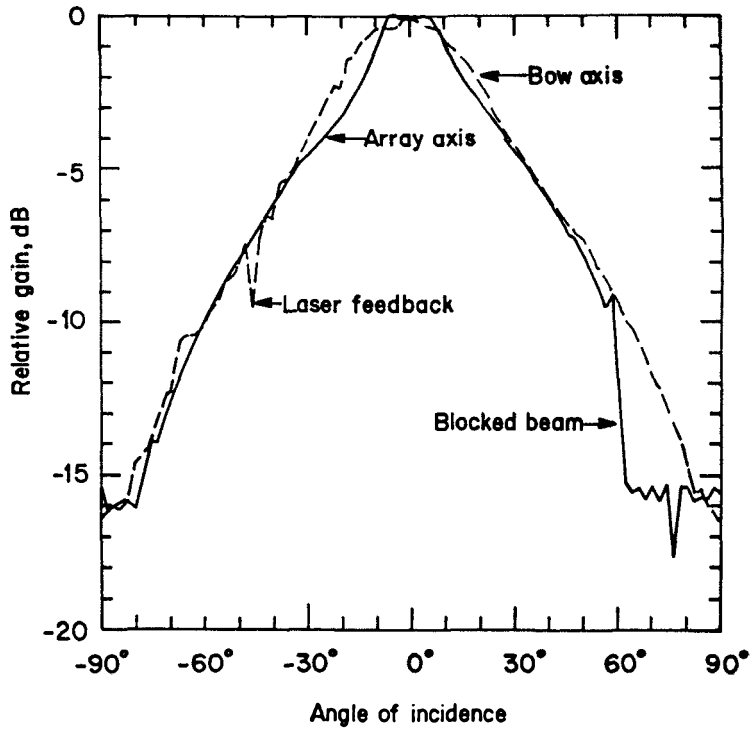


Figure 11. Measured array-axis and bow-axis patterns at 700 GHz.

References

- [1] D. B. Rutledge, D. P. Neikirk and D. P. Kasilingam, "Integrated circuit antennas," in *Infrared and Millimeter Waves*, vol. 10, K.J. Button, ed., Academic Press, New York, pp.1-90, 1983.
- [2] R. C. Compton, R. C. McPhedran, Z. Popović, G. M. Rebeiz, P. P. Tong and D. B. Rutledge, "Bow-tie antennas on a dielectric half-space: Theory and experiment," *IEEE Trans. Antennas Propagat*, vol. AP-35, pp. 622-631, June 1987.
- [3] G. W. Chantry, J. W. Fleming, P. M. Smith, "Far-infrared and millimeter-wave absorption spectra of some low-loss polymers," in *Chemical Physics Letters*, vol. 10, pp. 473-477, 1971.
- [4] K. Lee and M. Frerking, "Planar antennas on thick dielectric substrates," *12'th Int. Conf. Infrared Millimeter Waves*, pp. 216-217, Lake Buena Vista, Dec. 1987.
- [5] R. S. Elliott, "Antenna Theory and Design", pp. 336-341, Prentice-Hall, Englewood Cliffs, 1981.
- [6] K. E. Peterson, "Silicon as a mechanical material," *Proc. of the IEEE*, vol. 70, pp. 420-457, 1982.
- [7] R. H. DuHamel and D. E. Isbell, "Broadband logarithmically periodic antenna structure," *IRE National Convention Record*, Part I, pp. 119-128, 1957.
- [8] H. R. Feterman, P. E. Tannenwald et al., "Far-ir heterodyne radiometric measurements with quasioptical schottky diode mixers," *Appl. Phys. Lett*, vol. 33, pp.151-154, July 1978.
- [9] Anritsu Corporation, 15 Thornton Rd., Oakland NJ 07436.
- [10] C. A. Balanis, "Antenna Theory and Design," pp. 623-627, Harper and Row, New York, 1984.

Chapter 5

Future Work

Several two-dimensional imaging arrays have been demonstrated at millimeter-wave frequencies. The element pattern, cross-polarization, gain and the coupling efficiency to an imaging system have been measured. The measurements agree well with the analytical models derived in this thesis. The future work described in this section can be divided into two groups. The first discusses the limitation of the horn array and proposes methods to design a better imaging system. The second proposes new horn-array structures for imaging, communication and radiometric applications.

The superconductor-insulator-superconductor (SIS) detector [1] is well suited for integration with the horn array. It is a thin film detector, and could be deposited lithographically at the apex of a dipole antenna on the membrane. Thermal cycling of 1.6 mm square membranes from room temperature to 77° Kelvin showed no deterioration of the quality of the membranes. The supporting wafer could be Silicon or GaAs, depending on the electronics needed for the particular application. On the other hand, the GaAs Schottky-diode mixer [2] must be integrated on a supporting GaAs wafer near the membrane. The monopole antenna is better suited for this application. Phased-array applications and GaAs horn arrays are presented in Chap. 3.

5.1 Low-Frequency Horn Arrays

The fabrication difficulties in making large membranes have been solved by depositing silicon-oxynitride layers of very low residual stress. Currently, we can make membranes about 5×5 mm. This is enough to design monolithic two-dimensional horn arrays for 60 GHz applications. Such arrays would be suitable for space applications, where they are not affected by the large oxygen absorption line available

in our atmosphere [3]. However, the hydrostatic strength of the membrane falls off sharply with size. This could be solved by making much thicker membranes, about $4\text{--}5\mu\text{m}$, without affecting the radiation properties of the antenna. Such films can be easily deposited using plasma-enhanced chemical vapor deposition. Another approach is to support the membranes by several thin silicon or GaAs cantilevers. In the case of a silicon wafer, appropriate regions are heavily doped before the deposition of the silicon-oxynitride layer. The anisotropic etchant, ethylene-diamine pyrocatecol, does not attack highly doped p-type silicon [4]. The wafer is then etched in EDP, leaving a pyramidal cavity with a large membrane suspended by thin and narrow silicon cantilevers.

5.2 High-Gain Horn Arrays

A millimeter-wave imaging system requires a large number of focal-plane elements. An array size of (50×50) elements is not unreasonable at 300 GHz. The equivalent f-number of the imaging system should be around 2. This is necessary to reduce the aberrations and the gain loss of the outer elements of the array. However, the element pattern of a horn array does not improve considerably for openings greater than 1.5λ . This is due to the taper and phase errors across the aperture that result from the large flare angle (70.6°) of the horn.

A horn with a small effective flare angle does not suffer from these losses, and has high aperture efficiencies for large apertures. Such a horn could be fabricated by etching a number of silicon wafers in EDP, and then assembling them together with a mismatch at the boundary. The waveguide-step analytical approach developed by Dayalan Kasilingam [5] is well suited for the analysis of this structure. The corrugations on the sidewalls could be tailored to attenuate the high-order modes, resulting in E and H-plane patterns of equal beamwidths. Theoretical calculations on horns with small flare angles predict good coupling efficiencies to large f-number optical systems.

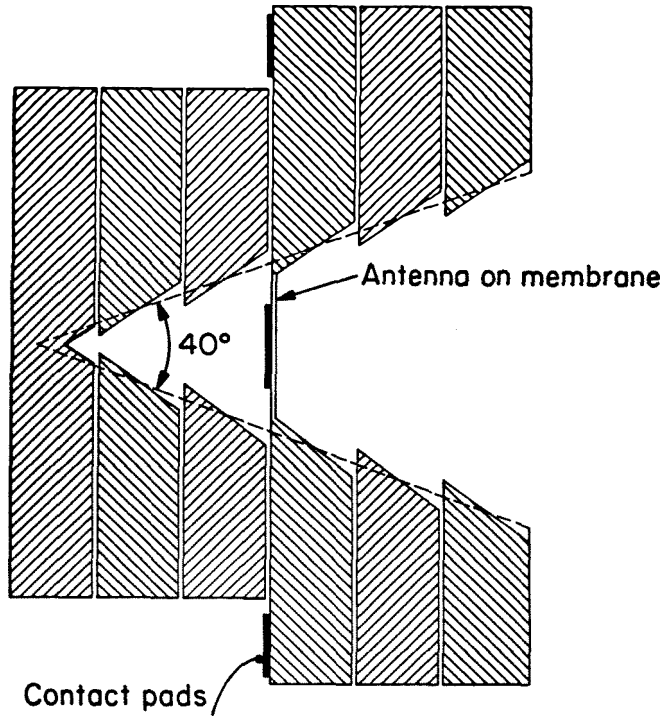


Figure 1. A high-gain small effective flare angle horn.

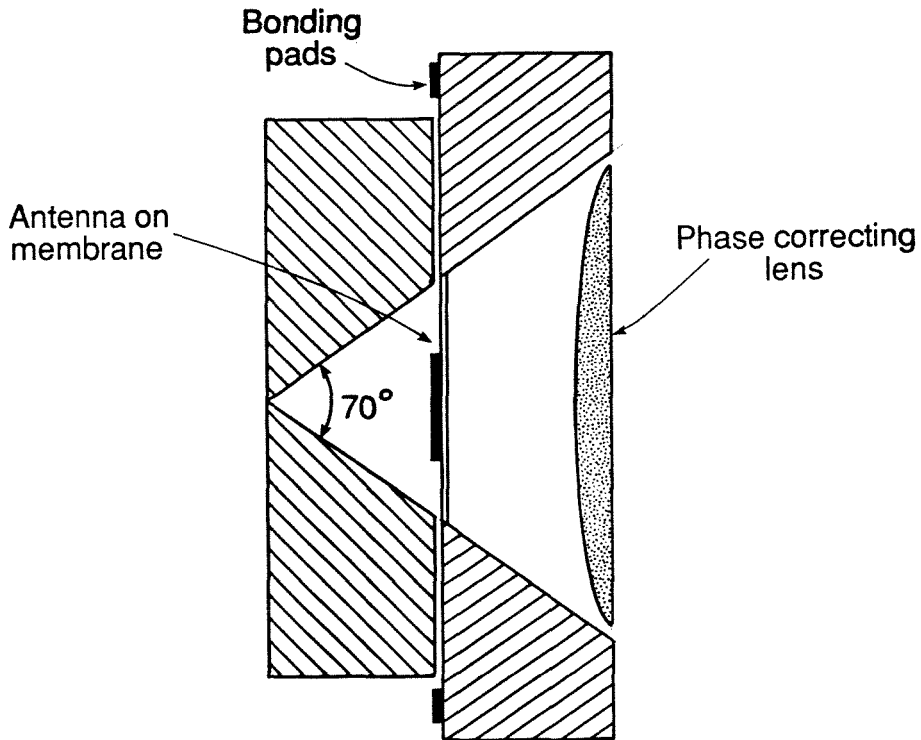


Figure 2. A lens-corrected horn with a large flare angle.

A high-gain horn could also be made using a large flare angle horn. The phase error at the aperture could also be corrected by inserting a dielectric lens in the pyramidal cavity (Fig. 2). The lens would provide the necessary phase shift such that the transmitted waves from the dipole arrive in phase at the horn aperture [6]. A 3.0λ horn at 94 GHz would require the fabrication of a 1-cm diameter lens. Such lenses are now easily machined in low-loss (Teflon or Polyethylene) dielectrics.

5.3 Doubly-Polarized Horn Arrays

In radiometric and remote-sensing applications, there is need for imaging arrays sensitive to two-orthogonal polarizations [7]. The dipole (or monopole) on the membrane yields a linearly polarized horn antenna. The cross-polarization level is about -18 dB in the 45° planes, with no measurable component in the E or H-planes. A doubly-polarized horn array could be fabricated by integrating two orthogonal monopoles on the same membrane. There are several disadvantages to this approach. The monopoles are very close to each other, and may couple strongly. Also, the symmetry of the dipole-horn structure is destroyed. Another approach is to suspend two membranes in the cavity, and integrate a horizontal and a vertical dipole on them (Fig. 3). As explained earlier in Chap. 2, there is region inside the cavity where the horn pattern is not sensitive to the dipole position. Both antennas will be integrated in this region. The co-polar and cross-polar patterns of the horn are given by the received power in the horizontal and vertical dipole, respectively. The dipole-horn symmetry is preserved, and therefore the horizontal dipole will not affect the E and H-plane patterns of the vertical dipole, and vice versa. However, there may be some coupling between the dipoles in the 45° planes. The resultant array has two monolithic wafers, processing two independent polarizations. This will ensure minimal coupling between the orthogonal polarizations.

5.4 Back-to-Back Horn Arrays

The local oscillator in a millimeter-wave heterodyne imaging system is gen-

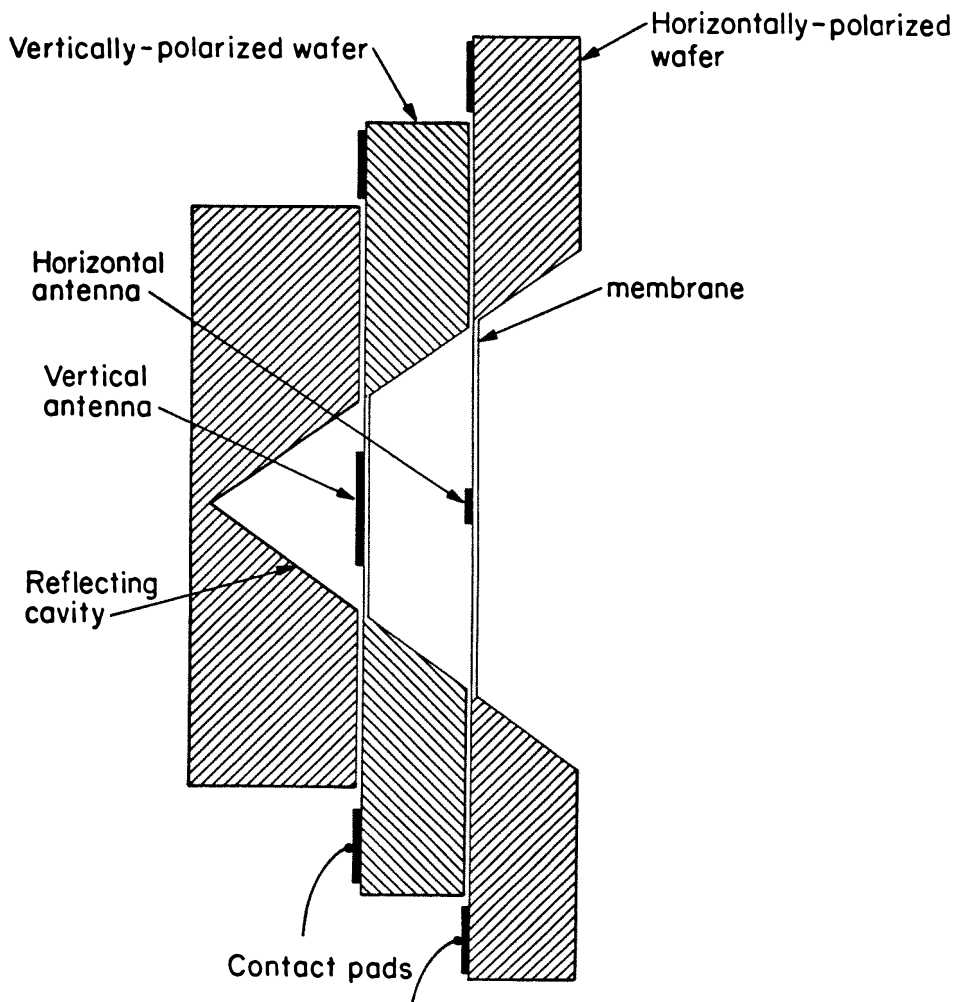


Figure 3. A doubly-polarized horn array.

erally introduced quasi-optically to the antenna and detector. This is done by placing a quasi-optical diplexer in front of the imaging system [8]. The diplexer combines the LO and the incident RF into a single beam with an efficiency near 100%. However, it has a very narrow acceptance angle, and is not useful in a multi-beam system. An alternative approach is to place a beam-splitter in front of the imaging array. The penalty paid is a loss in the incident RF energy, which lowers the overall efficiency of the imaging system. To solve this problem, we have introduced the back-to-back horn imaging array. In this structure, two horn arrays are integrated back-to-back using appropriately stacked silicon wafers. The antennas are integrated on the membranes. The back-to-back horns are electromagnetically isolated from each other. The front-horn receives the RF energy, while the back-horn receives the local oscillator. The RF and LO are fed to a balanced-mixer [9]. In a typical system, the membranes will not occupy more than half the available space on the wafer, leaving plenty of room for the balanced mixer. The resultant intermediate frequency is amplified and routed to the bonding pads. The back-to-back horn array is entirely monolithic with both RF and LO antennas and the balanced mixer integrated on the same wafer. This approach does not require a beam-splitter, and the system efficiency, from a quasi-optical point of view, is limited only by the coupling efficiency between the RF antenna and the imaging optics.

The major obstacle in this project is the development of a monolithic millimeter wave balanced mixer. The mixer structure must be able to receive energy from both the RF and LO antennas, and provide adequate isolation between them. This could be done by integrating a 3-dB hybrid at millimeter wavelengths [9]. The input ports are connected to the antennas while the output ports to the mixer diodes. The amount of coupling and isolation is strongly dependent on the impedances of the antennas, mixer diodes and transmission lines. Rigorous electromagnetic analysis of the mixer structure is therefore required to design an efficient balanced mixer.

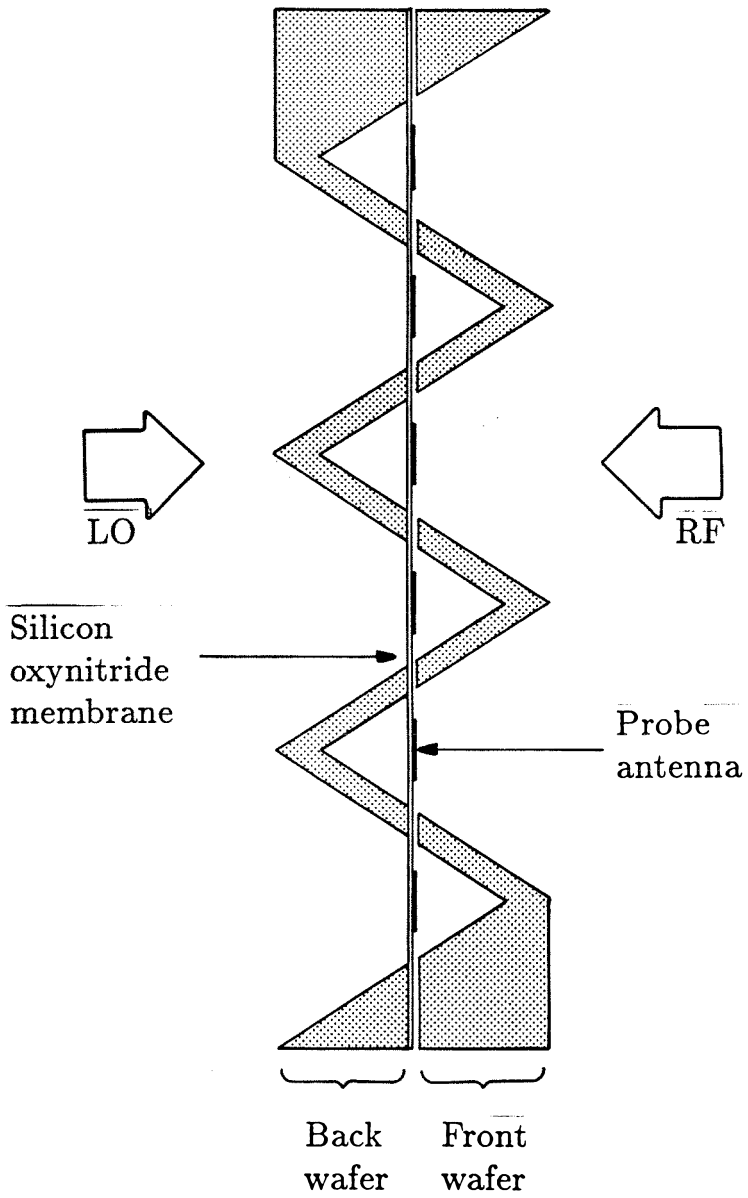


Figure 4. A back-to-back horn array.

5.5 Polarization-Duplexed Heterodyne Arrays

An efficient heterodyne imaging array could also be built by polarization-duplexing of the local oscillator and the RF signal [10]. The LO is introduced vertically polarized, while the RF horizontally polarized. Contrary to the case of a doubly-polarized imaging array, the LO signal would couple through the silicon wafer (Fig. 2—middle wafer) to a balanced mixer integrated near the RF antenna. Coupling networks through thick alumina substrates have been demonstrated at 10 GHz [11], and exhibit a coupling efficiency higher than 98%. For millimeter-wave applications, the silicon wafer should be a low-loss high resistivity wafer, and its thickness controlled by the coupling circuit.

5.6 Coaxial Doubly-Polarized Horn Arrays

Courtesy of Kent Potter [12] and Dr. Herb Pascalar [13]

In both configuration proposed above, one must translate the RF and LO signals from the antenna to a balanced mixer integrated on the substrate. An increase in the performance of the system is possible if the balanced mixer is put directly in the RF and LO signal paths. This is achieved by the novel coaxial doubly-polarized horn array. In this design, the front and back wafers flare into rectangular H-plane sectoral horns [14] rotated 90° from each other (Fig. 5). This results in a discontinuity in the horn structure at the membrane position. The horn dimensions are chosen such that only a TE_{01} and a TE_{10} waveguide mode can propagate in the front wafer and back wafers, respectively. The RF and LO signals are horizontally and vertically polarized, and are received by the front and back horns, respectively. Each horn provides an effective back-shortening cavity to the other horn, due to the polarization cut-off properties of the H-plane sectoral horns. A balanced mixer (Fig. 6) is integrated on the membrane [13]. The balanced mixer is placed directly in the path of the RF and LO signals, and therefore has better conversion characteristics. As discussed earlier, the membrane is well suited for SIS-mixer detectors.

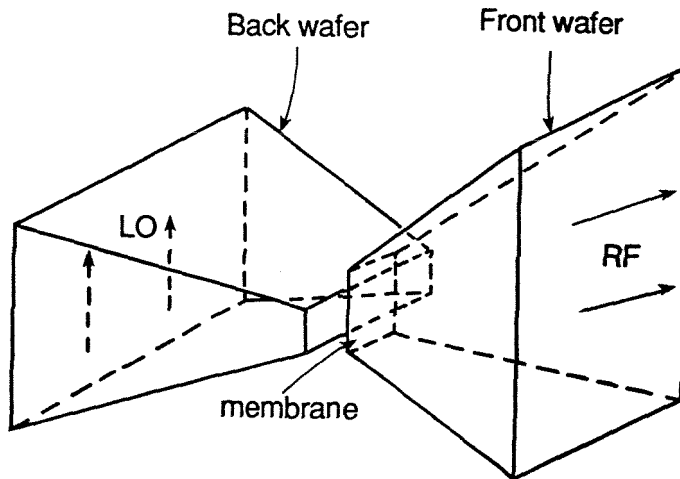


Figure 5. A coaxial doubly-polarized horn.

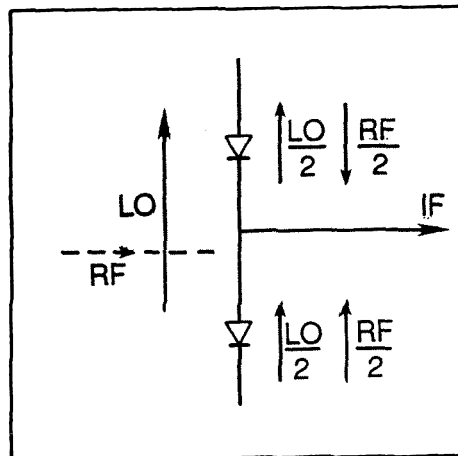


Figure 6. The layout of the balanced mixer on the membrane.

The coaxial-horn array leads intrinsically to a two-dimensional hexagonally spaced array. This is also an advantage because hexagonal arrays offer better imaging capabilities than their rectangular counterparts [15]. Also, the processing of a hexagonally sampled array offer substantial savings in computation time [16]. The front and back H-plane sectoral horns could also be tailored to produce E and H-plane patterns of equal beamwidths.

Finally, one could think of combining the ideas outlined above to design a high-gain back-to-back horn imaging array, or a coaxial doubly-polarized high-gain phased array. The phased array applications are most promising considering the recent advances in the fabrication of millimeter-wave devices and circuits. High-electron mobility transistors (HEMT) [17], and millimeter-wave monolithic phase-shifters and low-noise amplifiers are now available for frequencies around 60 GHz.

References

- [1] T. G. Phillips, D. P. Woody et. al., "Dayem-Martin (SIS tunnel junction) mixers for low noise heterodyne receivers," *IEEE Trans. Magnetics*, vol. MAG-17, pp. 684-689, Jan. 1981.
- [2] E. N. Grossman, "The performance of Scottky diodes as far-infrared modulators," *Int. J. Infrared Millimeter Waves*, vol. 9, Nov. 1987.
- [3] E. S. Rosenblum, "Atmospheric absorption of 10-400 KM CPS radiation: summary and bibliography to 1961," *Microwave J.*, vol. 4, pp. 91-96, March 1961.
- [4] K. E. Peterson, "Silicon as a mechanical material," *Proc. IEEE*, vol. 70, pp. 420-457, May 1982.
- [5] D. P. Kasilingam, "Topics in millimeter-wave imaging arrays," Ph. D Thesis, California Institute of Technology, June 1987.
- [6] P. J. B. Clarricoats and P. K. Saha, "Radiation pattern of a lens-corrected conical scalar horn," *Electron Letters*, vol. 5, pp. 300-301, Nov. 1969.
- [7] J. van Zyl, H. A. Zebker, and C. Elachi, "Imaging radar polarization signatures: Theory and observation," *Radio Science*, vol. 22, pp. 529-543, 1987.
- [8] N. R. Erickson, "A very low noise single-sideband receiver for 200-260 GHz", in *IEEE Trans. Microwave Theory Tech.*, vol. MTT-33, pp. 1179-1188, Nov. 1985.
- [9] S. A. Maas, "Microwave Mixers," Chapter 7, Artech House, Dedham, Massachusetts, 1986.
- [10] K. D. Stefan, N. Camilleri and T. Itoh, "A quasi-optical polarization-duplexed balanced mixer for millimeter-wave applications," in *IEEE Trans. Microwave Theory Tech.*, vol. MTT-31, pp. 164-170, Feb. 1983.

- [11] R. W. Jackson and D. W. Matolak, "Surface-to-surface transition via electromagnetic coupling of coplanar waveguides," *IEEE Trans. Microwave Theory Tech.*, vol. MTT-35, pp. 1027-1032, Nov. 1987.
- [12] Kent Potter, Engineer, Electrical Engineering Department, California Institute of Technology, Pasadena, CA 91125.
- [13] Dr. Herb Pascalar, Co-holder of a 1954 RCA patent on the balanced mixer, Aerojet Electrosystems, P.O.Box 296, Azusa, CA 91702.
- [14] R. C. Johnson, H. Jasik, "Antenna Engineering Handbook", Chap. 15, McGraw Hill, New York, 1984.
- [15] M. Born and E. Wolf, "Principles of Optics," Pergamon Press, Oxford, 1980.
- [16] R. M. Mersereau, "The processing of hexagonally sampled two-dimensional signals," *Proc. IEEE*, vol. 67, pp. 930-949, June 1979.
- [17] W. Yau, E. Watkins, S. Wang, K. Wang and B. Klatskin, "A four stage V-band MOCVD HEMT amplifier," *IEEE MTT Int. Microwave Conf.*, pp. 1015-1018, June 1987.